

H.W.M. Hoeijmakers<sup>1</sup>, M.P.J. Sanders<sup>1</sup>, L.H. Groot Koerkamp<sup>1</sup>, A. van Garrel<sup>1</sup> & C.H. Venner<sup>1</sup>

<sup>1</sup>University of Twente, Engineering Fluid Dynamics, PO Box 217, 7500 AE Enschede, the Netherlands

#### Abstract

Prandtl's Lifting-Line theory is applied to predict the aerodynamic characteristics of wings with various distributions of circulation. Expressions for induced upwash distribution, lift, drag, bending moment, adverse/proverse yawing moment and center-of-vorticity have been derived for numerically-computed or prescribed distributions of the circulation. The distributions include the classical elliptic distribution and a number of bell-shaped distributions. For a specified wing planform, solving Prandtl's integro-differential equation, analytically, or numerically, is more or less standard practice. Prandtl's methodology for minimization of induced drag for given lift and integrated section-bending-moment, requires finding the circulation distribution for a prescribed quadratic distribution of the upwash. For the minimization also involving the root-bending moment, the required distribution of the upwash contains a linear term. Determining the corresponding circulation distribution is less standard. However, for many upwash distributions the inverted Biot-Savart law between vortex distribution and upwash distribution yields a closed-form circulation distribution. In literature, the prescribed span-integrated section-bending-moment and the prescribed root-bending-moment are taken as the value of these moments for the wing with elliptic circulation distribution giving the prescribed lift. Here the generalization is considered to prescribe any value of span-integrated section-bending-moment and root-bending-moment. The results of the generalization reveal that an increase in each of the prescribed moments gives a reduction of the induced drag, facilitating a trade-off during wing design.

In the present study the upwash is determined along the span, as well as along the extension of the span from the tip outwards to infinity. This provides insight into the singular behavior of the upwash distribution in the tip region. This knowledge is used to assess the initial roll-up of the wake vortex sheet.

**Keywords:** flying wing, circulation distributions, wake roll-up, lifting-line theory

## 1. Introduction

The flying wing is an aircraft that does not have vertical nor horizontal tail surfaces: a wing-alone aircraft. Without the tail surfaces the (parasite) drag of the aircraft is smaller, while also the radar-cross-section (RCS) is smaller. Blended wing-body (BWB's) configurations might also be counted as belonging to the class of flying wings. However, without tail surfaces the controllability of flying-wing aircraft forms a challenge. Designs of flying-wing aircraft have been around for a long time, one might think of the hang-glider type of gliders that Lilienthal [1] experimented with, until his fatal flight accident in 1896. The 1920's saw a number of flying-wing gliders, notably those of the Horten brothers [2], [3]. During WW2 the Horten Brothers also developed military aircraft of flying-wing type, in Germany, such as the Horten Ho 229 V3 jet fighter-bomber, that was under construction at the end of WW2.



(a) Horten Ho 229 V3 Northrop-Grumman built replica [4]



(b) Northrop YB 49. National Museum US Air Force

Figure 1 a, b – Flying wing configurations of the 1940's.

After WW2 the prototype was shipped to the USA. Presently, this prototype is at the Steven F. Udvar-Hazy Center of the Smithsonian National Air and Space Museum at Washington's Dulles International Airport, USA, for preservation/restoration. Figure 1a shows a replica [4] of the Ho 229 V3, built by Northrop-Grumman for the National Geographic documentary "Hitler's Stealth Fighter" (2009), used for Radar-Cross-Section (RCS) measurements. The replica (no elevons, no engines) is on display at the San Diego Air and Space Museum.

Figure 1b shows the Northrop YB-49 prototype flying-wing jet bomber, in development between 1945 and 1950 [5]. It experienced severe control problems and the project was cancelled after some accidents. Figure 1c shows a 1990's example of a flying wing, the US Air Force B-2 Spirit stealth bomber [5]. The absence of tail surfaces contributes to reducing the RCS of such aircraft. Figure 1d shows a Prandtl-D flying-wing Radio-Controlled configuration (2010's) [6], designed to feature, like the Ho 229, a so-called bell-shaped spanwise distribution of the wing loading. The latter is proportional to the spanwise distribution of the section circulation. Such a circulation distribution generates an induced drag that is about 10% lower than the distribution that most aeronautical engineers consider to be the optimal distribution: the elliptic distribution. The bell-shaped distribution is the distribution that the Horten's implemented in their designs of gliders and other aircraft [2], [3].



Figure 1 c, d – Flying wings of the 1990's and 2010's.

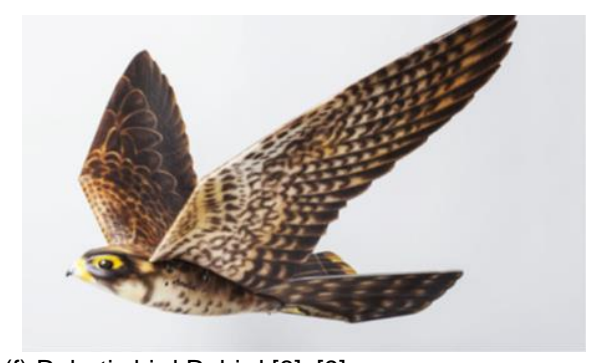


(d) Prandtl-D RC flying wing. [6], Figure 5.

There are numerous other wing planforms around, in aeronautical and maritime technology, as well as in nature and applied in robotic configurations to mimic their natural counterparts. The Gannet shown in Figure 1e, features a very slender thin wing with interesting wing tips. Figure 1f shows the Robird, an ornithopter type of drone mimicking the Peregrine Falcon.



(e) Northern Gannet [7].



(f) Robotic bird Robird [8], [9].

Figure 1 e, f – Example from nature (left) and example of robotic bird (right).

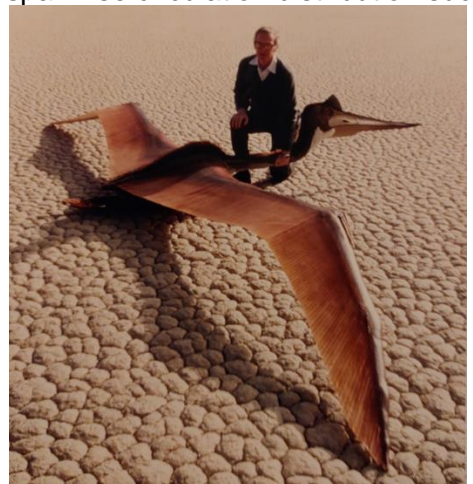
The Gannet ("Albatross of the Northern Atlantic", also known as Jan van Gent) [7], see Figure 1e, exemplifies an aerodynamically very efficient bird that can stay aloft for a long time and can cover large distances. Its wing planform is a prime example of a high-aspect-ratio wing featuring special wing tips. Presumably because of the geometry of these wing tips, this bird, like all birds, does not require a vertical control surface.

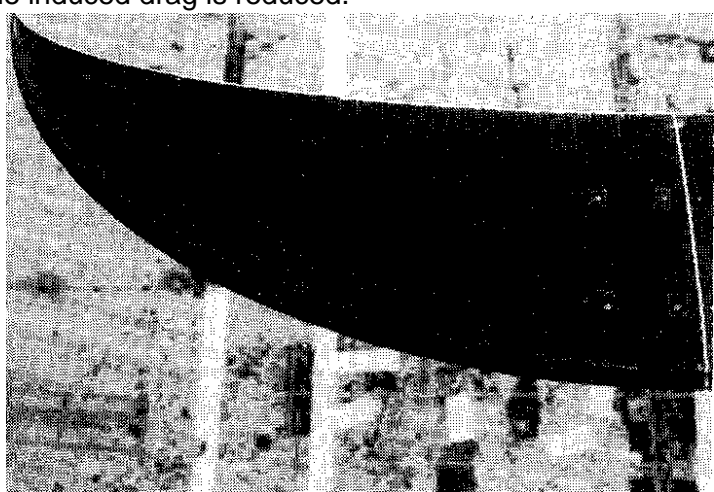
The Robird, see Figure 1f, is an ornithopter-type of drone developed by Clear Flight Solutions (CFS), that was designed to appear and fly like a Peregrine Falcon [8]. The wing of the Robird has an aspect ratio of about 7.5. The drone has the same dimensions and weight as the real falcon, and produces lift and thrust by flapping/pitching its wings [9]. Real birds instinctively sense that a falcon in flapping

flight is on the hunt, making the Robird very suitable for bird control at airports, garbage dumps, crop fields, etc.

Figure 1g shows the "On the Wing" movie (1986) replica Quetzalcoatus-Northropi of the extinct giant pterodactyl, which had a wing span of more than 10m. It was designed by Paul MacCready of Aero-Vironment [10]. MacCready's model of this pterosaur, is another drone shaped after a flying animal. The wing planform shows the same type of features as that of the Albatross.

Figure 1h is a photograph of a wind-tunnel model of a crescent-moon shaped wing design, investigated by van Dam et al. [11], [12]. Its elliptic distribution of the chord has been shifted in streamwise direction (flow is from bottom to top) in order to create an interaction between the vortex wake from the trailing edge and flow about the wing tip. Such an interaction is hypothesized to change the spanwise circulation distribution such that the induced drag is reduced.



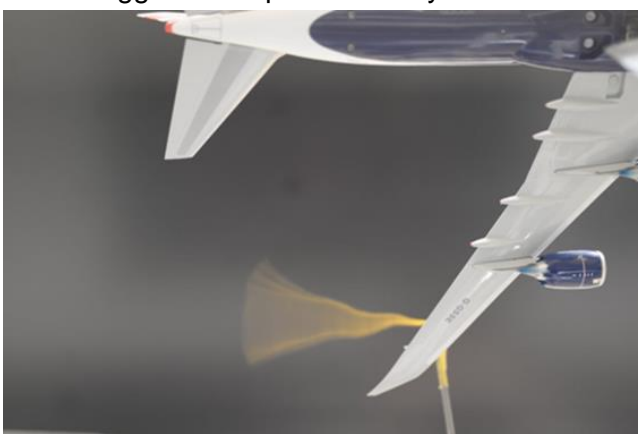


(g) Ornithopter of extinct giant pterodactyl [10]. (h) Crescent-moon shaped wing [11], [12]. Figure 1 g, h – Example from movie (left) and example of unconventional shape wing or fin.

At the University of Twente, a model B747-8, span about 0.35 m, see Figure 1i, has been used in demonstrations on aircraft aerodynamics in the (aero-acoustic) wind tunnel [13]. One of the goals of the demonstration is to show the tip vortices in the wake of aircraft. In these down-to-earth experiments for aspirant students and visitors of the facilities, it became clear that the tip vortex of the model B747-8, with its raked wing tip, i.e., integrated winglet, does not start at the wing tip, but at a location more inboard, see Figure 1j. This phenomenon triggered the present study.



(i) Top view of B747-8 model aircraft.



(j) Flow visualization with tuft, B747-8 model aircraft.

Figure 1 i, j – Example slender wing transport aircraft in UT wind-tunnel [13].

Figure 1i is a top view of the B747-8 model aircraft, showing the wing planform with unloaded raked wing tips. Figure 1j presents a top view of the same model in the (low-speed) wind tunnel of the University of Twente. The flow, visualized with a tuft, indicates the presence of a vortex that forms quite a bit inboard of the wing tip. The way in which a vortex wake rolls up is determined by the spanwise distribution of the section-circulation, or rather its derivative: the wake vortex distribution, as will be addressed in chapter 6.

In the present study the (Lanchester-)Prandtl lifting-line theory is used to investigate various circulation distributions that follow from minimising the induced drag, subject to different constraints. The lifting-line theory is a basic tool to investigate wing aerodynamics in concept design studies, to explore the effect on aerodynamic performance of different circulation distributions and their effect on the formation of wake vortices. Lifting-line theory allows an analytic approach to find insightful answers to research questions, even 100 years after its introduction by Prandtl's group in Göttingen, Germany.

The present paper is structured as follows:

Section 2 introduces the essentials of Prandtl's Lifting-Line Theory, including the not very well-known inverted Biot-Savart law which gives the vortex distribution for given upwash distribution. Three analysis/design approaches to using Prandtl's theory are discussed;

Section 3 describes the way the Lifting-Line methodology is used to obtain wing designs for minimum induced drag. Four scenarios are considered:

- (i) prescribed lift and span;
- (ii) prescribed lift and span-integrated section-bending-moment;
- (iii) prescribed lift and root-bending moment, and;
- (iv) prescribed lift, span-integrated section-shear-force (equivalent to root-bending moment) and span-integrated section-bending-moment.

Detailed expressions are derived for circulation distributions and vortex distributions, as well as distributions of upwash along the lifting line and its extension in outward direction. Furthermore, for assessment of aerodynamic performance, expressions are derived for overall lift, drag, bending moments and yawing moment, as well as location of the center of the vortex distribution;

Section 4 presents verification of the methodology via the application of the developed expressions to the Prandtl-D(rag) wing pursued by Bowers et al. [6], based on a bell-shaped circulation distribution. Present results are compared with results found in [6].

Section 5 presents the results of the application of the present lifting-line methodology to the wing planform of the Robird robotic bird;

Section 6 presents upwash distributions on lifting line and its outward extensions, as well as some results for the initial roll-up of the vortex wake of wings with bell-shaped distributions of the circulation. Section 7 provides the conclusions of the present investigation.

# 2. Prandtl's Lifting-Line Theory

In the first half of the twentieth century, Prandtl's group in Göttingen derived the lifting-line theory [14], [15] for determining the aerodynamic characteristics of slender (high aspect-ratio), thin, mildly-cambered, nonelastic, non-swept, 3D wings positioned in a uniform free stream of velocity  $U_{\infty}$ , in steady, incompressible, inviscid, irrotational (potential) flow. In this theory the wing is represented by a line-vortex along its quarter-chord line, of strength equal to the circulation  $\Gamma(y)$  of the airfoil sections making up the wing. In order to obey Kelvin-Helmholtz's vortex laws, a planar vortex sheet is added, which trails from the lifting-line to infinity downstream, see Figure 2.

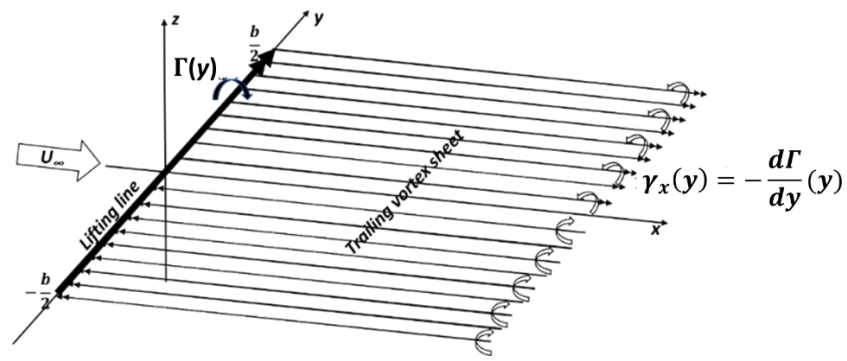


Figure 2 – Mathematical model Prandtl's lifting-line method for incompressible potential flow about high-aspect-ratio wing at small angle-of-attack.

# 2.1 Formulation lifting-line theory

Prandtl's integro-differential equation solves for the distribution of the circulation  $\Gamma(y)$  along the span of the lifting line. The lifting line is situated along the y-axis for |y| < b/2 in the plane z = 0. The wake

vortex sheet (x > 0), also in the plane z = 0, is attached to the lifting line and extends to infinity  $(x \to 0)$ ∞). In the present paper it is assumed that the problem features starboard-side/port-side symmetry. Prandtl's equation is obtained by equating the expression for the section lift  $\ell(y)$  in terms of the section circulation  $\Gamma(y)$ , obtained through Kutta-Joukowsky's Theorem, and the expression of the section lift  $\ell(y)$  in terms of the lift coefficient  $c_{\ell}(y)$  and the section chord c(y):

$$\ell(y) = \rho_{\infty} U_{\infty} \Gamma(y)$$
 and  $\ell(y) = \frac{1}{2} \rho_{\infty} U_{\infty}^2 c(y) c_{\ell}(y)$ , respectively, (1a)

$$\ell(y) = \rho_{\infty} U_{\infty} \Gamma(y) \text{ and } \ell(y) = \frac{1}{2} \rho_{\infty} U_{\infty}^2 c(y) c_{\ell}(y), \text{ respectively,}$$
with, the slope  $a_0$  of the section-lift curve assumed constant:
$$c_{\ell}(y) = a_0 \alpha_{eff}(y) = a_0 \left( \Delta \alpha(y) + \frac{w_{in}(y)}{U_{\infty}} \right) = a_0 \left( \alpha - \alpha_0(y) + \beta(y) + \frac{w_{in}(y)}{U_{\infty}} \right). \tag{1b}$$

This exercise yields Prandtl's integro-differential equation for 
$$\Gamma(y)$$
:
$$\Gamma(y) = \frac{1}{2} U_{\infty} c(y) a_0 \left[\alpha - \alpha_0(y) + \beta(y) + \frac{w_{in}(y)}{U_{\infty}}\right], \text{ for } |y| < b/2 \text{ and } \Gamma(|y| = b/2) = 0. \tag{1c}$$
The arrange of  $C$  is the solution of at the lifting line bands are the statement as a solution line.

The upwash  $w_{in}(y)$ , induced at the lifting line by the wake vortex sheet downstream of the lifting line, expressed as Cauchy-Principle-Value integral, equals (Biot-Savart's law):

$$w_{in}(|y| < b/2) = \frac{1}{4\pi} \text{CPV} \int_{-b/2}^{b/2} \gamma_x(y') \frac{dy'}{y - y'}, \tag{1d}$$

with the *x*-component of the vortex distribution on the wake vortex sheet  $\gamma_x(y') = -\frac{d\Gamma}{dy'}(y')$ .

The relation given in Eq. (1d) between the distribution of the upwash  $w_{in}(y)$  and that of the strength  $\gamma_r(y)$  of the wake vortex sheet can be inverted into

$$\gamma_x(y) = -\frac{4}{\pi} \frac{1}{\sqrt{(b/2)^2 - y^2}} \text{CPV} \int_{-b/2}^{b/2} w_{in}(y') \frac{((b/2)^2 - y'^2)^{1/2}}{y - y'} dy', \text{ for } |y| < b/2,$$
(2a)

which might be called the inverted Biot-Savart law. Following the evaluation of Eq. (2a), the distribution of the circulation  $\Gamma(y)$  is found by substituting Eq. (2a) in

$$\Gamma(y) = \int_{y}^{b/2} \gamma_{x}(\tilde{y}) d\tilde{y}, \text{ for } |y| < b/2.$$
(2b)

In literature the inverted relation Eq. (2a), between  $w_{in}(y)$  and  $\gamma_x(y)$ , does not appear to be widely known. Jones [17], Eqs. (11, 12), based on Munk [18], provides a very brief account on the derivation of a relation similar to Eq. (2a) above. Klein and Viswanathan [19], also present a similar relation, derived from airfoil theory. Nickel [20], [21] presents the inverted relation in the form of Eq. (2b) with Eq. (2a) substituted. Nickel derived this expression considering Eq. (1d) as a Fredholm integral equation of the first kind for  $\gamma_x(y) = -(d/dy)\Gamma(y)$  with  $w_{in}(|y| < 1)$  specified. Nickel's result would read, in the present notation:

$$\Gamma(y) = \frac{4}{\pi} \int_{-b/2}^{b/2} w_{in}(y') \ln \frac{((b/2)^2 - y^2)^{1/2} ((b/2)^2 - y'^2)^{1/2} + (b/2)^2 - y'y}{(b/2)|y-y'|} dy'. \tag{2c}$$
To verify Eq. (2c), differentiate Eq. (2c) with respect to  $y$ , which yields
$$\frac{d}{dy} \Gamma(y) = -\frac{4}{\pi} \frac{1}{\sqrt{(b/2)^2 - y^2}} \text{CPV} \int_{-b/2}^{b/2} w_{in}(y') \frac{((b/2)^2 - y'^2)^{1/2}}{y-y'} dy'$$
Since  $\gamma_x(y) = -(d/dy)\Gamma(y)$ , indeed this expression is equal to the expression for the vortex distribution

$$\frac{d}{dy}\Gamma(y) = -\frac{4}{\pi} \frac{1}{\sqrt{(b/2)^2 - y^2}} CPV \int_{-b/2}^{b/2} w_{in}(y') \frac{((b/2)^2 - y'^2)^{1/2}}{y - y'} dy'$$

 $\gamma_x(y)$  in Eq. (2a). Nickel [20], [21] presents the circulation distribution for a number of port-side/starboard-side symmetric and nonsymmetric distributions of the upwash.

In the present study, the inversion of Eq. (1d), given in Eq. (2a), has been inspired by the treatise of Ashley & Landahl ([22], section 5.3) on the inversion of the formulation of thin-airfoil theory in the complex plane.

Finally, for the velocity induced at points on the outward extensions of the span Eq. (1d) is a regular integral, not requiring the CPV-evaluation:

$$w_{in}(|y| > b/2) = \frac{1}{4\pi} \int_{-b/2}^{b/2} \gamma_x(y') \frac{dy'}{y-y'}$$
 (2d)

## 2.2 Analysis and design/optimization formulations

For specified free-stream density  $\rho_{\infty}$  and free-stream velocity  $U_{\infty}$  parallel to the x-axis, Prandtl's liftingline (integro-differential) equation, given in Eq. (1c-d), can be utilised in three ways:

1. Aerodynamic performance analysis: Given the planform of the wing, i.e., span b and distribution section-chord c(y), as well as  $\Delta \alpha(y) = \alpha - \alpha_0(y) + \beta(y)$ , with  $\alpha$  the wing angle of attack,  $\alpha_0(y)$  the section-zero-lift angle-of-attack and  $\beta(y)$  the section-twist-angle, the integro-differential equation Eq. (1c) can be solved approximately for  $\Gamma(y)$  by expanding the spanwise circulation distribution  $\Gamma(y)$  as a Fourier series and solving analytically for the coefficients in the series. This is the approach followed by Prandtl's group. Alternatively, as in the present research, the integro-differential

equation can be discretised employing local polynomial-type of expansions of the circulation distribution  $\Gamma(y)$  and determining the parameters in the local expansions by solving the resulting system of linear algebraic equations, e.g., [23].

Once the circulation distribution  $\Gamma(y)$  has been computed, the wing's aerodynamic performance is obtained in terms of the components of the overall forces and moments: lift L, induced drag D, starboard-side span-integrated section-shear-force  $F_z$ , starboard-side root-bending moment  $M_x$ , span-integrated section-bending-moment  $M_{x,2}$  and starboard-side yawing moment  $M_z$ . Furthermore, also computed are the section lift  $\ell(y)$ , drag d(y), section shear force  $f_z(y)$ , the section-starboard-root-bending-moment  $m_x(y)$ , section-span-integrated-bending-moment  $m_{x,2}(y)$  and yawing-moment  $m_z(y)$ , see Appendix A and Table 1.

Section forces and moments	Integrated along span	Conversion from y to $\eta = y/(\frac{b}{2})$
$\ell(y) = \rho_{\infty} U_{\infty} \Gamma(y)$	$L = \rho_{\infty} U_{\infty} \int_{-b/2}^{b/2} \Gamma(y) dy$	$=q_{\infty}b^2\int_{-1}^{1}\frac{\Gamma(\eta)}{U_{\infty}b}d\eta$
$d(y) = -\rho_{\infty} w_{in}(y) \Gamma(y)$	$D = -\rho_{\infty} \int_{-b/2}^{b/2} \Gamma(y) w_{in}(y) dy$	$=-q_{\infty}b^2\int_{-1}^{1}rac{\Gamma(\eta)}{U_{\infty}b}rac{w_{in}(\eta)}{U_{\infty}}d\eta$
$f_z(y) = \int_y^{b/2} \ell(y') dy'$	$F_z = \rho_\infty U_\infty \int_0^{b/2} \Gamma(y) y dy$	$=q_{\infty}b^3rac{1}{2}\int_0^1rac{\Gamma(\eta)}{U_{\infty}b}\eta d\eta$
$m_{\chi}(y) = y\ell(y)$	$M_x = \rho_\infty U_\infty \int_0^{b/2} \Gamma(y) y dy$	$=q_{\infty}b^3rac{1}{2}\int_0^1rac{\Gamma(\eta)}{U_{\infty}b}\eta d\eta$
$m_{x,2}(y) = \int_y^{b/2} \ell(y')(y'-y)dy'$	$M_{x,2} = \frac{1}{2} \rho_{\infty} U_{\infty} \int_0^{b/2} \Gamma(y) y^2 dy$	$=q_{\infty}b^4rac{1}{8}\int_0^1rac{\Gamma(\eta)}{U_{\infty}b}\eta^2d\eta$
$m_z(y) = -d(y)y$	$M_z = \rho_\infty \int_0^{b/2} \Gamma(y) w_{in}(y) y dy$	$=q_{\infty}b^{3}\frac{1}{2}\int_{0}^{1}\frac{\Gamma(\eta)}{U_{\infty}b}\frac{w_{in}(\eta)}{U_{\infty}}\eta d\eta$

Table 1 Formula aerodynamic performance quantities.  $q_{\infty} = \frac{1}{2} \rho_{\infty} U_{\infty}^2$  is free-stream dynamic pressure.

Note that in the derivation of the expression for  $F_z$  and that for  $M_{x,2}$  in Table 1, use has been made of partial integration and of Leibniz's rule of differentiating integrals. For example, for the span-integrated section-bending-moment  $M_{x,2}$ :

$$\begin{split} \int_0^{b/2} m_{x,2}(y) dy &= \left[ y m_{x,2}(y) \right] \Big|_0^{b/2} - \int_0^{b/2} y \frac{d}{dy} m_{x,2}(y) dy = - \int_0^{b/2} y \left\{ - \int_y^{b/2} \ell(y') dy' \right\} dy \\ &= \int_0^{b/2} y \left[ \int_y^{b/2} \ell(y') dy' \right] dy = \left[ \frac{1}{2} y^2 \int_y^{b/2} \ell(y') dy' \right] \Big|_{y=0}^{b/2} + \int_0^{b/2} \frac{1}{2} y^2 \ell(y) dy. \\ &= \int_0^{b/2} \frac{1}{2} y^2 \ell(y) dy = \frac{1}{2} \rho_\infty U_\infty \int_0^{b/2} y^2 \Gamma(y) dy \end{split}$$

An additional quantity considered is  $y_{COV}$ , the location of the center of the x-component of the wake vortex distribution  $\gamma_x(y)$ . The center-of-vorticity (COV) of the starboard side of the x- (and only) component of the wake vortex distribution  $\gamma_x(y)$ , follows from:

$$y_{COV} \equiv \int_0^{b/2} \gamma_x(y) y dy / \int_0^{b/2} \gamma_x(y) dy = \frac{1}{\Gamma(0)} \int_0^{b/2} \Gamma(y) dy$$
 (3)

In the present study the focus is on the design/optimisation problem of prescribing specific distributions of the circulation  $\Gamma(y)$  that follow from minimising the induced drag. This leads to the next two problem formulations, for given  $\Gamma(y)$ :

2. For prescribed distribution of the circulation  $\Gamma(y)$ , the upwash distribution  $w_{in}(y)$  is computed from Eq. (1d). Then, if for given  $a_0$  and  $U_{\infty}$ ,  $\Delta\alpha(y) = \alpha - \alpha_0(y) + \beta(y)$  is specified, the spanwise distribution of the chord c(y) required to generate the prescribed circulation distribution, follows from Eq. (1c) as:

$$c(y) = \frac{2\Gamma(y)}{a_0 U_{\infty} \left(\alpha - \alpha_0(y) + \beta(y) + \frac{w_{in}(y)}{U_{\infty}}\right)}, \text{ for } |y| \le b/2.$$

$$(4a)$$

3. If for given  $a_0$  and  $U_\infty$ , c(y) and  $\alpha - \alpha_0(y)$  are specified, the geometric twist distribution  $\beta(y)$  required for generating the prescribed spanwise distribution of the circulation  $\Gamma(y)$ , follows from Eq. (1c) as:

$$\Delta \alpha(y) = \alpha - \alpha_0(y) + \beta(y) = \frac{2\Gamma(y)}{a_0 U_\infty c(y)} - \frac{w_{in}(y)}{U_\infty}, \text{ for } |y| \le b/2.$$
(4b)

# 3 Minimization Induced Drag

The task considered is to determine the distribution of the circulation  $\Gamma(y)$  that minimises the induced drag D. For this purpose, upon introducing an arbitrary infinitesimal variation  $\delta\Gamma(y)$  of the circulation  $\Gamma(y)$ , accounting for the resulting variation of the upwash, Prandtl (and Betz) [14] set the ensuing

variation  $\delta D$  of the induced drag D equal to zero. Using the expression for the induced drag listed in Table 1 and the analysis in Appendix B, gives for  $\delta D$ :

$$\delta D = -2\rho_{\infty} \int_{-b/2}^{b/2} w_{in}(y) \delta\Gamma(y) dy = 0, \tag{5}$$

for positive  $\Gamma(v)$ .

In this section, four scenarios have been investigated for minimising the induced drag D:

- (a) Section 3.1: prescribed lift L, for given span b;
- (b) Section 3.2: prescribed lift L, prescribed starboard-span-integrated section-bending-moment  $M_{\chi,2}$ , which is some measure for the structural weight of the wing. The span b of the wing is a free parameter, it will be determined as part of the outcome;
- (c) Section 3.3: prescribed lift L, prescribed starboard root-bending-moment  $M_x$ , which is another measure for the wing structural weight. The span b of the wing is free, it will be part of the outcome.
- (d) Section 3.4: prescribed lift L, prescribed starboard root-bending-moment  $M_x$  (equal to span-integrated section-shear-force  $F_z$ ) in combination with the starboard-span-integrated section-bendingmoment  $M_{x,2}$ . The combination of  $M_x$  and  $M_{x,2}$  represents a more comprehensive measure for the wing structural weight. The span b of the wing is free, it will be determined as part of the outcome. Note that: scenario (a) was considered by Prandtl [14]; scenario (b) by Prandtl [15]; scenario (c) by Jones [17] and Nickel [21] and; scenario (d) by Klein and Viswanathan [24].

Further note that there are many more practical relevant scenarios, such as:

- scenario (b) with span-integrated section-bending-moment divided by section thickness, e.g., Löbert [25] and McGeer [26];
- either scenario coupled to the Breguet range formula for mission-performance analysis Iglesias & Mason [27] and Bragado-Aldana & Riaz [28].

## 3.1 Minimization Induced Drag for prescribed Lift and prescribed Wing Span

The classic scenario of minimizing the induced drag is to prescribe lift  $L = L_{\rho}$  in combination with the span  $b_e$  of the wing. Therefore, the variation  $\delta L$  due to an infinitesimal variation  $\delta \Gamma(y)$  of the circulation  $\Gamma(y)$  should be zero, i.e., using the expression for the lift in terms of the circulation distribution  $\Gamma(y)$ , given in Table 1, Appendix B lists the optimalisation problem: as

$$\delta D = -2\rho_{\infty} \int_{-b/2}^{b_e/2} w_{in}(y) \delta \Gamma(y) dy = 0 \text{ subject to}$$
 (5)

$$\delta D = -2\rho_{\infty} \int_{-b_e/2}^{b_e/2} w_{in}(y) \delta \Gamma(y) dy = 0 \text{ subject to}$$

$$\delta L = \rho_{\infty} U_{\infty} \int_{-b_e/2}^{b_e/2} \delta \Gamma(y) dy = 0.$$
(5)

So, it is found from Eq. (5), that, in order to minimise induced drag D, for constant span  $b_e$ ,  $w_{in}(y)$ should be constant, here chosen as:  $w_{in}(y) = -U_{\infty}A_0$ , with  $A_0$  an arbitrary constant.

For specified  $w_{in}(y)$  the vortex distribution  $\gamma_x(y)$  follows from the inverted Biot-Savart relation, Eq.

$$\gamma_{x}(y) = \frac{4}{\pi} \frac{U_{\infty} A_{0}}{\sqrt{(b_{e}/2)^{2} - y^{2}}} CPV \int_{-b_{e}/2}^{b_{e}/2} \frac{((b_{e}/2)^{2} - y'^{2})^{1/2}}{y - y'} dy' = \frac{4}{\pi} \frac{U_{\infty} A_{0}}{\sqrt{1 - \eta^{2}}} CPV \int_{-1}^{1} \frac{(1 - {\eta'}^{2})^{1/2}}{\eta - \eta'} d\eta' = \frac{4U_{\infty} A_{0} \eta}{\sqrt{1 - \eta^{2}}}, \tag{7a}$$

with  $\eta = y/(b_e/2)$ . It then follows from Eq. (2b) that the distribution of the circulation is indeed the elliptic distribution, found in any textbook on aircraft aerodynamics, e.g., [29]:

$$\Gamma(y) = 4U_{\infty}A_0\sqrt{(b_e/2)^2 - y^2} \equiv \Gamma_{0,e}\sqrt{1 - \eta^2}, \text{ with } \Gamma_{0,e} = 4U_{\infty}A_0\frac{b_e}{2}.$$
 (7b)

Therefore, 
$$\gamma_{\chi}(\eta) = U_{\infty} \frac{\Gamma_{0,e}}{U_{\infty}b_{e}} \frac{2\eta}{\sqrt{1-\eta^{2}}}$$
 and  $w_{in}(\eta) = -\frac{1}{2}U_{\infty} \frac{\Gamma_{0,e}}{U_{\infty}b_{e}}$ . (7c)

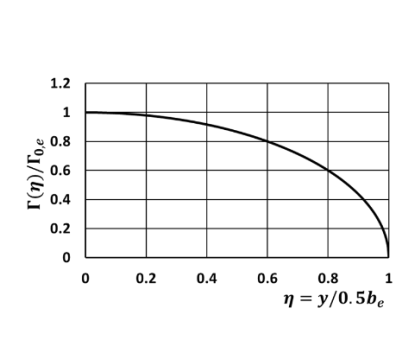
The aerodynamic performance, calculated using the formulas in Table 1, is presented in Table 2 below. The table includes the expressions for the induced upwash  $w_{in}(\eta)/U_{\infty}$ , both at the lifting line  $(|\eta| < 1)$  and at its outboard-directed extensions  $(|\eta| > 1)$ . The upwash at the latter points is obtained by evaluating Eq. (1d) for  $|\eta| > 1$ , as a regular integral, see Appendix C for the integrals. The table also includes the location of the center-of-gravity  $y_{cov.e}/(0.5b_e)$  of the vortex distribution  $\gamma_x(\eta)$ .

In Table 2 the forces and moments are expressed in dimensionless form, using  $q_{\infty}$  and powers of the (full) span  $b_e$ . These dimensionless quantities are a function of dimensionless amplitude  $\Gamma_{0,e}/U_{\infty}b_e$  of the circulation distribution, or equivalently, of dimensionless lift  $L_e/q_\infty b_e^2$ , only. The results indeed show that the induced drag  $D_e$  is quadratic in the prescribed lift  $L_e$  and that the induced drag  $D_e$  decreases quadratically with span  $b_e$ : the classic result for the elliptic circulation distribution. The two bending moments are linear in the prescribed lift  $L_e$ , while the yawing moment is quadratic in the lift  $L_e$ .

$\Gamma(\eta) = \Gamma_{0,e} \sqrt{1 - \eta^2}$	Function of $\frac{\Gamma_{0,e}}{U_{\infty}b_e}$	Function of $\frac{L_e}{q_{\infty} b_e^2}$
$\frac{w_{in}( \eta <1)}{U_{\infty}}$	$-\frac{1}{2}\frac{\Gamma_{0,e}}{U_{\infty}b_{e}}$	$-rac{1}{\pi}rac{L_e}{q_{\infty}b_e^2}$
$\frac{w_{in}( \eta >1)}{U_{\infty}}$	$\frac{-\frac{1}{2}\frac{1}{U_{\infty}b_{e}}}{-\frac{1}{2}\frac{\Gamma_{0,e}}{U_{\infty}b_{e}}(1-\frac{ \eta }{\sqrt{\eta^{2}-1}})}$	$-\frac{1}{\pi} \frac{L}{q_{\infty} b_e^2} \left(1 - \frac{ \eta }{\sqrt{\eta^2 - 1}}\right)$
$\frac{L_e}{q_{\infty}b_e^2}$ $\frac{D_e}{q_{\infty}b_e^2}$	$\frac{\pi}{2} \frac{\Gamma_{0,e}}{U_{\infty}b_{e}}$	
$\frac{D_e}{q_{\infty}b_e^2}$	$\frac{\frac{\pi}{4} \left(\frac{\Gamma_{0,e}}{U_{\infty} b_e}\right)^2}{\frac{1}{\Gamma_{0,e}}}$	$\frac{1}{\pi} \left( \frac{L_e}{q_{\infty} b_e^2} \right)^2$
$\frac{M_{x,e}}{q_{\infty}b_e^3}$	$6 U_{\infty} b_e$	$\frac{1}{3\pi} \frac{L_e}{q_{\infty} b_e^2}$
$\frac{M_{X,2,e}}{q_{\infty}b_{e}^{4}}$	$\frac{\pi}{128} \frac{\Gamma_{0,e}}{U_{\infty} b_e}$	$\frac{1}{64} \frac{L_e}{q_{\infty} b_e^2}$
$\frac{M_{z,e}}{q_{\infty}b_e^3}$	$-rac{1}{12} \Big(rac{\Gamma_{0,e}}{U_{\infty}b_e}\Big)^2$	$-rac{1}{3\pi^2}{\left(rac{L_{m{ec{e}}}}{q_{\infty}b_{m{ec{e}}}^2} ight)}^2$
$y_{cov,e}/0.5b_e$	$\frac{\pi}{4}$	

Table 2 - Aerodynamic performance for scenario (a) minimisation of induced drag  $D_e$ , for prescribed free-stream conditions  $(U_{\infty}, q_{\infty})$ , lift  $L_e$  as  $L_e/q_{\infty}b_e^2$  and span  $b_e$ : yielding elliptic distribution circulation  $\Gamma(\eta) = \Gamma_{0,e}\sqrt{1-\eta^2}$ , with  $\eta = [y/0.5b_e]/\sigma; \sigma = b/b_e = 1.$ 

As shown in Figure 3, at the wing tip  $\eta = 1$ , the circulation distribution has zero function value and infinite first and higher derivatives. At the wing tip the vortex distribution  $\gamma_x(\eta)$  features a square-root singularity and is therefore infinite. The induced upwash  $w_{in}(\eta)$ , the requirement that followed from the optimisation formulation, Eqs. (5) and (6), is a negative constant all along the lifting line. Along the outward extension of the lifting line, the upwash is positive featuring a discontinuity at  $\eta = 1$ , the wing tip, where the upwash has a square-root singularity for  $\eta \downarrow 1$ .



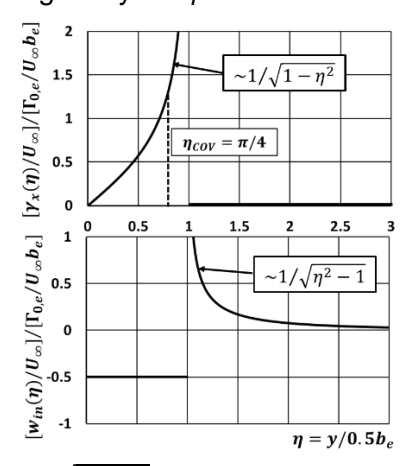


Figure 3 – Left: Elliptic distribution circulation  $\Gamma(\eta) = \Gamma_{0,e} \sqrt{1 - \eta^2}$ ; Right-upper: Vortex distribution  $\gamma_{\chi}(\eta)$ ; Rightlower: Distribution upwash  $w_{in}(\eta)$  on starboard-side lifting line and its outward extension. Dashed line: location COV.  $\eta = [y/0.5b_e]/\sigma$ ;  $\sigma = b/b_e = 1$ .

In case the spanwise distribution of the section chord c(y) of the wing is given, Eq. (4b), derived from Prandtl's integro-differential equation, provides the section angle-of-attack combination  $\Delta \alpha(y) = \alpha$  $\alpha_0(y) + \beta(y)$ , consisting of wing angle-of-attack  $\alpha$ , section zero-lift angle-of-attack  $\alpha_0(y)$  and section geometric twist-angle  $\beta(y)$  of the wing. Alternatively, in case  $\Delta\alpha(y)$  is given, Eq. (4a), also derived from Prandtl's integro-differential equation, provides the spanwise distribution of section chord c(y).

# 3.2 Minimization Induced Drag for prescribed Lift and Span-integrated Section-Bending-Moment

For scenario (b), the optimisation is for constant lift L, and for constant starboard-side-integrated section-bending-moment  $M_{x,2}$ , with circulation distribution  $\Gamma(\eta)$  and the span b of the wing to be determined. Now not only the variation  $\delta L$  of the lift L, but also the variation  $\delta M_{x,2}$  of  $M_{x,2}$ , due to an infinitesimal variation  $\delta\Gamma(y)$ , should be zero, i.e., the formulation of the optimalisation problem reads, see Appendix B:

$$\delta D = -2\rho_{\infty} \int_{-b/2}^{b/2} w_{in}(y) \delta \Gamma(y) dy = 0, \text{ subject to}$$
 (5)

$$\delta D = -2\rho_{\infty} \int_{-b/2}^{b/2} w_{in}(y) \delta \Gamma(y) dy = 0, \text{ subject to}$$

$$\delta L = \rho_{\infty} U_{\infty} \int_{-b/2}^{b/2} \delta \Gamma(y) dy = 0 \text{ and}$$
(8a)

$$\delta M_{x,2} = \frac{1}{2} \rho_{\infty} U_{\infty} \int_{0}^{b/2} y^{2} \delta \Gamma(y) dy = \frac{1}{4} \rho_{\infty} U_{\infty} \int_{-b/2}^{b/2} y^{2} \delta \Gamma(y) dy = 0.$$
 (8b)

In order to force  $\delta D$  in Eq. (5) to be equal to zero, it is to be prescribed that

$$w_{in}(y) = -U_{\infty}[A_2 + \frac{1}{4}B_2(y/0.5b)^2], \text{ for } |y| < b/2$$
 (9a)

with  $A_2$  and  $B_2$  arbitrary dimensionless constants. To get more insight,  $w_{in}(y)$  is expressed as

$$V_{in}(y) = -U_{\infty}[\hat{A}_2 + \hat{B}_2\{1 - (y/0.5b)^2\}] = -U_{\infty}[\hat{A}_2 + \hat{B}_2(1 - \eta^2)],$$
 (9b)

 $w_{in}(y) = -U_{\infty}[\hat{A}_2 + \hat{B}_2\{1 - (y/0.5b)^2\}] = -U_{\infty}[\hat{A}_2 + \hat{B}_2(1 - \eta^2)], \tag{9b}$  with  $\hat{A}_2$  and  $\hat{B}_2$  another set of arbitrary dimensionless constants. Substitution in Eq. (2a), the inverted Biot-Savart law, gives, with the CPV integrals listed in the Appendix C:

$$\gamma_{x}(y) = \frac{4}{\pi} \frac{U_{\infty}}{\sqrt{(b/2)^{2} - y^{2}}} CPV \int_{-\frac{b}{2}}^{\frac{b}{2}} [\hat{A}_{2} + \hat{B}_{2} \{1 - (y'/0.5b)^{2}\}] \frac{((b/2)^{2} - y'^{2})^{1/2}}{y - y'} dy' 
= \frac{4}{\pi} \frac{U_{\infty}}{\sqrt{1 - \eta^{2}}} [\hat{A}_{2} CPV \int_{-1}^{1} \frac{(1 - {\eta'}^{2})^{1/2}}{\eta - \eta'} d\eta' + \hat{B}_{2} CPV \int_{-1}^{1} \frac{(1 - {\eta'}^{2})^{3/2}}{\eta - \eta'} d\eta' = \frac{4U_{\infty}\eta}{\sqrt{1 - \eta^{2}}} [\hat{A}_{2} + \hat{B}_{2} (\frac{3}{2} - \eta^{2})].$$
(9c)

It then follows from Eq. (2b), that the corresponding distribution of the circulation equals: 
$$\Gamma(y) = 4U_{\infty}[\hat{A}_2\sqrt{(b/2)^2-y^2} + \hat{B}_2\left\{\frac{1}{2}\sqrt{(b/2)^2-y^2} + \frac{1}{3}\frac{1}{(b/2)^2}((b/2)^2-y^2)^{3/2}\right\}], \text{ so that}$$

$$\Gamma(\eta) = 4U_{\infty} \left[ \hat{A}_2 \frac{b}{2} \sqrt{1 - \eta^2} + \hat{B}_2 \left\{ \frac{1}{2} \frac{b}{2} \sqrt{1 - \eta^2} + \frac{1}{3} \frac{b}{2} (1 - \eta^2)^{3/2} \right\} \right].$$

With  $\Gamma_{2,0}$  and  $\Gamma_{2,2}$  defined as  $\Gamma_{2,0}=4U_{\infty}\frac{b}{2}(\hat{A}_2+\frac{1}{2}\hat{B}_2)$  and  $\Gamma_{2,2}=4U_{\infty}\frac{b}{2}\frac{1}{3}\hat{B}_2$ , respectively, it follows

$$\Gamma(\eta) = \Gamma_{2,0} \sqrt{1 - \eta^2} + \Gamma_{2,2} (1 - \eta^2)^{3/2}, \text{ for } |\eta| < 1.$$
 (9d)

 $\Gamma(\eta) = \Gamma_{2,0} \sqrt{1 - \eta^2} + \Gamma_{2,2} (1 - \eta^2)^{3/2}, \text{ for } |\eta| < 1.$  In this notation  $\gamma_x(\eta) = \frac{2}{b} \left[ \Gamma_{2,0} \frac{\eta}{\sqrt{1 - \eta^2}} + 3\Gamma_{2,2} \eta \sqrt{1 - \eta^2} \right]$ (9e)

Since it follows that  $\hat{A}_2 = \frac{\Gamma_{2,0} - \frac{3}{2} \Gamma_{2,2}}{4U_{\infty}(b/2)}$  and  $\hat{B}_2 = \frac{3\Gamma_{2,2}}{4U_{\infty}(b/2)}$ , the induced upwash  $w_{in}(\eta)$  can be rewritten as:  $w_{in}(\eta) = -\frac{1}{2b} \left[\Gamma_{2,0} + 3\Gamma_{2,2} \left\{-\frac{1}{2} + (1 - \eta^2)\right\}\right]$ , for  $|\eta| < 1$ . (9f) In Eq. (9d), the first term in the expression for  $\Gamma(\eta)$  is the elliptic distribution that gives a constant

$$w_{in}(\eta) = -\frac{1}{2h} \left[ \Gamma_{2,0} + 3\Gamma_{2,2} \left\{ -\frac{1}{2} + (1 - \eta^2) \right\} \right], \text{ for } |\eta| < 1.$$
 (9f)

contribution to the upwash  $w_{in}(\eta)$ , i.e., the first term in Eq. (9f). The term inside the curly brackets in Eq. (9f) is the quadratic distribution of the upwash generated by the  $\Gamma_{2,2}(1-\eta^2)^{3/2}$  term in Eq. (9d). This part of the circulation distribution is the so-called bell-shaped (as coined by Reimar Horten [2], [3]) circulation distribution. At the wing tips the bell-shaped distribution has zero function value as well as zero first derivative, resulting in a wing loaded lighter near the wing tips and more heavily near the wing root. At the wing tip, circulation distribution Eq. (9d) generates an upwash distribution that is continuous at the wing tip, with a square-root singularity in its first derivative, see Figure 4. Using the expression for the circulation distribution, Eq. (9d), the lift, induced drag, root-bending-moment, etc., have been computed and collected in Table 3.

	$\Gamma(\eta) = \Gamma_{2,0} \sqrt{1 - \eta^2} + \Gamma_{2,2} \left(1 - \eta^2\right)^{3/2}$
$\frac{w_{in}( \eta <1)}{U_{\infty}}$	$-\frac{1}{2}\left[\frac{\Gamma_{2,0}}{U_{\infty}b}+3\frac{\Gamma_{2,2}}{U_{\infty}b}(-\frac{1}{2}+(1-\eta^2))\right]$
$\frac{w_{in}( \eta >1)}{U_{\infty}}$	$-\frac{1}{2}\left[\frac{\Gamma_{2,0}}{U_{\infty}b}\left(1-\frac{ \eta }{\sqrt{\eta^2-1}}\right)+3\frac{\Gamma_{2,2}}{U_{\infty}b}\left(-\frac{1}{2}+(1-\eta^2)+ \eta \sqrt{\eta^2-1}\right)\right]$
$\frac{L}{q_{\infty}b^2}$	$\frac{\pi}{2} \left[ \frac{\Gamma_{20}}{U_{\infty}b} + \frac{3}{4} \frac{\Gamma_{2,2}}{U_{\infty}b} \right]$
$\frac{L}{q_{\infty}b^2}$ $\frac{D}{q_{\infty}b^2}$	$\frac{\pi}{4} \left[ \left( \frac{\Gamma_{2,0}}{U_{\infty}b} \right)^2 + \frac{3}{2} \frac{\Gamma_{2,0}}{U_{\infty}b} \frac{\Gamma_{2,2}}{U_{\infty}b} + \frac{3}{4} \left( \frac{\Gamma_{2,2}}{U_{\infty}b} \right)^2 \right]$
$\frac{M_x}{q_{\infty}b^3}$	$\frac{1}{6} \left[ \frac{\Gamma_{2,0}}{U_{\infty}b} + \frac{3}{5} \frac{\Gamma_{2,2}}{U_{\infty}b} \right]$
$\frac{M_{x,2}}{q_{\infty}b^4}$	$\frac{\pi}{128} \left[ \frac{\Gamma_{2,0}}{U_{\infty}b} + \frac{1}{2} \frac{\Gamma_{2,2}}{U_{\infty}b} \right]$
$ \frac{M_X}{q_{\infty}b^3} $ $ \frac{M_{X,2}}{q_{\infty}b^4} $ $ \frac{M_Z}{q_{\infty}b^3} $	$\frac{-1}{12} \left[ \left( \frac{\Gamma_{2,0}}{U_{\infty}b} \right)^2 + \frac{9}{10} \frac{\Gamma_{2,0}}{U_{\infty}b} \frac{\Gamma_{2,2}}{U_{\infty}b} + \frac{27}{70} \left( \frac{\Gamma_{2,2}}{U_{\infty}b} \right)^2 \right]$
<u>ycov</u> 0.5 <i>b</i>	$\frac{\pi}{4} \left[ \frac{\Gamma_{2,0}}{U_{\infty}b} + \frac{3}{4} \frac{\Gamma_{2,2}}{U_{\infty}b} \right] / \left[ \frac{\Gamma_{2,0}}{U_{\infty}b} + \frac{\Gamma_{2,2}}{U_{\infty}b} \right]$

Table 3 – Aerodynamic performance scenario (b) minimisation of induced drag D, for prescribed free-stream conditions  $(U_{\infty}, q_{\infty})$ , lift L and starboard-integrated-bending-moment  $M_{x,2}$ : yielding circulation distribution  $\Gamma(\eta) =$  $\Gamma_{2.0}\sqrt{1-\eta^2} + \Gamma_{2.2}(1-\eta^2)^{3/2}$ .  $\eta = [y/0.5b_e]/\sigma$ ;  $\sigma = b/b_e$ 

The minimisation of the induced drag D, for prescribed lift L and prescribed starboard-span-integrated section-bending-moment  $M_{x,2}$ , comprises to consider, with wing span b some function of L and  $M_{x,2}$ :

Minimize 
$$D = q_{\infty}b^{2}\frac{\pi}{4}\left[\left(\frac{\Gamma_{2,0}}{U_{\infty}b}\right)^{2} + \frac{3}{2}\frac{\Gamma_{2,0}}{U_{\infty}b}\frac{\Gamma_{2,2}}{U_{\infty}b} + \frac{3}{4}\left(\frac{\Gamma_{2,2}}{U_{\infty}b}\right)^{2}\right],$$
 for prescribed 
$$L = q_{\infty}b^{2}\frac{\pi}{2}\left[\frac{\Gamma_{20}}{U_{\infty}b} + \frac{3}{4}\frac{\Gamma_{2,2}}{U_{\infty}b}\right]$$
 and (10)

prescribed 
$$M_{x,2} = q_{\infty}b^4 \frac{\pi}{128} \left[ \frac{\Gamma_{2,0}}{U_{\infty}b} + \frac{1}{2} \frac{\Gamma_{2,2}}{U_{\infty}b} \right],$$

with  $\Gamma(\eta) > 0$ , for  $|\eta| < 1$ .

The lift L is prescribed as  $L = L_e$ . Rather than prescribing  $M_{x,2}$ , arbitrarily, Prandtl and Betz [15] prescribed the radius *r*, associated with the radius of gyration, i.e., the inertial moment of the circulation distribution  $\Gamma(y)$ . The radius of gyration is defined as:

$$r^2 \int_0^{\frac{b}{2}} \Gamma(y) dy \equiv \int_0^{\frac{b}{2}} \Gamma(y) y^2 dy,$$

 $r^2 \int_0^{\frac{b}{2}} \Gamma(y) dy \equiv \int_0^{\frac{b}{2}} \Gamma(y) y^2 dy,$  resulting in  $r^2 = \frac{b^2}{16} \left[ \frac{\Gamma_{2,0}}{U_{\infty}b} + \frac{1}{2} \frac{\Gamma_{2,2}}{U_{\infty}b} \right] / \left[ \frac{\Gamma_{20}}{U_{\infty}b} + \frac{3}{4} \frac{\Gamma_{2,2}}{U_{\infty}b} \right],$  which is equivalent to  $r^2 = 4M_{x,2}/L$ . However, for the present study it turned out to be more insightful, and less cumbersome algebraically, to follow Klein and Viswanathan ([19], [24]), in prescribing alongside  $L=L_e$ ,  $M_{x,2}$  in terms of  $M_{x,2,e}$  as  $M_{x,2}=\tau M_{x,2,e}$ , with  $\frac{M_{X,2,e}}{q_{\infty}b_e^4} = \frac{\pi}{128} \frac{\Gamma_{0,e}}{U_{\infty}b_e}$ , see Table 2. This results in expressions in terms of the dimensionless geometric variable  $\sigma = b/b_e$ , directly related to the yet unknown span of the wing. In the present derivation, a system of linear equations is constructed for  $\Gamma_{2,0}$  and  $\Gamma_{2,2}$ , the two parameters in the circulation distribution, Eq. (9d). With  $\hat{\Gamma}_{2,k} = \Gamma_{2,k}/\Gamma_{0,e}$ , Eq. (10) yields:

$$\begin{split} \widehat{\Gamma}_{2,0} + 3/4 \widehat{\Gamma}_{2,2} &= 1/\sigma \text{ and } \\ \widehat{\Gamma}_{2,0} + 1/2 \widehat{\Gamma}_{2,2} &= \tau/\sigma^3 \, \tau \end{split}$$

which keeps the dimensionless wing span  $\sigma = b/b_e$  as geometric parameter in the optimalisation. The solution of the above system of linear equations for  $\hat{\Gamma}_{2,0}$  and  $\hat{\Gamma}_{2,2}$  is:

$$\hat{\Gamma}_{2,0} = -2/\sigma + 3\tau/\sigma^3 \text{ and } \hat{\Gamma}_{2,2} = 4/\sigma - 4\tau/\sigma^3 \tag{11a}$$

Substitution of Eq. (11a) in the expressions given in Table 3 results in the expressions listed in Table 4. Specifically, the induced drag  $D/q_{\infty}b^2$  in Table 3, divided by the induced drag  $D_e/q_{\infty}b_e^2 = \frac{\pi}{4}\left(\frac{\Gamma_{0,e}}{U_{\infty}b_e}\right)^2$  of the wing with elliptic circulation distribution and the same lift  $L=L_e$ , yields, upon some algebra:

$$\frac{D}{D_e} = \frac{1}{\sigma^6} [4\sigma^4 - 6\tau\sigma^2 + 3\tau^2]. \tag{11b}$$

The induced drag is a function of variable  $\sigma = b/b_e$  and parameter  $\tau$ . The value of the relative span  $\sigma$ for which the first derivative with respect to  $\sigma$ , of the induced drag  $D/D_e$  equals zero, is the value  $\sigma_{opt} = b/b_e$  for which the induced drag is at a local minimum. The first derivative of Eq. (11b) with

respect to 
$$\sigma$$
 equals: 
$$\frac{d}{d\sigma} \frac{D}{D_0} = -\frac{2}{\sigma^7} (2\sigma^2 - 3\tau)^2. \tag{11c}$$

	$\Gamma(\boldsymbol{\eta}) = \Gamma_{2,0} \sqrt{1 - \boldsymbol{\eta}^2} + \Gamma_{2,2} \big(1 - \boldsymbol{\eta}^2\big)^{3/2}$	Optimum: $\sigma_{opt} = \sqrt{\frac{3\tau}{2}}$
$\frac{w_{in}( \eta <1)}{U_{\infty}}$	$-\frac{1}{2}\left[\frac{\Gamma_{2,0}}{U_{\infty}b} + 3\frac{\Gamma_{2,2}}{U_{\infty}b}(-\frac{1}{2} + (1-\eta^2))\right]$	
$\frac{w_{in}( \eta >1)}{U_{\infty}}$	$-\frac{1}{2}\left[\frac{\Gamma_{2,0}}{U_{\infty}b}\left(1-\frac{ \eta }{\sqrt{\eta^2-1}}\right)+3\frac{\Gamma_{2,2}}{U_{\infty}b}\left(-\frac{1}{2}+(1-\eta^2)\right)\right]$	$+  \eta \sqrt{\eta^2 - 1})]$
$\frac{\Gamma_{2,0}}{\Gamma_{0,e}}$	$\frac{1}{\sigma^3}[-2\sigma^2+3\tau]$	0
$\frac{\Gamma_{2,2}}{\Gamma_{0,e}}$	$\frac{1}{\sigma^3}[4\sigma^2-4\tau]$	$\frac{4}{3}\sqrt{\frac{2}{3\tau}}$
$rac{L}{q_{\infty}b_{e}^{2}}$	$rac{\pi}{2}rac{\Gamma_{0,e}}{U_{\infty}b_{e}}=rac{L_{e}}{q_{\infty}b_{e}^{2}}$	
$ \frac{\frac{D}{D_e}}{\frac{M_x}{M_{x,e}}} $	$\frac{1}{\sigma^6}[4\sigma^4 - 6\tau\sigma^2 + 3\tau^2]$	$\frac{8}{9}\frac{1}{\tau}$
$\frac{M_{\chi}}{M_{\chi,e}}$	$\frac{1}{\sigma}\left[\frac{2}{5}\sigma^2 + \frac{3}{5}\tau\right]$	$\frac{2}{5}\sqrt{6\tau}$
$\frac{M_{x,2}}{M_{x,2,e}}$	τ	τ
$\frac{M_Z}{ M_{Z,e} }$	$\frac{-1}{\sigma^5} \left[ \frac{104}{35} \sigma^4 - \frac{74}{5} \tau \sigma^2 + \frac{153}{35} \tau^2 \right]$	$-\frac{24}{35}\sqrt{\frac{2}{3\tau}}$
$\frac{y_{COV}}{0.5b_e}$	$\frac{\pi}{4} \left[ \frac{\sigma^3}{2\sigma^2 - \tau} \right]$	$\frac{\pi}{4} \frac{3}{4} \sqrt{\frac{3\tau}{2}}$

Table 4 – Aerodynamic performance scenario (b) minimisation of induced drag D, for prescribed free-stream conditions  $(U_{\infty}, q_{\infty})$ , lift  $L = L_e$  and starboard-integrated section-bending-moment  $M_{x,2} = \tau M_{x,2,e}$ , as function of  $\sigma = b/b_e$ : yielding circulation distribution  $\Gamma(\eta) = \Gamma_{2,0}\sqrt{1-\eta^2} + \Gamma_{2,2}(1-\eta^2)^{3/2}$ .  $\eta = [y/0.5b_e]/\sigma$ ;  $\sigma = b/b_e$ . Third column lists performance for the optimal solution of the minimisation problem at  $\sigma_{opt} = b_{opt}/b_e = \sqrt{3\tau/2}$ .

The optimum is obtained for  $\frac{d}{d\sigma} \frac{D}{D_{\sigma}} = 0$ , which yields:

$$\sigma_{opt} = \sqrt{\frac{3\tau}{2}}$$
, for which  $\frac{D_{opt}}{D_e} = \frac{8}{9} \frac{1}{\tau}$ . (11d)

From Eq. (11c) it follows that at the optimum span  $\sigma_{opt}$ , not only the first derivative, but also the second derivative of  $D(\sigma;\tau)$  equals zero. Therefore, the minimum of  $D(\sigma;\tau)$ . is at an inflection point of  $D(\sigma;\tau)$ . From Eq. (11d) and the expressions listed in Table 4, it becomes clear that the distribution of the circulation  $\Gamma(\eta)$  that minimizes the induced drag D, for prescribed lift  $L=L_e$  and prescribed starboard span-integrated section-bending-moment  $M_{x,2}=\tau M_{x,2,e}$  is the one for which:  $\Gamma(y)=\Gamma_{2,2}(1-\eta^2)^{3/2}$ , i.e., the bell-shaped circulation distribution, for any value of  $\tau$ . For  $\tau=1$ , analysis shows that this particular bell-shaped distribution generates a factor 8/9 lower induced drag than the elliptic distribution of the circulation. This is partly due to the longer span  $\sigma_{opt}=b_{opt}/b_e=\sqrt{3/2}\approx 1.225$  of the wing featuring the bell-shaped distribution of the circulation and partly due to the differences in the induced upwash combined with differences in the circulation distribution. For  $\tau>1$  the minimum induced drag decreases further like  $D_{opt}/D_e=8/9\tau$ , while the span increases slower like  $\sigma_{opt}=b_{opt}/b_e=\sqrt{3/2}\sqrt{\tau}$ . The aerodynamic performance of wings with circulation distribution  $\Gamma(\eta)=\Gamma_{2,0}\sqrt{1-\eta^2}+\Gamma_{2,2}(1-\eta^2)^{3/2}$  is presented in Figure 4 as function of  $\sigma=b/b_e$ .

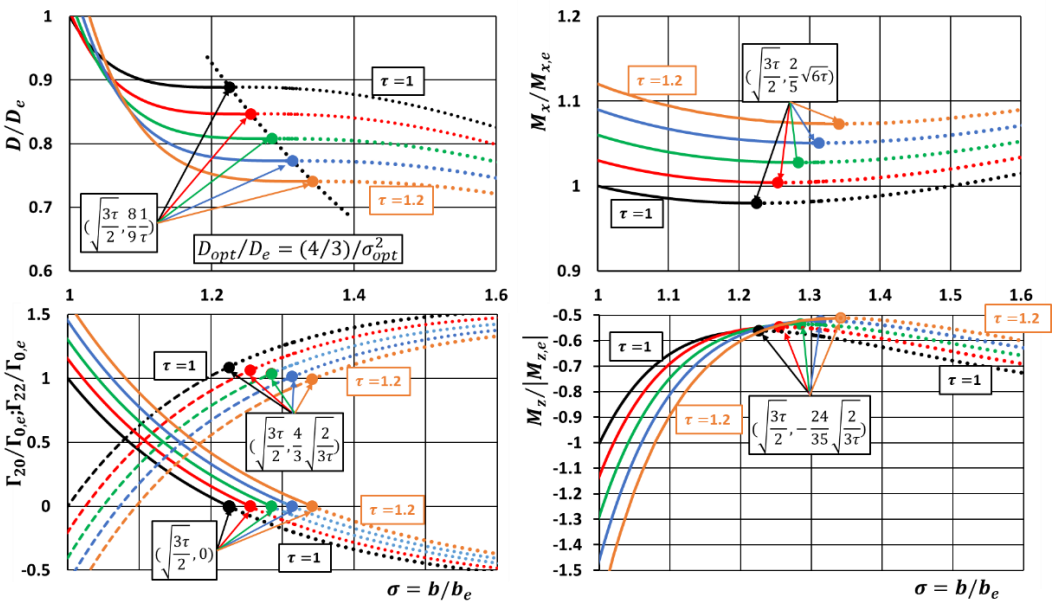


Figure 4 – Results of optimisation scenario (b): minimisation induced drag D, for prescribed free-stream conditions  $(U_{\infty},q_{\infty})$ , lift  $L=L_e$  and starboard span-integrated section-bending-moment  $M_{x,2}=\tau M_{x,2,e}$ : yielding two-term circulation distribution  $\Gamma(\eta)=\Gamma_{2,0}\sqrt{1-\eta^2}+\Gamma_{2,2}(1-\eta^2)^{3/2}$ . Results are shown for  $\tau=1.0(0.05)1.2$ , from black-to-red-to-green-to-blue-to-ochre coloured curves. Left-top: dimensionless induced drag  $D/D_e$  vs. dimensionless span  $\sigma\equiv b/b_e$ ; Left-bottom: Amplitude two contributions circulation distribution  $\Gamma_{2,0}(\sigma)/\Gamma_{0,e}$  (solid lines) and  $\Gamma_{2,2}(\sigma)/\Gamma_{0,e}$  (dashed lines); Right-top: dimensionless root-bending-moment  $M_x/M_{x,e}$  vs.  $\sigma$  and; Right-bottom: dimensionless starboard-yawing-moment  $M_z/M_{z,e}$  vs.  $\sigma$ . Dotted lines: invalid solutions for which  $\Gamma(\eta)$  not positive for all  $|\eta|<1$ . Coloured round solid circles: optimum solution of minimum induced drag.

From Figure 4 it becomes clear that, with increasing  $\tau=M_{x,2}/M_{x,2,e}>1$ , the semi-span required for the minimisation of the induced drag, increases slowly as  $\sigma=b/b_e\sim\sqrt{\tau}$ , from 22.5% for  $\tau=1$  to 34.2% for  $\tau=1.2$ . The optimal induced drag decreases from  $D_{opt}/D_e=8/9\approx0.8889$  for  $\tau=1$  to  $D_{opt}/D_{opt}/D_{opt}$  for  $D_{opt}/D_{opt}/D_{opt}/D_{opt}$  for  $D_{opt}/D_{opt}/D_{opt}/D_{opt}/D_{opt}/D_{opt}/D_{opt}/D_{opt}$  for  $D_{opt}/D_$ 

of  $\tau$ , the root-bending-moment is at its minimum when the induced drag is at its minimum.

For any value of  $\tau$ , the starboard-yawing moment  $M_z/|M_{z,e}|$  remains negative, though its magnitude decreases quite rapidly with increasing  $\sigma = b/b_e$ , attaining its minimum when the induced drag is at its minimum. For increasing values of  $\tau$ , the magnitude of  $M_z/|M_{z,e}|$  decreases to increasingly smaller values. The reason is that in the wing-tip region the section drag becomes negative (thrust rather than drag), which gives a positive (proverse) contribution to the yawing moment. This is advantageous for turning flight, since this leads to a smaller vertical tail surface, or even elimination of the vertical tail.

Figure 5 presents results for three values of  $\tau = M_{x,2}/M_{x,2,e}$ :  $\tau = 1.0$ , 1.1 and 1.2, values in the same range as the ones used in Figure 4. Furthermore, for the dimensionless wing span  $\sigma = b/b_e$ , we choose, for each value of  $\tau$ , the value at which the induced drag is minimal:  $\sigma_{opt} = b_{opt}/b_e = \sqrt{3\tau/2}$ . This implies that the corresponding circulation distributions have  $\Gamma_{20} = 0$ , corresponding to bell-shaped distributions  $\Gamma_{opt}(\eta) = (4/3)\sqrt{2/3\tau}(1-\eta^2)^{3/2}$ . Results are compared with results for the elliptic circulation distribution. Figure 5 shows that with increasing  $\tau = M_{x,2}/M_{x,2,e}$  the dimensionless section circulation  $\Gamma_{opt}(y/0.5b_e)/\Gamma_{0,e}$ , which is proportional to the dimensionless section lift:  $\ell(y/0.5b_e)/q_{\infty}b_e = 2\Gamma(y/0.5b_e)/q_{\infty}b_e$ , see Table 1, decreases near the wing root, which is due to the increase in dimensionless span  $\sigma = b_{opt}/b_e$  at constant total lift, i.e., the lift for the elliptic distribution.

Figure 5 confirms that the bell-shaped circulation distribution generates a quadratic distribution of the upwash  $w_{in} (y/0.5b_e)/U_{\infty}$  on the lifting line, negative in the wing-root portion of the wing, positive in about 30-percent of the outboard part of the semi-span. The elliptic circulation distribution generates a constant (negative) upwash. As will be clear later on, this difference in upwash distribution has implications for the roll-up of the wake of the wing.

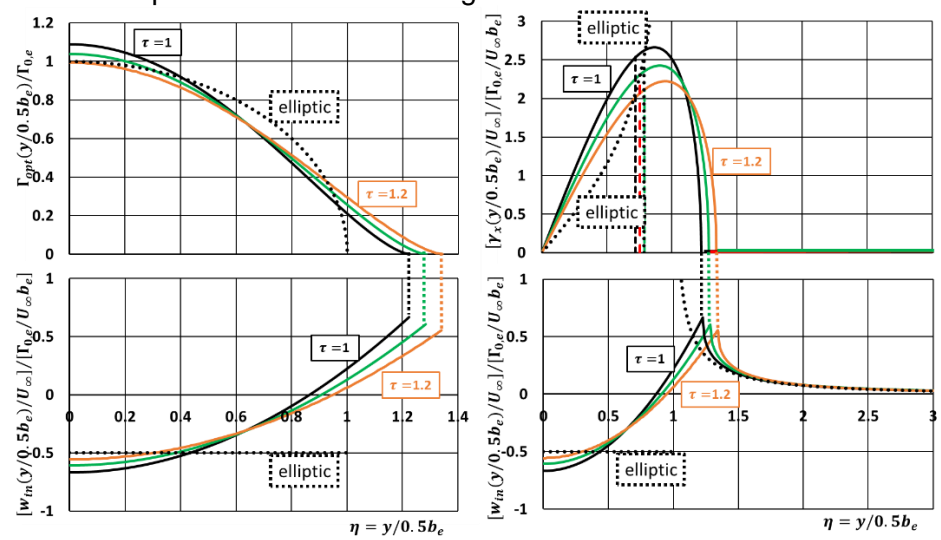


Figure 5 - Results optimisation scenario (b): minimisation of induced drag D, for prescribed free-stream conditions  $(U_{\infty},q_{\infty})$ , lift  $L=L_e$  and starboard-integrated section-bending moment  $M_{x,2}=\tau M_{x,2,e}$ : yielding two-term circulation distribution  $\Gamma(\eta)=\Gamma_{2,0}\sqrt{1-\eta^2}+\Gamma_{2,2}(1-\eta^2)^{3/2}$ . Results are shown for  $\tau=1.0(0.1)1.2$ , from black-togreen-ochre coloured curves.  $\eta=(y/0.5b_e)/\sigma$ ; Minimum drag:  $\sigma=\sigma_{opt}=b_{opt}/b_e=\sqrt{3\tau/2}$ ,  $\Gamma_{2,0}=0$ . Top-left: spanwise distributions dimensionless circulation  $\Gamma_{opt}(y/0.5b_e)/\Gamma_{0,e}$  vs.  $y/0.5b_e$ ; Bottom-left: spanwise distributions dimensionless upwash velocity  $[w_{in}~(y/0.5b_e)/U_{\infty}]/[\Gamma_{0,e}/U_{\infty}b_e]$  vs.  $y/0.5b_e$ ; Top-right: spanwise distributions sionless vortex distribution  $[\gamma_x~(y/0.5b_e)/U_{\infty}]/[\Gamma_{0,e}/U_{\infty}b_e]$  vs.  $y/0.5b_e$ ; Bottom-right: spanwise distributions dimensionless upwash velocity  $[w_{in}~(y/0.5b_e)/U_{\infty}]/[\Gamma_{0,e}/U_{\infty}b_e]$  vs.  $y/0.5b_e$  on lifting line and its extension y>b. Vertical dashed lines: location COV. Results for elliptic circulation distribution: black dotted curves.

The vortex distribution along the lifting line decreases in peak value with increasing value of  $\tau$ . The location of the peak, at  $y_{peak}/0.5b_e = \sigma_{opt}/\sqrt{2} = \sqrt{3\tau}/2$ , as well as the location of the center-of-vorticity (COV) at  $y_{cov}/0.5b_e = (3\pi/16) \, \sigma_{opt} = (3\pi/16) \, \sqrt{3\tau/2} < y_{peak}/0.5b_e$ , both move outboard with increasing  $\tau$ . For  $0.823 = \pi^2/12 < \tau < 32/27 = 1.185$ . the COV for the elliptic distribution, at  $y_{cov,e}/0.5b_e = \pi/4$ , is situated between  $y_{cov}/0.5b_e$  and  $y_{peak}/0.5b_e$ . For  $\tau > 32/27 = 1.185$ ,  $y_{cov,e}/0.5b_e < y_{cov}/0.5b_e$ , so inboard of both  $y_{cov}/0.5b_e$  and  $y_{peak}/0.5b_e$ . Figure 5, bottom-right presents the upwash distribution for y > b, along the extension of the lifting line. It shows that, characteristic for bell-shaped circulation distributions, the upwash distribution:

- (i) is continuous in function value across the wing tip;
- (ii) is slope-discontinuous across the wing tip: the slope is finite at the inboard side of the wing tip, but has a square-root singularity at the outboard side;
- (iii) tends to zero for points far outboard of the wing tip, as should be the case for any circulation distribution.

Figure 6 shows that for the elliptic distribution  $\Gamma_{0,e}\sqrt{1-\eta^2}$  of the circulation, the distribution of the section- drag  $d(y/0.5b_e)/q_\infty b_e$  of the wing is positive along the whole span of the wing, while for the bell-shaped circulation distribution  $\Gamma_{2,2}(1-\eta^2)^{3/2}$  the tip portion of the wing features much lower and even negative section-drag (section-thrust). In the root portion of the wing, the bell-shaped circulation distribution generates a higher section-drag, however, for the wing as a whole the net effect is a decrease in overall induced drag, like  $1/\tau$ .

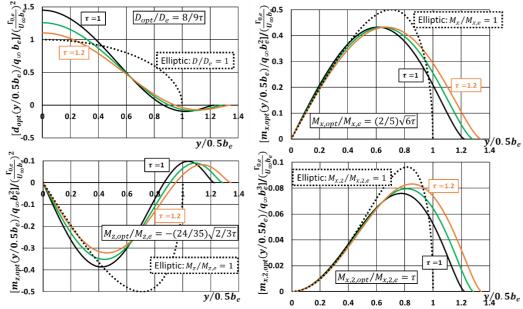


Figure 6 - Results optimisation scenario (b): minimisation of induced drag D, for prescribed free-stream conditions  $(U_{\infty},q_{\infty})$ , lift  $L=L_e$  and starboard-integrated section-bending-moment  $M_{x,2}=\tau M_{x,2,e}$ : yielding two-term circulation distribution  $\Gamma(\eta)=\Gamma_{2,0}\sqrt{1-\eta^2}+\Gamma_{2,2}(1-\eta^2)^{3/2}$ , with. Results are shown for  $\tau=1.0(0.1)1.2$ , from black-togreen-to-ochre coloured curves.  $\eta=(y/0.5b_e)/\sigma$ ;  $\sigma=\sigma_{opt}=b_{opt}/b_e=\sqrt{3\tau/2}$ . Left-top: spanwise distributions dimensionless section drag  $[d_{opt}(y/0.5b_e)/q_{\infty}b_e]/(\Gamma_{0,e}/U_{\infty}b_e)^2$  vs.  $y/0.5b_e$ ; Left-bottom: spanwise distributions dimensionless section yawing moment  $[m_{z,opt}(y/0.5b_e)/q_{\infty}b_e^2]/(\Gamma_{0,e}/U_{\infty}b_e)^2$  vs.  $y/0.5b_e$ . Right-top: spanwise distributions dimensionless root-bending-moment  $[m_{x,opt}(y/0.5b_e)/q_{\infty}b_e^2]/(\Gamma_{0,e}/U_{\infty}b_e)$ . Results for elliptic circulation distribution: black dotted curves.

It is also clear that increasing  $\tau$  does not change the section-thrust in the tip region very much, while in the wing-root portion of the wing the section-drag decreases substantially. This is the reason that for the optimal case, the overall drag decreases for increasing  $\tau$ .

Since  $m_z(y) = -d(y)y$ , the section contribution  $m_z(y/0.5b_e)/q_\infty b_e^2$  to the starboard-yawing moment  $M_z/q_\infty b_e^3$ , it is clear that for the bell-shaped distributions the yawing moment is much smaller than for the elliptic circulation distribution. For increasing  $\tau = M_{x,2}/M_{x,2,e}$ , the yawing moment quite drastically decreases the magnitude of the negative, adverse, yawing moment, see Figure 4.

The plot of the distributions of the section contribution to the root-bending-moment  $m_x(y)$ , indicates that the root-bending moment due to the bell-shaped distributions and that due to the elliptic circulation distribution behave about the same. For  $\tau = M_{x,2}/M_{x,2,e} = 1$ ,  $M_x/M_{x,e} \approx 0.98$ , while for  $\tau = 1.1$  and 1.2,  $M_x/M_{x,e} \approx 1.03$  and 1.07, respectively, slowly increasing like  $\sqrt{\tau}$ . As far as the distributions of the contribution to the integrated-bending-moment  $m_{x,2}(y)$ , is concerned, it is seen that:

- (i) for  $\tau=1$  and for the elliptic distribution, the corresponding integrated-bending-moments are equal:  $M_{x,2,opt}/M_{x,2,e}=\tau=1$  and  $M_{x,2,e}/M_{x,2,e}=1$ . Therefore, since the span of the optimal wing is longer, the distribution is less peaky.
- (ii) For  $\tau > 1$   $M_{x,2,opt}/M_{x,2,e} = \tau > 1$  increases, so that the distribution of  $m_{x,2}(y)$  shifts towards the wing tip and simultaneously its amplitude increases.

Comparison with results of Prandtl [15]

The results presented in the present section agree with the results presented by Prandtl [15], though the present study considers further details on aerodynamic performance. Note that there is a difference in choice of the form of the expression for the circulation distribution: in our case  $\Gamma(\eta) =$  $\Gamma_{2,0}\sqrt{1-\eta^2} + \Gamma_{2,2}(1-\eta^2)^{3/2}$ ; in Prandtl's case  $\Gamma(\eta) = \Gamma_{0,P}[1-\mu\eta^2]\sqrt{1-\eta^2}$ . Here  $\mu$  is the aerodynamic parameter that Prandtl varied in the optimisation. The relation between the two formulations is:

$$\Gamma_{0,P} = \Gamma_{2,0} + \Gamma_{2,2}$$
 and  $\mu = \Gamma_{2,2}/(\Gamma_{2,0} + \Gamma_{2,2})$ .

Substituting Eqs. (11a) results in  $\Gamma_{0,P} = \Gamma_{0,e}(\frac{2}{\sigma} - \frac{\tau}{\sigma^3})$  and  $\mu = 4(\sigma^2 - \tau)/(2\sigma^2 - \tau)$ .

The optimal values are found for  $\sigma=\sigma_{opt}=b_{opt}/b_e=\sqrt{3\tau/2}$ , i.e.,  $\Gamma_{0,P,opt}=\Gamma_{0,e}\frac{4}{3}\sqrt{2/3\tau}$  and  $\mu_{opt}=1$ . This means that  $\Gamma_{2,0}=0$ : the circulation distribution is the bell-shaped distribution  $\Gamma(\eta)=\Gamma_{0,P}(1-\eta^2)^{3/2}$ . Clearly,  $\mu_{opt} = 1$  agrees with the value found by Prandtl [15], resulting in  $D/D_e = 8/9$  and  $b_{opt}/b_e =$  $\sqrt{3/2}$ . In other words, a decrease in induced drag of 11.1% and an optimal span 22.5% longer than the span of the wing with elliptic distribution of the wing load at the same lift  $L = L_e$ .

A remarkable difference is found in the circulation distributions, which in Figure 1 of [15] appears to have the same value of  $\Gamma(\eta = 0)$  for the three distributions shown, while in our Figure 5 upper-left,  $\Gamma(\eta=0)$  is larger for  $\tau=1$  than for the elliptic distribution. Also, there is a typo in the formula heading the most-right column in the table above Figure 1 in [15]: the power 2 should be within the brackets.

## 3.3 Minimization Induced Drag for prescribed Lift and prescribed Root-Bending-Moment

For scenario (c), the optimisation is for constant lift L, and for constant starboard-side root-bending moment  $M_x$ . Now the variation  $\delta L$  of the lift L in combination with zero variation  $\delta M_x$  of  $M_x$ , due to the variation in  $\Gamma(y)$  should be zero, i.e., see Appendix B:

$$\delta D = -2\rho_{\infty} \int_{-b/2}^{b/2} w_{in}(y) \delta \Gamma(y) dy = 0, \text{ subject to}$$

$$\delta L = \rho_{\infty} U_{\infty} \int_{-b/2}^{b/2} \delta \Gamma(y) dy = 0 \text{ and}$$
(13a)

$$\delta L = \rho_{\infty} U_{\infty} \int_{-h/2}^{b/2} \delta \Gamma(y) dy = 0 \text{ and}$$
 (13a)

$$\delta M_x = \rho_\infty U_\infty \int_0^{b/2} y \delta \Gamma(y) dy = 0. \tag{13b}$$
 In order to force  $\delta D$  in Eq. (5) to be equal to zero, it is to be prescribed that for the present case

$$w_{in}(y) = U_{\infty}[A + B\frac{b}{2}|\eta|], \text{ for } |y| < b/2$$
 , (14a)

Substitution in the inverted Biot-Savart law, Eq. (2a), gives, using the integrals listed in Appendix C:

$$\gamma_{x}(\eta) = -4U_{\infty}A\frac{\eta}{\sqrt{1-\eta^{2}}} - \frac{4U_{\infty}}{\pi}Bb\{\frac{\eta}{\sqrt{1-\eta^{2}}} - \eta\ln\frac{1+\sqrt{1-\eta^{2}}}{|\eta|}\},$$
It then follows from Eq. (2b), that the corresponding distribution of the circulation equals:

$$\Gamma(y) = -4U_{\infty} \frac{b}{2} A \sqrt{1 - \eta^2} - \frac{4}{\pi} U_{\infty} (\frac{b}{2})^2 B (\sqrt{1 - \eta^2} + \eta^2 \ln \frac{1 + \sqrt{1 - \eta^2}}{|\eta|}),$$

which upon defining  $\Gamma_0 = -4U_{\infty}\frac{b}{2}A$  and  $\Gamma_1 = -\frac{4}{\pi}U_{\infty}(\frac{b}{2})^2B$ , is re-expressed as

$$\Gamma(\eta) = \Gamma_0 \sqrt{1 - \eta^2} + \Gamma_1 (\sqrt{1 - \eta^2} + \eta^2 \ln \frac{1 + \sqrt{1 - \eta^2}}{|\eta|}), \text{ for } |\eta| < 1,$$
(14c)

while 
$$\frac{w_{in}(\eta)}{U_{\infty}} = -\frac{1}{2U_{\infty}b} [\Gamma_0 + \Gamma_1 \pi |\eta|]$$
, for  $|\eta| < 1$ . (14d)

In this notation 
$$\gamma_x(\eta) = \frac{2}{b} \left[ \Gamma_0 \frac{\eta}{\sqrt{1-\eta^2}} + 2\Gamma_1 \left( \frac{\eta}{\sqrt{1-\eta^2}} - \eta \ln \frac{1+\sqrt{1-\eta^2}}{|\eta|} \right) \right]$$
 (14e)

Note: in the present study Eq. (14e) has been derived independently. However, in 1950, R.T. Jones ([17], Eq. (13)) derived an expression similar to Eq. (14c) for the circulation distribution that solves the present minimisation problem. Rather than using the natural-logarithmic term, Jones used the inverse-hyperbolic-cosine  $\cosh^{-1}(1/|\eta|)$  in his formulation. However, since  $\ln \frac{1+\sqrt{1-\eta^2}}{|\eta|} = \cosh^{-1}(1/|\eta|)$ , Jones' formulation and the present one are fully equivalent. Also, Klein and Viswanathan [19] presented the expression for the bell-shaped solution for scenario (c) with  $\ln \frac{1+\sqrt{1-\eta^2}}{\ln l}$  expressed as

$$-\frac{1}{2}\ln\frac{1-\sqrt{1-\eta^2}}{1+\sqrt{1-\eta^2}}$$

From the expression for the distribution of the circulation, Eq. (14c), the lift, induced drag, root-bending moment, etc., have been determined, see Table 5.

The minimisation of the induced drag D, at prescribed lift L and prescribed root-bending moment  $M_x$ , requires to consider b as some function of L and  $M_x$ :

Minimize 
$$D = q_{\infty}b^{2}\frac{\pi}{4}\left[\left(\frac{\Gamma_{0}}{U_{\infty}b}\right)^{2} + \frac{8}{3}\frac{\Gamma_{0}}{U_{\infty}b}\frac{\Gamma_{1}}{U_{\infty}b} + 2\left(\frac{\Gamma_{1}}{U_{\infty}b}\right)^{2}\right],$$
 for prescribed 
$$L = q_{\infty}b^{2}\frac{\pi}{2}\left[\frac{\Gamma_{0}}{U_{\infty}b} + \frac{4}{3}\frac{\Gamma_{1}}{U_{\infty}b}\right] \text{ and}$$
 prescribed 
$$M_{\chi} = q_{\infty}b^{3}\frac{1}{6}\left[\frac{\Gamma_{0}}{U_{\infty}b} + \frac{3}{2}\frac{\Gamma_{1}}{U_{\infty}b}\right].$$

Similar to scenario (b), rather than working directly with L and  $M_x$ , one could consider the radius  $r_1$ , associated with the center-of-gravity of the circulation distribution  $\Gamma(y)$ :

$$r_1 \int_0^{\frac{b}{2}} \Gamma(y) dy \equiv \int_0^{\frac{b}{2}} \Gamma(y) y dy.$$

However, in the present study the span b is used as the optimisation parameter in the formulation, which is less cumbersome algebraically.

$\Gamma(\eta) = \Gamma_0 \sqrt{1-\eta^2} + \Gamma_1 (\sqrt{1-\eta^2} + \eta^2 \ln \frac{1+\sqrt{1-\eta^2}}{ \eta })$	Function of $\frac{\Gamma_0}{U_{\infty}b}, \frac{\Gamma_1}{U_{\infty}b}$ and $b$
$\frac{w_{in}( \eta <1)}{U_{\infty}}$	$rac{-1}{2}[rac{\Gamma_0}{U_{\infty}b}+rac{\Gamma_1}{U_{\infty}b}\pi \eta ]$
$\frac{w_{in}( \eta >1)}{U_{\infty}}$	$\frac{-1}{2} \left[ \frac{\Gamma_0}{U_{\infty}b} \left( 1 - \frac{ \eta }{\sqrt{\eta^2 - 1}} \right) + \frac{2\Gamma_1}{U_{\infty}b} \left( \frac{- \eta }{\sqrt{\eta^2 - 1}} + \eta \arcsin\left(\frac{1}{\eta}\right) \right) \right]$
$\frac{L}{q_{\infty}b^2}$	$\frac{\pi}{2} \left[ \frac{\Gamma_0}{U_{\infty}b} + \frac{4}{3} \frac{\Gamma_1}{U_{\infty}b} \right]$
$\frac{L}{q_{\infty}b^2}$ $\frac{D}{q_{\infty}b^2}$	$\frac{\pi}{4} \left[ \left( \frac{\Gamma_0}{U_{\infty}b} \right)^2 + \frac{8}{3} \frac{\Gamma_0}{U_{\infty}b} \frac{\Gamma_1}{U_{\infty}b} + 2 \left( \frac{\Gamma_1}{U_{\infty}b} \right)^2 \right]$
$\frac{M_x}{q_{\infty}b^3}$	$\frac{1}{6} \left[ \frac{\Gamma_0}{U_{\infty}b} + \frac{3}{2} \frac{\Gamma_1}{U_{\infty}b} \right]$
$\frac{M_{\chi,2}}{q_{\infty}b^4}$	$\frac{\pi}{128} \left[ \frac{\Gamma_0}{U_{\infty}b} + \frac{8}{5} \frac{\Gamma_1}{U_{\infty}b} \right]$
$ \frac{M_X}{q_{\infty}b^3} $ $ \frac{M_{X,2}}{q_{\infty}b^4} $ $ \frac{M_Z}{q_{\infty}b^3} $	$\frac{-1}{12} \left[ \left( \frac{\Gamma_0}{U_{\infty}b} \right)^2 + \frac{3}{2} \left( 1 + \frac{\pi^2}{8} \right) \frac{\Gamma_0}{U_{\infty}b} \frac{\Gamma_1}{U_{\infty}b} + \frac{3}{10} \pi^2 \left( \frac{\Gamma_1}{U_{\infty}b} \right)^2 \right]$
$\eta_{cov} = y_{cov}/0.5b$	$\frac{\pi}{4} \frac{(\frac{\Gamma_0}{U_{\infty}b} + \frac{4}{3U_{\infty}b})}{(\frac{\Gamma_0}{U_{\infty}b} + \frac{\Gamma_1}{U_{\infty}b})}$

Table 5 – Aerodynamic performance for scenario (c): minimisation of induced drag D, for prescribed free-stream conditions  $(U_{\infty}, q_{\infty})$ , lift L and root-bending moment  $M_x$ , yielding circulation distribution  $\Gamma(\eta) = \Gamma_0 \sqrt{1 - \eta^2} + 1$  $\Gamma_1 \{ \sqrt{1 - \eta^2} + \eta^2 \ln \frac{1 + \sqrt{1 - \eta^2}}{|\eta|} \}.$ 

Remark: Evaluating the upwash for  $|\eta| > 1$  is not trivial. The integral is not found in Integral Tables. However, expanding  $1/(\eta - \eta')$  in the integrand in Eq. (2d) for large values of  $\eta$ , the evaluation of the sub-integrals is obtained, in closed form, as an infinite series that appears to converge. The resulting series is then recognised as the expansion of  $\eta \arcsin(1/\eta)$ .

Following Klein and Viswanathan ([19], [24]), the prescribed lift L is expressed in terms of the lift  $L_e$  generated by the elliptic distribution of the circulation, at the same free-stream conditions, of a wing with given span  $b_e$ . With  $\Gamma_{0,e}$  the amplitude of the circulation of this imaginary wing, the circulation distribution equals  $\Gamma(\eta) = \Gamma_{0,e} \sqrt{1 - \eta^2}$ . Using the expression in Table 2 for the lift of such a distribution,

$$\frac{L_e}{q_{\infty}b_e^2} = \frac{\pi}{2} \frac{\Gamma_{0,e}}{U_{\infty}b_e},$$

subsequently defines  $\Gamma_{0,e}$ . The prescribed root-bending moment  $M_x$  is expressed as a factor  $\lambda$  times the root-bending moment  $M_{x,e}$  of the elliptic distribution:  $M_x = \lambda M_{x,e}$ , see Table 2:  $\frac{M_{x,e}}{q_{\infty}b_e^3} = \frac{1}{6} \frac{\Gamma_{0,e}}{U_{\infty}b_e}.$ 

$$\frac{M_{x,e}}{q_{\infty}b_e^3} = \frac{1}{6} \frac{\Gamma_{0,e}}{U_{\infty}b_e}.$$

Then a system of linear equations is constructed for the two parameters ( $\Gamma_0$  and  $\Gamma_1$ ) in the expression, Eq. (14c), for the circulation distribution. This gives, with  $\hat{\Gamma}_k = \Gamma_k/\Gamma_{0,e}$  and  $\sigma = b/b_e$ :

$$\hat{\Gamma}_0 + 4/3\hat{\Gamma}_1 = 1/\sigma$$
 and  $\hat{\Gamma}_0 + 3/2\hat{\Gamma}_1 = \lambda/\sigma^2$ 

The solution of this system of linear equations for  $\widehat{\Gamma}_0$  and  $\widehat{\Gamma}_1$  is:

$$\hat{\Gamma}_0 = 9/\sigma - 8\lambda/\sigma^2 \text{ and } \hat{\Gamma}_1 = -6/\sigma + 6\lambda/\sigma^2$$
 (16a)

Substitution of Eq. (16a) in the expression for the induced drag  $\frac{D}{q_{\infty}p^2}$  in Table 5, divided by the induced drag  $\frac{D_e}{q_{\infty}b_e^2} = \frac{\pi}{4} \left(\frac{\Gamma_{0,e}}{U_{\infty}b_e}\right)^2$  of the wing with elliptic circulation distribution, yields, upon some algebra:  $\frac{D}{D_e} = \hat{\Gamma}_0^2 + \frac{8}{3} \hat{\Gamma}_0 \hat{\Gamma}_1 + 2\hat{\Gamma}_1^2$ .

$$\frac{D}{D_e} = \hat{\Gamma}_0^2 + \frac{8}{3} \hat{\Gamma}_0 \hat{\Gamma}_1 + 2\hat{\Gamma}_1^2. \tag{16b}$$

Substitution of Eq. (16a) gives:

$$\frac{D}{D_e} = \frac{1}{\sigma^4} [9\sigma^2 - 16\lambda\sigma + 8\lambda^2]. \tag{16c}$$

The induced drag is a function of the variable  $\sigma = b/b_e$ , i.e., the relative span and of the parameter  $\lambda$ . The value of the relative span  $\sigma$  for which the first derivative, with respect to  $\sigma$ , of the induced drag  $D/D_e$  equals zero, is the value  $\sigma = \sigma_{opt} = b_{opt}/b_e$  for which the induced drag is at a local minimum. The first derivative of Eq. (16c) equals:  $\frac{d}{d\sigma} \frac{D}{D_e} = -\frac{2}{\sigma^5} (3\sigma - 4\lambda)^2.$ 

$$\frac{d}{d\sigma} \frac{D}{D_{\sigma}} = -\frac{2}{\sigma^5} (3\sigma - 4\lambda)^2. \tag{16d}$$

The optimum is obtained for  $\frac{d}{d\sigma} \frac{D}{D_e} = 0$ , which yields:  $\sigma_{opt} = \frac{4}{3}\lambda$ , for which  $\frac{D_{opt}}{D_e} = \frac{27}{32}\frac{1}{\lambda^2}$ . (16e)

Eq. (16d) reveals that at the optimum span  $\sigma_{opt}$ , the first derivative and also the second derivative of the induced drag equals zero. Therefore, the minimum of  $D(\sigma; \lambda)$  is at an inflection point of  $D(\sigma; \lambda)$ . Now the aerodynamics performance of the wing can be expressed in terms of the prescribed variables L,  $M_x$  and of the unknown wing span b, or equivalently  $\sigma$  and  $\lambda$ , see Table 6 below.

	$\Gamma(\eta) = \Gamma_0 \sqrt{1-\eta^2} + \Gamma_1 [\sqrt{1-\eta^2} + \eta^2 ln \frac{1+\sqrt{1-\eta^2}}{ \eta }]$	Optimum: $\sigma_{opt} = \frac{4}{3}\lambda$
$\frac{w_{in}( \eta <1)}{U_{\infty}}$	$-rac{1}{2}[rac{\Gamma_0}{U_{\infty b}}+rac{\Gamma_1}{U_{\infty b}}\pi \eta ]$	
$\frac{w_{in}( \eta >1)}{U_{\infty}}$	$-\frac{1}{2} \left[ \frac{\Gamma_0}{I_{\infty b}} \left( 1 - \frac{ \eta }{\sqrt{\eta^2 - 1}} \right) + \frac{2\Gamma_1}{I_{\infty b}} \left( \frac{- \eta }{\sqrt{\eta^2 - 1}} + \eta \arcsin(1/ \eta ) \right) \right]$	
$\frac{\Gamma_0}{\Gamma_{0,e}}$	$\frac{1}{\sigma^2}[9\sigma - 8\lambda]$	$\frac{9}{4\lambda}$
$\begin{array}{c} \frac{\Gamma_0}{\Gamma_{0,e}} \\ \frac{\Gamma_1}{\Gamma_{0,e}} \\ \frac{L_e}{q_{\infty}b_e^2} \end{array}$	$\frac{1}{\sigma^2}[-6\sigma+6\lambda]$	$-\frac{9}{8\lambda}$
$\frac{L_e}{q_{\infty}b_e^2}$	$\frac{\pi}{2} \frac{\Gamma_{0,e}}{U_{\infty}b_{e}}$	
$\frac{D}{D_e}$	$\frac{1}{\sigma^4}[9\sigma^2 - 16\lambda\sigma + 8\lambda^2]$	$\frac{27}{32} \frac{1}{\lambda^2}$
$\frac{M_{\chi}}{M_{\chi,e}}$	λ	λ
$ \frac{D_e}{D_e} $ $ \frac{M_X}{M_{x,e}} $ $ \frac{M_{x,2}}{M_{x,2,e}} $	$\sigma \frac{1}{5}[-3\sigma + 8\lambda]$	$\frac{16}{15}\lambda^2$
$\frac{M_z}{ M_{z,e} }$	$\frac{-1}{\sigma^3} \left[ \lambda (9\sigma - 8\lambda) + \frac{27}{40} \pi^2 (\sigma - \lambda) (\sigma - \frac{8}{3} \lambda) \right]$	$-\frac{27}{16}(1-\frac{3}{40}\pi^2)\frac{1}{\lambda}$
$\frac{y_{COV}}{0.5b_e}$	$\frac{\pi}{4} \left[ \frac{\sigma^2}{3\sigma - 2\lambda} \right]$	$\frac{2\pi}{9}\lambda$

Table 6 – Aerodynamic performance for scenario (c) minimisation of induced drag D, for prescribed free-stream conditions  $(U_{\infty},q_{\infty})$ , lift  $L=L_e$  and root-bending moment  $M_{\chi}=\lambda M_{\chi,e}$ , yielding circulation distribution  $\Gamma(\eta)=1$  $\Gamma_0 \sqrt{1 - \eta^2} + \Gamma_1 \{ \sqrt{1 - \eta^2} + \eta^2 \ln \frac{1 + \sqrt{1 - \eta^2}}{|\eta|} \}.$ 

From Figure 7 it becomes clear that, with increasing  $\lambda = M_x/M_{x,e}$ , the semi-span required for the minimisation of the induced drag, increases linearly as  $\sigma = b/b_e \sim \lambda$ , from 27.6% for  $\lambda = 0.95$  to 46.7% for  $\lambda$  = 1.1. The optimal induced drag decreases quadratically with  $\lambda$  from  $D_{opt}/D_e$  = 0.934 for  $\lambda$  = 0.95 to  $D_{opt}/D_e$  = 0.697 for  $\lambda$  = 1.1. The latter is a decrease in induced drag by almost 30%, for a span increase of 46.7%. This indicates that a small increase in root-bending moment  $M_x = \lambda M_{x,e}$ vields a substantial decrease in minimum induced drag.

Also clear from Figure 7 is that the optimal condition requires that the amplitude  $\Gamma_0/\Gamma_{0,e}$  of the elliptic part of the distribution and the amplitude  $\Gamma_1/\Gamma_{0,e}$  of the natural-logarithmic part of the circulation distribution should be related as  $\Gamma_1 = -\Gamma_0/2$ . Therefore, the optimal circulation distribution follows from

$$\Gamma_{opt}(\eta) = \frac{1}{2} \Gamma_0 \left[ \sqrt{1 - \eta^2} - \eta^2 \ln \frac{1 + \sqrt{1 - \eta^2}}{|\eta|} \right]. \tag{17a}$$

The corresponding optimal vortex distribution then reads, see Eq. (14e):

$$\gamma_{x,opt}(\eta) = \frac{2}{b} \Gamma_0 \eta \ln \frac{1 + \sqrt{1 - \eta^2}}{|\eta|},\tag{17b}$$

which shows that the vortex distribution is zero at the wing tip, i.e., the circulation distribution features not only zero function value, but also zero derivative at the wing tip, i.e., Eq. (17a) is our second bellshaped distribution.

The associated distribution of the upwash follows from Eq. (14d) as:

$$\frac{w_{in,opt}(\eta)}{U_{\infty}} = -\frac{1}{2} \frac{\Gamma_0}{U_{\infty}b} [1 - 0.5\pi |\eta|], \text{ for } |\eta| < 1, \tag{17c}$$

which is indeed a linear distribution of the upwash along the lifting line. For points at the outward extension of the lifting line, the distribution of the upwash follows, with  $\Gamma_1 = -0.5\Gamma_0$  from Table 6 as:

$$\frac{w_{in,opt}(\eta)}{U_{\infty}} = -\frac{1}{2} \frac{\Gamma_0}{U_{\infty}b} [1 - \eta \arcsin(1/|\eta|)], \text{ for } |\eta| > 1.$$
 (17d)

Evaluation of Eqs. (17c) and (17d) at the wing tip  $|\eta| = 1$ , shows that in the optimal case, the distribution of the upwash is continuous at the wing tip.

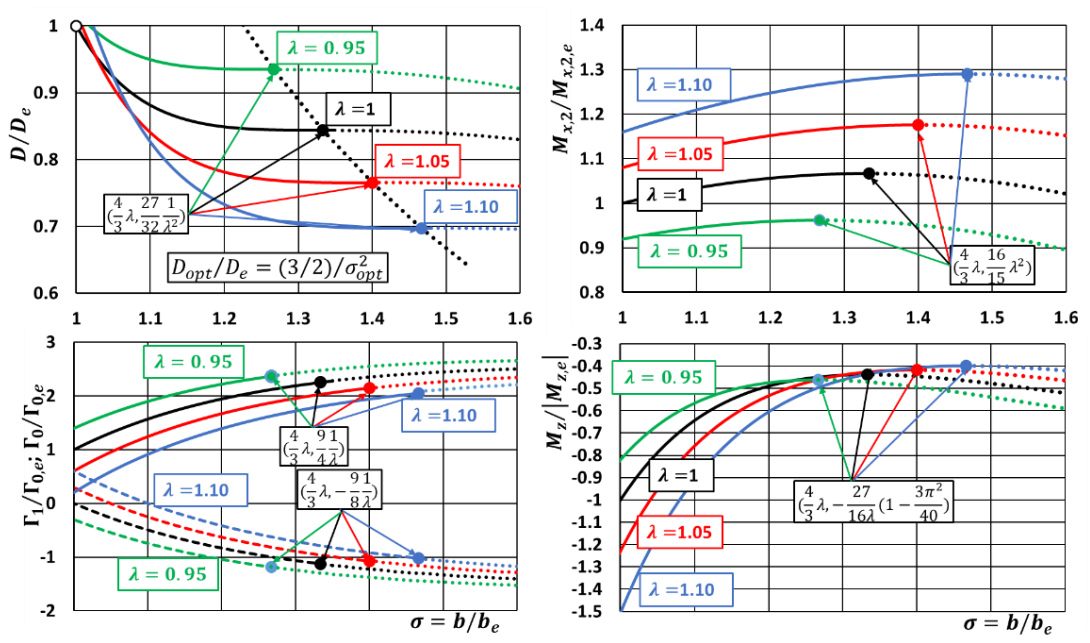


Figure 7 – Results of optimisation scenario (c): minimisation induced drag D, for prescribed free-stream conditions  $(U_{\infty},q_{\infty})$ , lift  $L=L_e$  and root-bending-moment  $M_x=\lambda M_{x,e}$ : yielding two-term circulation distribution  $\Gamma(\eta)=\Gamma_0\sqrt{1-\eta^2}+\Gamma_1\{\sqrt{1-\eta^2}+\eta^2\ln\frac{1+\sqrt{1-\eta^2}}{|\eta|}\}$ . Results are shown for  $\lambda=0.95(0.05)1.1$ , from green-to-black-to-red-to-blue coloured curves. Left-top: dimensionless induced drag  $D/D_e$  vs. dimensionless span  $\sigma\equiv b/b_e$ ; Left-bottom: amplitude two contributions circulation distribution  $\Gamma_0(\sigma)/\Gamma_{0,e}$  (solid lines) and  $\Gamma_1(\sigma)/\Gamma_{0,e}$  (dashed lines); Right-top: dimensionless starboard-integrated bending moment  $M_{x,2}/M_{x,2,e}$  vs.  $\sigma$  and; Right-bottom: dimensionless starboard-yawing-moment  $M_z/M_{z,e}$  vs.  $\sigma$ . Dotted lines: invalid solutions for which  $\Gamma(\eta)$  not positive for all  $|\eta|<1$ . Coloured round solid circles: optimum solution of minimum induced drag.

The optimal value of amplitude  $\Gamma_0/\Gamma_{0,e}$  of the bell-shaped distribution Eq. (17b) decreases slowly with increasing  $\lambda$  like  $9/4\lambda$ . This optimal value decreases slowly with  $\lambda$ , because the optimal span  $\sigma_{opt}=b_{opt}/b_e$  increases linearly with  $\lambda$ , in order to force the lift to remain equal to:  $L=L_e$ .

The optimal starboard-integrated bending-moment  $M_{x,2,opt}/M_{x,2,e}$  increases quadratically with increasing  $\lambda$ . For  $\lambda = M_{x,opt}/M_{x,e} = 1$ ,  $M_{x,2,opt}/M_{x,2,e}$  increases a mere 6.7%, for a wing with the optimal bell-shaped circulation distribution, which has an optimal span that is 33.3% longer than the wing with an elliptic circulation distribution. The induced drag for the optimal design equals  $D_{opt}/D_e = 0.84$ , 16% lower than the corresponding value of the elliptically-loaded wing.

For any value of  $\lambda$ , the starboard-yawing moment  $M_{z,opt}/|M_{z,e}|$  remains negative, at  $-\frac{27}{16\lambda}\Big(1-\frac{3}{40}\pi^2\Big)\approx -0.4384$  at  $\lambda=1$  and -0.3985 at  $\lambda=1.1$  a reduction by 56% and 60%, respectively, in magnitude compared to the wing with elliptic circulation distribution. The reason for this is that in the wing-tip region the section drag becomes negative (thrust rather than drag), which gives a positive (proverse) contribution to the yawing moment. This is advantageous for turning flight, since this leads to a smaller vertical tail surface, or even elimination of the vertical tail. Note that the optimisation scenario (b), minimizing induced drag for prescribed lift and starboard-span-integrated section-bending-moment, that resulted in the bell-shaped circulation distribution  $(1-\eta^2)^{3/2}$ , featured a starboard-yawing moment, for  $\tau=1$ , equal to  $M_{z,opt}/|M_{z,e}|\approx -0.5599$ , i.e.,10% less favourably in terms of amplitude.

Figure 8 presents results for three values of  $\lambda = M_x/M_{x,e}$ :  $\lambda = 1.0$ , 1.05 and 1.1, values in the same range as the ones used in Figure 7. Furthermore, for the dimensionless wing span  $\sigma = b/b_e$ , we choose, for each value of  $\lambda$ , the value for which the induced drag is minimal:  $\sigma_{opt} = b_{opt}/b_e = (4/3)\lambda$ . This implies that the corresponding circulation distributions satisfy  $\Gamma_1 = -0.5\Gamma_0$ , corresponding to bell-

shaped distributions  $\Gamma_{opt}(\eta) = \frac{1}{2}\Gamma_0[\sqrt{1-\eta^2}-\eta^2\ln\frac{1+\sqrt{1-\eta^2}}{|\eta|}]$ , with  $\frac{\Gamma_0}{\Gamma_{0,e}} = \frac{9}{4\lambda}$ . Results are compared with results for the elliptic circulation distribution  $\Gamma(\eta) = \Gamma_{0,e}\sqrt{1-\eta^2}$ . Figure 8 shows that with increasing  $\lambda = M_x/M_{x,e}$  the dimensionless section circulation  $\Gamma_{opt}(y/0.5b_e)/\Gamma_{0,e}$ , which is proportional to the dimensionless section lift:  $\ell(y/0.5b_e)/q_{\infty}b_e = 2\Gamma(y/0.5b_e)/q_{\infty}b_e$ , see Table 1, decreases near the wing root, which is due to the increase in dimensionless span  $\sigma = b_{opt}/b_e$  at constant total lift  $L_e$  distribution.

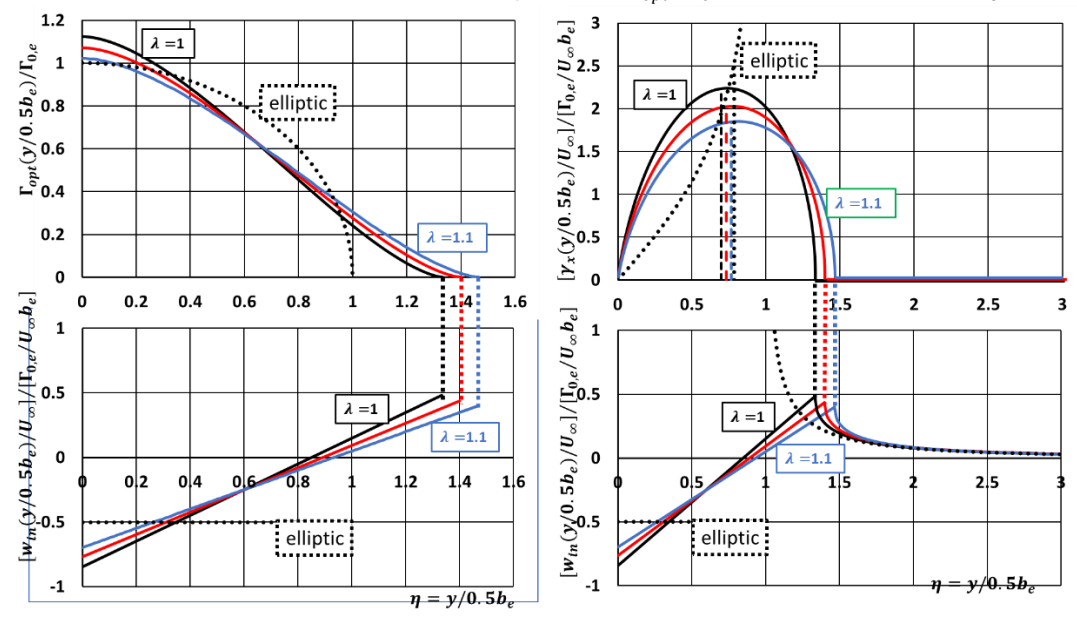


Figure 8 - Results optimisation scenario (c): minimisation of induced drag D, for prescribed free-stream conditions  $(U_{\infty},q_{\infty})$ , lift  $L=L_e$  and root-bending-moment  $M_x=\lambda M_{x,e}$ : yielding two-term circulation distribution  $\Gamma(\eta)=\Gamma_0\sqrt{1-\eta^2}+\Gamma_1\{\sqrt{1-\eta^2}+\eta^2\ln\frac{1+\sqrt{1-\eta^2}}{|\eta|}\}$ . Results are shown for  $\lambda=1.0(0.05)1.1$ , from black-to-red-to-blue coloured curves.  $\eta=(y/0.5b_e)/\sigma$ ; Minimum drag:  $\sigma=\sigma_{opt}=b_{opt}/b_e=(4/3)\lambda$ ,  $\Gamma_1=-0.5\Gamma_0$ . Top-left: spanwise distributions dimensionless circulation  $\Gamma_{opt}(y/0.5b_e)/\Gamma_{0,e}$  vs.  $y/0.5b_e$ ; Bottom-left: spanwise distributions dimensionless upwash velocity  $[w_{in}(y/0.5b_e)/U_{\infty}]/[\Gamma_{0,e}/U_{\infty}b_e]$  vs.  $y/0.5b_e$ ; Top-right: spanwise dimensionless vortex distribution  $[\gamma_x(y/0.5b_e)/U_{\infty}]/[\Gamma_{0,e}/U_{\infty}b_e]$  vs.  $y/0.5b_e$ ; Bottom-right: spanwise distributions dimensionless upwash velocity  $[w_{in}(y/0.5b_e)/U_{\infty}]/[\Gamma_{0,e}/U_{\infty}b_e]$  vs.  $y/0.5b_e$  on lifting line and its extension y>b/2. Vertical dashed lines: location COV. Results for elliptic circulation distribution: black dotted curves.

Figure 8 illustrates that the present bell-shaped distribution of the circulation gives a linear distribution of the upwash  $w_{in} (y/0.5b_e)/U_{\infty}$  along the lifting line, negative in the wing-root portion of the wing, positive in about 40-percent of the outboard part of the semi-span. The elliptic circulation distribution generates a constant (negative) upwash. As will be clear later on, this difference in upwash distribution has implications for the roll-up of the wake of the wing.

The vortex distribution along the lifting line decreases in peak value with increasing value of  $\lambda$ . The location of the peak, at  $y_{peak}/0.5b_e=0.55243(4/3)\lambda$ , as well as the location of the center-of-vorticity (COV) at  $y_{cov}/0.5b_e=(2\pi/9)\lambda < y_{peak}/0.5b_e$ , move outboard with increasing  $\lambda$ . For  $1.0663=3\pi/(16\times0.552434)<\lambda<9/8=1.125$ . the COV for the elliptic distribution, at  $y_{cov,e}/0.5b_e=\pi/4$ , is situated between  $y_{cov}/0.5b_e$  and  $y_{peak}/0.5b_e$ . For  $\lambda>9/8=1.125$ ,  $y_{cov,e}/0.5b_e< y_{cov}/0.5b_e$ , so inboard of both  $y_{cov}/0.5b_e$  and  $y_{peak}/0.5b_e$ .

Figure 8 also presents the upwash distribution for y > b/2, the outward extension of the lifting line. It shows that, characteristic for bell-shaped circulation distributions, the upwash distribution:

- (i) is continuous in function value across the wing tip;
- (ii) is slope-discontinuous across the wing tip: the slope is finite at the inboard side of the wing tip, but has a square-root singularity at the outboard side of the wing tip;
- (iii) tends to zero for points far outboard of the wing tip, as should be the case for any circulation distribution.

Figure 9 shows that for the elliptic distribution  $\Gamma_{0,e}\sqrt{1-\eta^2}$  of the circulation, the distribution of the section-drag  $d(y/0.5b_e)/q_\infty b_e$  of the wing is positive along the whole span of the wing, while for the bell-shaped circulation distribution  $\Gamma_{opt}(\eta) = \frac{1}{2}\Gamma_0[\sqrt{1-\eta^2}-\eta^2\ln{(1+\sqrt{1-\eta^2}/|\eta|)}]$ , with  $\Gamma_0/\Gamma_{0,e} = 9/(4\lambda)$ , the tip portion of the wing features much lower and even negative section-drag (section-thrust). In the

root portion of the wing, the bell-shaped circulation distribution generates a considerably higher section-drag, however, for the wing as a whole the net effect is a decrease in overall induced drag, like  $1/\lambda^2$ . It is also clear that increasing  $\lambda$  does not change the section-thrust in the tip region very much, while in the wing-root portion of the wing the section-drag decreases quite a bit. This is the reason that the overall induced drag decreases quadratically with increasing  $\lambda$ .

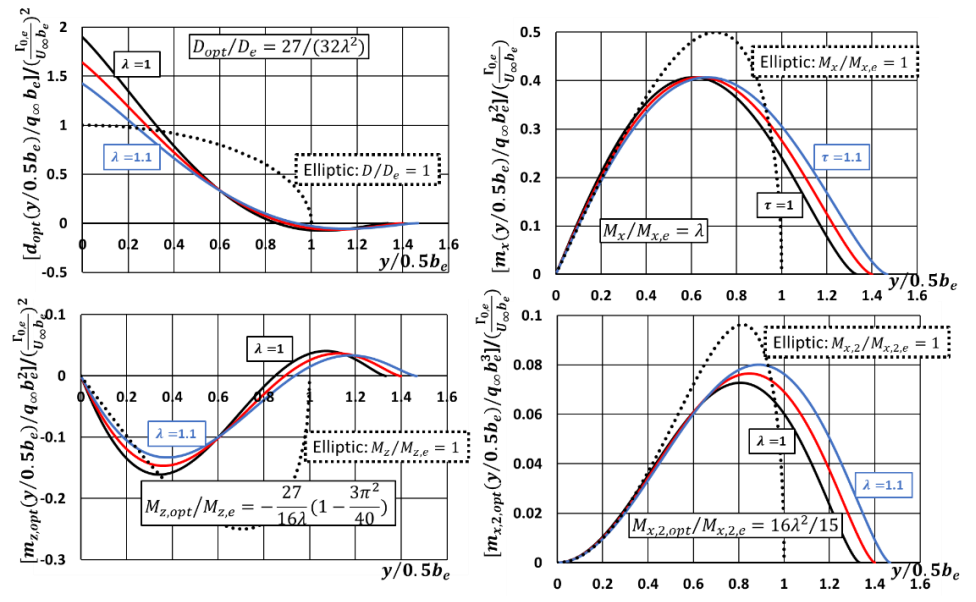


Figure 9 - Results optimisation scenario (c): minimisation of induced drag D, for prescribed free-stream conditions  $(U_{\infty},q_{\infty})$ , lift  $L=L_e$  and root-bending-moment  $M_x=\lambda M_{x,e}$ : yielding two-term circulation distribution  $\Gamma(\eta)=\Gamma_0\sqrt{1-\eta^2}+\Gamma_1\{\sqrt{1-\eta^2}+\eta^2\ln\frac{1+\sqrt{1-\eta^2}}{|\eta|}\}$ . Results are shown for  $\lambda=1.0(0.05)1.1$ , from black-to-red-to-blue coloured curves.  $\eta=(y/0.5b_e)/\sigma$ ;  $\sigma=\sigma_{opt}=b_{opt}/b_e=(4/3)\lambda$ ,  $\Gamma_1=-0.5\Gamma_0$ . Left-top: spanwise distributions dimensionless section drag  $[d_{opt}(y/0.5b_e)/q_{\infty}b_e]/(\Gamma_{0,e}/U_{\infty}b_e)^2$  vs.  $y/0.5b_e$ ; Left-bottom: spanwise distributions dimensionless section yawing moment  $[m_{z,opt}(y/0.5b_e)/q_{\infty}b_e^2]/(\Gamma_{0,e}/U_{\infty}b_e)^2$  vs.  $y/0.5b_e$ . Right-top: spanwise distributions dimensionless root-bending-moment  $[m_{x,opt}(y/0.5b_e)/q_{\infty}b_e^2]/(\Gamma_{0,e}/U_{\infty}b_e)$ . Results for elliptic circulation distribution: black dotted curves.

As far as the section contribution  $m_z(y/0.5b_e)/q_\infty b_e^2$  to the starboard-yawing moment  $M_z/q_\infty b_e^3$  is concerned, it is clear that for the bell-shaped distributions the yawing moment is much smaller in magnitude than that of the elliptic distribution of the circulation. For increasing  $\lambda = M_x/M_{x,e}$ , the yawing moment quite drastically decreases in magnitude, like  $1/\lambda$  because the contribution of the root portion of the wing, with negative, adverse, yawing moment, decreases.

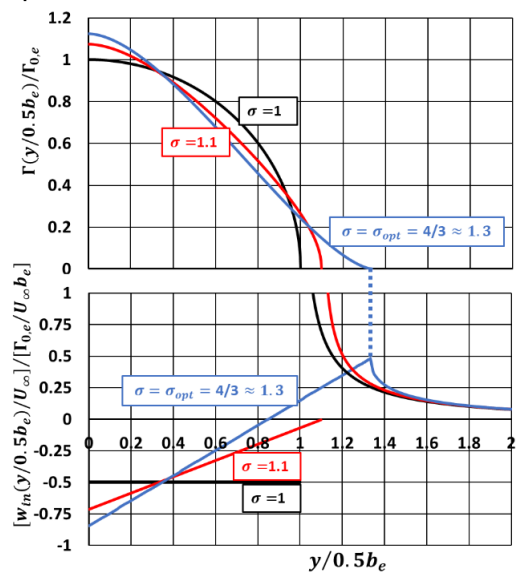
The plot of the distributions of the section contribution  $m_{\chi}(y/0.5b_e)$  to the root-bending-moment  $M_{\chi}$  indicates that the root-bending moment due to the bell-shaped distributions and that due to the elliptic circulation distribution differ in amplitude and in shaped. For  $\lambda = M_{\chi}/M_{\chi,e} = 1$ , the elliptic circulation distribution has the same  $M_{\chi}/M_{\chi,e} = 1$ , while the distribution  $m_{\chi}(y/0.5b_e)$  is quite different.

For  $\lambda=M_x/M_{x,e}>1$  the distribution  $m_x(y/0.5b_e)$  keeps about the same amplitude, which moves slowly in the direction of the wing tip, which itself moves outward, while the prescribed  $M_x/M_{x,e}$  increases linearly with  $\lambda$ . With increasing  $\lambda$  the distribution  $m_{x,2}(y/0.5b_e)$  of the section-contribution to the starboard-side integrated-bending-moment  $M_{x,2,opt}$  increases in amplitude, while simultaneously the distribution stretches in outboard direction because of the increasing span. This causes  $M_{x,2}$  to increase quadratically with increasing  $\lambda$ : for  $\lambda=1$ ,  $M_{x,2,opt}/M_{x,2,e}\approx 1.0667$ , for  $\lambda=1.1$ ,  $M_{x,2,opt}/M_{x,2,e}\approx 1.2907$  an increase by 21%.

Therefore, increasing  $\lambda = M_x/M_{x,e}$ , in optimisation scenario (c), results in a quadratic increase with  $\lambda$  in the integrated section-bending-moment  $M_{x,2}/M_{x,2,e}$ , while increasing the prescribed  $\tau = M_{x,2}/M_{x,2,e}$  in optimisation scenario (b) results in a modest square-root increase with  $\tau$  in the root-bending moment  $M_x/M_{x,e}$ . Note: Jones [17] Figure 5, presents a plot similar to Figure 6 (upper-left) above, though using a different notation for the parameter  $\lambda$  used in the present study. Furthermore, the specific condition at the wing tip, of a bell-shaped circulation distribution is not discussed.

Comparison with results of Drela [23]

In [23], the minimum-induced-drag problem is described in a form similar to that of scenario (c), though for more general configurations. The solution of the optimisation problem is obtained by numerically through a panel method which approximates the integral that provides the upwash  $w_{in}(y)$  as function of the vortex distribution  $\gamma_x(y)$ , i.e., the Biot-Savart law Eq. (1d). In effect the relation between upwash and vortex distribution is inverted numerically, rather than analytically as in Eq. (2a).



Drela [8		Present $\lambda = 1$	
$b/b_e$	$D/D_e$	$\sigma = b/b_e$	$D/D_e$
1.00	1.000	1	1.0
1.10	0.882	1.1	0.8811
1.30	0.845	1.3	0.8438
n.a	n.a	$\sigma_{opt} = 1.333$	0.8438

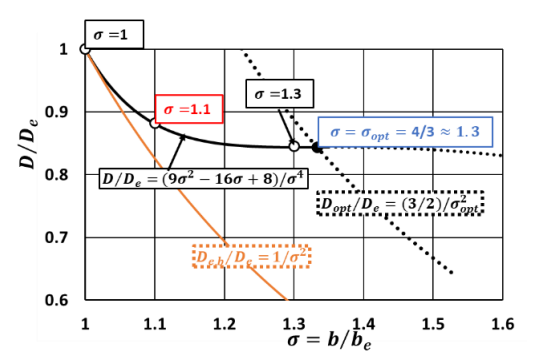


Figure 10 – Minimisation of induced drag D, for prescribed free-stream conditions  $(U_{\infty}, q_{\infty})$ , lift  $L = L_e$  and rootbending moment  $M_x = \lambda M_{x,e}$ , here  $\lambda = 1$ , yielding circulation distribution  $\Gamma(\eta) = \Gamma_0 \sqrt{1 - \eta^2} + \Gamma_1 \{\sqrt{1 - \eta^2} + \eta^2 \ln \frac{1 + \sqrt{1 - \eta^2}}{|\eta|} \}$ . Comparison present results with results obtained in [23]. Left-top: circulation distributions for 3 values of dimensionless span:  $\sigma = b/b_e = 1.0$ ,  $\sigma = 1.1$  and  $\sigma = \sigma_{opt} = 4/3$ . Left-bottom: distributions induced upwash for same dimensionless spans, for  $0 \le y/0.5b_e \le b/b_e$  and for  $y/0.5b_e \ge b/b_e$ . Right-bottom: Comparison induced drag  $D/D_e$  derived in present study with data (open circles) from [23].

In [23], the scaled induced drag  $D/D_e$  is given for three discrete values of the scaled span  $\sigma=b/b_e$ , see table in above Figure 10, with  $b_e$  the span of the wing carrying lift  $L=L_e$ , generated by the elliptic distribution of the circulation  $\Gamma(y)=\Gamma_{0,e}(1-\eta^2)^{1/2}$ , with  $\eta=y/0.5b$ . In the optimisation problem the lift is fixed at  $L_e$  and the root-bending-moment at  $M_x=M_{x,e}$ , i.e., in terms of the present formulation  $\lambda=1$ . The expressions in Table 6 are used to calculate, for  $\lambda=1$ , the value of the induced drag for the three discrete dimensionless wing spans  $\sigma=b/b_e$  used in [23], see table in Figure 10 above. Note, that the value  $\sigma=b/b_e=1.3$  is close to the optimal value of the span, which is equal to  $b/b_e=4/3=1.3333...$ 

Comparison of the circulation distributions obtained in the present study, presented in Figure 10, with the ones presented in [23] Figure 5.16, page 120, shows a very good correlation. The three distributions shown are the elliptic distribution  $\sigma=1$ , the distribution  $\sigma=1.3$  that is quite close to the bell-shaped distribution for  $\sigma=b/b_e=\sigma_{opt}=4/3$  and a distribution at an intermediate  $\sigma=1.1$ . At the wing tip, each of the three distributions has zero function value  $\Gamma(\sigma)=0$  and a square-root singularity  $d\Gamma/dy \to \infty$  for  $y/0.5b_e \uparrow \sigma$ . Only in case  $\sigma=b_{opt}/b_e=\sigma_{opt}$  the derivative and therewith the vortex distribution, equals zero at the wing tip.

Comparison of the distributions of the upwash, linear for 0 < y/0.5b < 1, obtained in the present study, presented in Figure 10, with the ones presented in [23], Figure 5.16, page 120, shows a very good correlation. In [23] the upwash distribution outboard of the wing tip has not been provided. Except the distribution for  $\sigma = b_{opt}/b_e = \sigma_{opt}$ , the upwash is discontinuous at the wing tip: finite for  $y/0.5b_e \uparrow \sigma$  and a square-root singularity for  $y/0.5b_e \downarrow \sigma$ . So, also for  $\sigma = 1.3$  the upwash distribution features this singularity.

Figure 10 presents the closed-form expression for induced drag  $D/D_e$  as function of  $\sigma=b/b_e$ , derived in the present study, in comparison with the numerical data given in [23], Figure 5.17, p. 120. The discrete data are in close agreement with the analytic results. Included in the plot for  $D(\sigma)/D_e$  is the envelope of the optimal (minimum) values of  $D_{opt}(\sigma)/D_e$ , proportional to  $1/\sigma_{opt}^2$ , with  $\sigma_{opt}=(4/3)\lambda$ , with here  $\lambda=1$ .

Also included in Figure 10 above, as well as in [23], in the plot  $D(\sigma)/D_e$  is the curve corresponding to the induced drag of the wing of span b and lift  $L_e$ , with elliptic circulation distribution. The induced drag of a wing of span  $b=b_e$ , with elliptic circulation distribution  $\Gamma(y)=\Gamma_{0,e}(1-\eta^2)^{1/2}$  has, according to Table 2, lift  $L=L_e=\frac{\pi}{2}(q_{\infty}/U_{\infty})b_e\Gamma_{0,e}$ , induced drag  $D_e=\frac{\pi}{4}(q_{\infty}/U_{\infty}^2)\Gamma_{0,e}^2$  and root-bending-moment  $M_{x,e}=rac{1}{6}(q_{\infty}/U_{\infty})b_e^2\Gamma_{0,e}$ . The wing with span b and elliptic circulation distribution  $\Gamma(y)=\Gamma_0(1-\eta^2)^{1/2}$  has lift  $L = \frac{\pi}{2} (q_{\infty}/U_{\infty}) b \Gamma_0$ , induced drag  $D = \frac{\pi}{4} (q_{\infty}/U_{\infty}^2) \Gamma_0^2$  and root-bending-moment  $M_x = \frac{1}{6} (q_{\infty}/U_{\infty}) b^2 \Gamma_0$ . Therefore, the amplitude  $\Gamma_0$  of the elliptic distribution on wing with span b and lift  $L_e^{\circ}$  equals  $\Gamma_0$  =  $(b_e/b)\Gamma_{0,e}$ , so that its induced drag equals  $D=\frac{\pi}{4}(q_\infty/U_\infty^2)\Gamma_{0,e}^2(b_e^2/b^2)=D_e(b_e^2/b^2)$ , see plot in Figure 10 above, and its root-bending-moment  $M_x=\frac{1}{6}(q_\infty/U_\infty)b_e^2\Gamma_{0,e}$   $(b/b_e)=M_{x,e}$   $(b/b_e)$ . The analysis shows that the induced drag of a wing with elliptic circulation distribution  $\Gamma(\eta) = \Gamma_0 \sqrt{1 - \eta^2}$  of fixed lift  $L_e$  and unconstrained root-bending-moment  $M_x$ , decreases quadratically with wing span, while its root-bendingmoment increases, unbounded, linearly with wing span. In contrast, the induced drag of a wing with circulation distribution  $\Gamma(\eta) = \Gamma_0 \sqrt{1 - \eta^2} + \Gamma_1 \{\sqrt{1 - \eta^2} + \eta^2 \ln \frac{1 + \sqrt{1 - \eta^2}}{|\eta|} \}$  of fixed lift  $L_e$  and constrained rootbending-moment  $\lambda M_{x,e}$ , decreases increasingly slower with increasing wing span, up to wing span  $\sigma = \sigma_{opt} = (4/3)\lambda$ : the wing span for which the circulation distribution is the bell-shaped distribution,  $\Gamma(\eta) = \frac{1}{2}\Gamma_0[\sqrt{1-\eta^2} - \eta^2 \ln \frac{1+\sqrt{1-\eta^2}}{|\eta|}]$ , with  $\Gamma_0 = 9/(4\lambda)$ . For wing spans beyond the optimal one, the present solution is invalid because the circulation distribution is not positive along its whole span. However, the present study does show that allowing a higher root-bending-moment than  $M_{x,e}$ , the one associated with the wing with elliptic circulation distribution ( $\lambda > 1$ ) constraint, translates into a lower

induced drag.

# 3.4 Minimization Induced Drag for prescribed Lift, prescribed Root-Bending Moment (Shear Force) in Combination with prescribed Span-integrated Section-Bending-Moment

For scenario (d), the optimisation is for constant lift L, for constant starboard-side root-bending moment  $M_x$  (equivalent to span-integrated section-shear-force  $F_z$ ) in combination with constant starboard-side span-integrated section-bending-moment  $M_{x,2}$ . In this case the variation  $\delta L$  of the lift L in combination with the variation  $\delta M_x$  of  $M_x$  and  $\delta M_{x,2}$  of  $M_{x,2}$ , due to the variation of  $\Gamma(y)$ , i.e., the optimisation comprises, see Appendix B:  $\delta D = -2\rho_{\infty} \int_{-b/2}^{b/2} w_{in}(y) \delta \Gamma(y) dy = 0, \text{ subject to } \\ \delta L = \rho_{\infty} U_{\infty} \int_{-b/2}^{b/2} \delta \Gamma(y) dy = 0, \\ \delta M_{x} = \rho_{\infty} U_{\infty} \int_{0}^{b/2} y \delta \Gamma(y) dy = 0 \text{ and.} \\ \delta M_{x,2} = \frac{1}{2} \rho_{\infty} U_{\infty} \int_{0}^{b/2} y^{2} \delta \Gamma(y) dy = 0.$ 

$$\delta D = -2\rho_{\infty} \int_{-b/2}^{b/2} w_{in}(y) \delta \Gamma(y) dy = 0, \text{ subject to}$$
 (5)

$$\delta L = \rho_{\infty} U_{\infty} \int_{-b/2}^{b/2} \delta \Gamma(y) dy = 0, \tag{18a}$$

$$\delta M_x = \rho_\infty U_\infty \int_0^{b/2} y \delta \Gamma(y) dy = 0 \text{ and.}$$
 (18b)

$$\delta M_{x,2} = \frac{1}{2} \rho_{\infty} U_{\infty} \int_0^{b/2} y^2 \delta \Gamma(y) dy = 0.$$
 (18c)

To force  $\delta D=0$  in Eq. (5), for arbitrary  $\delta \Gamma(y)$  obeying Eqs. (18a-c), it is to be prescribed that:

$$w_{in}(y) = U_{\infty}[A + B\frac{b}{2}|\eta| + C\eta^2], \text{ for } |y| < b/2.$$
 (18d)

From the analysis carried out for the preceding three optimisation scenarios, it follows that the distribution of the section-circulation  $\Gamma(\eta)$  will be equal to

Thoution of the section-circulation 
$$\Gamma(\eta)$$
 will be equal to 
$$\Gamma(\eta) = \Gamma_0 \sqrt{1 - \eta^2} + \Gamma_1 \left( \sqrt{1 - \eta^2} + \eta^2 \ln \frac{1 + \sqrt{1 - \eta^2}}{|\eta|} \right) + \Gamma_2 (1 - \eta^2)^{3/2},$$
 while, in this notation, the distribution of the upwash equals 
$$\frac{w_{in}(|\eta|<1)}{U_\infty} = -\frac{1}{2U_\infty b} \left[ \Gamma_0 + \Gamma_1 \pi |\eta| + 3\Gamma_2 (\frac{1}{2} - \eta^2) \right], \text{ for } |\eta| < 1.$$
 (19b) Furthermore, it follows that

$$\frac{v_{ln}(|\eta|<1)}{U_{lm}} = -\frac{1}{2U_{lm}h} \left[\Gamma_0 + \Gamma_1 \pi |\eta| + 3\Gamma_2 (\frac{1}{2} - \eta^2)\right], \text{ for } |\eta| < 1.$$
(19b)

$$\gamma_{x}(\eta) = \frac{2}{b} \left[ \Gamma_{0} \frac{\eta}{\sqrt{1-\eta^{2}}} + 2\Gamma_{1} \left( \frac{\eta}{\sqrt{1-\eta^{2}}} - \eta \ln \frac{1+\sqrt{1-\eta^{2}}}{|\eta|} \right) + 3\Gamma_{2} \eta \sqrt{1-\eta^{2}} \right]. \tag{19c}$$

In terms of the expression for the circulation distribution  $\Gamma(\eta)$ , the lift L, the starboard root-bending moment  $M_x$  (equal to the starboard span-integrated section-shear-force  $F_z$ ), the starboard span-integrated section-bending-moment  $M_{x,2}$  and the induced drag D, have been listed in Table 7.

Following Klein and Viswanathan ([19], [24]), the prescribed lift  $L = L_e$  is expressed in terms of the lift  $L_e$  generated by an elliptic distribution of the circulation at the same free-stream conditions of a wing with given span  $b_e$ . The amplitude  $\Gamma_{0,e}$  of the distribution of this imaginary wing is  $\Gamma(\eta) = \Gamma_{0,e} \sqrt{1 - \eta^2}$ . Using the expression for the lift of such a distribution, found in Table 2, i.e.,  $\frac{L_e}{q_{\infty}b_e^2} = \frac{\pi}{2} \frac{\Gamma_{0,e}}{U_{\infty}b_e}$ , defines  $\Gamma_{0,e}$ .

The prescribed root-bending-moment  $M_x$  is expressed as a factor  $\lambda$  times the root-bending moment  $M_{x,e}$  of the elliptic distribution as  $M_x = \lambda M_{x,e}$ , see Table 7:  $\frac{M_{x,e}}{q_{\infty}b_o^2} = \frac{1}{6} \frac{\Gamma_{0,e}}{U_{\infty}b_o}$ .

$\Gamma(\boldsymbol{\eta}) = \Gamma_0 \sqrt{1}$	$\frac{1-\eta^2}{1-\eta^2} + \Gamma_1 \left( \sqrt{1-\eta^2} + \eta^2 \ln \frac{1+\sqrt{1-\eta^2}}{ \eta } \right) + \Gamma_2 (1-\eta^2)^{3/2}$
$\frac{w_{in}( \eta <1)}{U_{\infty}}$	$\frac{-1}{2} \left[ \frac{\Gamma_0}{U_{\infty}b} + \frac{\Gamma_1}{U_{\infty}b} \pi  \eta  + \frac{\Gamma_2}{U_{\infty}b} 3(\frac{1}{2} - \eta^2) \right]$
$\frac{w_{in}( \eta >1)}{U_{\infty}}$	$\frac{-1}{2} \left[ \frac{\Gamma_0}{U_{\infty}b} \left( 1 - \frac{ \eta }{\sqrt{\eta^2 - 1}} \right) + \frac{2\Gamma_1}{U_{\infty}b} \left( \frac{- \eta }{\sqrt{\eta^2 - 1}} + \eta \arcsin(\frac{1}{\eta}) \right) + \frac{\Gamma_2}{U_{\infty}b} 3(\frac{1}{2} - \eta^2 +  \eta \sqrt{\eta^2 - 1}) \right]$
$\frac{L}{q_{\infty}b^2}$	$\frac{\pi}{2} \left[ \frac{\Gamma_0}{U_{\infty}b} + \frac{4}{3} \frac{\Gamma_1}{U_{\infty}b} + \frac{3}{4} \frac{\Gamma_2}{U_{\infty}b} \right]$
$\frac{\frac{L}{q_{\infty}b^2}}{\frac{D}{q_{\infty}b^2}}$	$\frac{\pi}{4} \left[ \left( \frac{\Gamma_0}{U_{\infty} b} \right)^2 + \frac{8}{3} \frac{\Gamma_0}{U_{\infty} b} \frac{\Gamma_1}{U_{\infty} b} + \frac{3}{2} \frac{\Gamma_0}{U_{\infty} b} \frac{\Gamma_2}{U_{\infty} b} + 2 \left( \frac{\Gamma_1}{U_{\infty} b} \right)^2 + \frac{8}{5} \frac{\Gamma_1}{U_{\infty} b} \frac{\Gamma_2}{U_{\infty} b} + \frac{3}{4} \left( \frac{\Gamma_2}{U_{\infty} b} \right)^2 \right]$
$\frac{M_{\chi}}{q_{\infty}b^3}$	$\frac{1}{6} \left[ \frac{\Gamma_0}{U_{\infty}b} + \frac{3}{2} \frac{\Gamma_1}{U_{\infty}b} + \frac{3}{5} \frac{\Gamma_2}{U_{\infty}b} \right]$
$\frac{M_x}{q_{\infty}b^3}$ $\frac{M_{x,2}}{q_{\infty}b^4}$ $\frac{M_z}{q_{\infty}b^3}$	$\frac{\pi}{128} \left[ \frac{\Gamma_0}{U_{\infty}b} + \frac{8}{5} \frac{\Gamma_1}{U_{\infty}b} + \frac{1}{2} \frac{\Gamma_2}{U_{\infty}b} \right]$
$\frac{M_z}{q_{\infty}b^3}$	$\frac{-1}{12} \left[ \left( \frac{\Gamma_0}{U_{\infty}b} \right)^2 + \frac{3}{2} \left( 1 + \frac{\pi^2}{8} \right) \frac{\Gamma_0}{U_{\infty}b} \frac{\Gamma_1}{U_{\infty}b} + \frac{9}{10} \frac{\Gamma_0}{U_{\infty}b} \frac{\Gamma_2}{U_{\infty}b} + \frac{3\pi^2}{10} \left( \frac{\Gamma_1}{U_{\infty}b} \right)^2 + \frac{1}{4} \left( 1 + \frac{3\pi^2}{8} \right) \frac{\Gamma_1}{U_{\infty}b} \frac{\Gamma_2}{U_{\infty}b} + \frac{27}{70} \left( \frac{\Gamma_2}{U_{\infty}b} \right)^2 \right]$
$y_{cov}/0.5b$	$\frac{\pi}{4} \left[ \Gamma_0 + \frac{4}{3} \Gamma_1 + \frac{3}{4} \Gamma_2 \right] / (\Gamma_0 + \Gamma_1 + \Gamma_2)$

Table 7 – Aerodynamic performance for scenario (d): minimisation of induced drag D, for prescribed free-stream conditions  $(U_{\infty},q_{\infty})$ , lift L, root-bending moment  $M_{x,2}$ , and span-integrated section-bending-moment  $M_{x,2}$ , yielding  $\text{circulation distribution } \Gamma(\eta) = \Gamma_0 \sqrt{1-\eta^2} + \Gamma_1 \left\{ \sqrt{1-\eta^2} + \eta^2 \ln \frac{1+\sqrt{1-\eta^2}}{|\eta|} \right\} + \Gamma_2 (1-\eta^2)^{3/2}.$ 

Similarly, the prescribed span-integrated section-bending-moment  $M_{x,2}$  is coupled to  $M_{x,2,e}$  of the elliptic distribution of circulation as  $M_{x,2} = \tau M_{x,2,e}$ , with, see Table 7:

$$\frac{M_{\chi,2,e}}{q_{\infty}b_e^4} = \frac{\pi}{128} \frac{\Gamma_{0,e}}{U_{\infty}b_e}.$$

Then a system of linear equations is constructed for the three parameters  $(\Gamma_0, \Gamma_1, \Gamma_2)$  in the expression,

Eq. (19a), for the circulation distribution, with, 
$$\hat{\Gamma}_{k} = \Gamma_{k}/\Gamma_{0,e}$$
 and  $\sigma = b/b_{e}$ :
$$\begin{pmatrix}
1 & 4/3 & 3/4 \\
1 & 3/2 & 3/5 \\
1 & 8/5 & 1/2
\end{pmatrix}
\begin{pmatrix}
\hat{\Gamma}_{0} \\
\hat{\Gamma}_{1} \\
\hat{\Gamma}_{2}
\end{pmatrix} = \begin{pmatrix}
1/\sigma \\
\lambda/\sigma^{2} \\
\tau/\sigma^{3}
\end{pmatrix}, \text{ so that } \begin{pmatrix}
\hat{\Gamma}_{0} \\
\hat{\Gamma}_{1} \\
\hat{\Gamma}_{2}
\end{pmatrix} = \begin{pmatrix}
126 & -320 & 195 \\
-60 & 150 & -90 \\
-60 & 160 & -100
\end{pmatrix}
\begin{pmatrix}
1/\sigma \\
\lambda/\sigma^{2} \\
\tau/\sigma^{3}
\end{pmatrix}. \tag{20a}$$

Substitution of Eq. (20a) in the expression for the induced drag  $\frac{D}{a_{\infty}b^2}$  in Table 7, divided by the induced drag  $\frac{D_e}{q_{\infty}b_e^2} = \frac{\pi}{4} \left(\frac{\Gamma_{0,e}}{U_{\infty}b_e}\right)^2$  of the wing with elliptic circulation distribution, yields, upon some algebra:  $\frac{D}{D_e} = \hat{\Gamma}_0^2 + \frac{8}{3} \hat{\Gamma}_0 \hat{\Gamma}_1 + \frac{3}{2} \hat{\Gamma}_0 \hat{\Gamma}_2 + 2\hat{\Gamma}_1^2 + \frac{8}{5} \hat{\Gamma}_1 \hat{\Gamma}_2 + \frac{3}{4} \hat{\Gamma}_2^2$ 

$$\frac{D}{D} = \hat{\Gamma}_0^2 + \frac{8}{3} \hat{\Gamma}_0 \hat{\Gamma}_1 + \frac{3}{2} \hat{\Gamma}_0 \hat{\Gamma}_2 + 2\hat{\Gamma}_1^2 + \frac{8}{5} \hat{\Gamma}_1 \hat{\Gamma}_2 + \frac{3}{4} \hat{\Gamma}_2^2$$
 (20b)

$$= \frac{4}{\sigma^6} \left[ 9\sigma^4 - 40\lambda\sigma^3 + (\frac{45}{2}\tau + 50\lambda^2)\sigma^2 - 60\lambda\tau\sigma + \frac{75}{4}\tau^2 \right]$$
 (20c)

The relation presented in Eq. (20c) is identical to the relation presented by Klein & Viswanathan ([19], 16]), as Eq. (19), when substituting  $\lambda = 1$  and  $\tau = 1$ .

Pate & German [30] considered Klein & Viswanathan's ([19], [24]) three-term circulation distribution for the case that the span-integrated section bending-moment and the root-bending-moment are parameters. In their notation  $\varepsilon_{\rm IBM} \equiv C_{\rm IBM}/C_{\rm IBM}|_{elliptic}$  and  $\varepsilon_{\rm RBM} \equiv C_{\rm RBM}/C_{\rm RBM}|_{elliptic}$  denote  $\tau$  and  $\lambda$ , respectively, in the notation of the present study. Note that in their study the span of the wing is fixed at the span of the wing with elliptic circulation distribution at the prescribed lift, i.e.,  $\sigma \equiv b/b_e = 1$ . Therefore, substituting Eq. (20c) for  $\sigma = 1$  in the so-called induced-drag parameter  $\delta$ , defined as  $\delta \equiv$  $D/D_e - 1$ , gives  $\delta = 5(7 - 32\lambda + 18\tau + 40\lambda^2 + 15\tau^2 - 48\lambda\tau)$ , which agrees with Eq. (16) in [30].

The choice of  $\sigma = 1$  in [30] implies that bell-shaped circulation distributions, with zero first derivative of the circulation distribution at the tip, do not show up in the analysis in [30].

To complete the optimisation, consider the first derivative of the induced drag, Eq. (20c), with respect to variable  $\sigma$ , with  $\lambda$  and  $\tau$  parameters:

$$\frac{d}{d\sigma} \frac{D}{D_e} = \frac{-2}{\sigma^7} [36\sigma^4 - 240\lambda\sigma^3 + (180\tau + 400\lambda^2)\sigma^2 - 600\lambda\tau\sigma + 225\tau^2],$$

which can be re-expressed as:

$$\frac{d}{d\sigma} \frac{D}{D_e} = -\frac{2}{\sigma^7} \left( 6\sigma^2 - 20\lambda\sigma + 15\tau \right)^2 = -\frac{72}{\sigma^7} \left[ \left( \sigma - \frac{5}{3}\lambda \right)^2 - \frac{5}{2} \left( \frac{10}{9}\lambda^2 - \tau \right) \right]^2 = 0.$$
 (20d)

The right-most expression in Eq. (20d) directly provides the two roots of  $\frac{d}{d\sigma} \frac{D}{D_o} = 0$ , i.e., the dimensionless wing span  $\sigma$  at which  $D/D_e$  is minimal:

$$\sigma_{opt,1,2} = \frac{5}{3}\lambda \pm \sqrt{\frac{5}{2}(\frac{10}{9}\lambda^2 - \tau)}, \text{ for } \tau \le \frac{10}{9}\lambda^2.$$
 (20e)

The condition  $\tau \leq \frac{10}{9}\lambda^2$  in Equation (20e) indicates the constraint on the choice of the value of  $\tau =$  $M_{x,2}/M_{x,2,e}$  in relation to the value of  $\lambda = M_x/M_{x,e}$ . The relation for the induced drag  $D/D_e$  in Eq. (20b) can also be expressed in a form similar to the one in Eq. (20e), after some algebra involving partial integration of Eq. (20d), it is found that:

$$\frac{D}{D_e} = \frac{4}{\sigma^6} \left[ 3 \left[ \left( \sigma - \frac{5}{3} \lambda \right)^2 - \frac{5}{2} \left( \frac{10}{9} \lambda^2 - \tau \right) \right]^2 + \frac{3}{5} \left[ \left( \sigma - \frac{5}{3} \lambda \right)^2 - \frac{5}{2} \left( \frac{10}{9} \lambda^2 - \tau \right) \right] \sigma \left( 7 \sigma - \frac{20}{3} \lambda \right) + \frac{9}{5} \sigma^2 \left[ \left( \sigma - \frac{5}{9} \lambda \right)^2 + \frac{5}{3} \left( \frac{25}{27} \lambda^2 - \tau \right) \right] \right]. \tag{20f}$$

The value of the relative span,  $\sigma_{opt,1,2} = b_{opt,1,2}/b_e$ , for which the first derivative of the induced drag with respect to dimensionless wing span  $\sigma = b/b_e$  equals zero, is the value for which the induced drag is at a local minimum. Substituting Eq. (20e) in Eq. (20f) yields:

$$\frac{D_{opt,1,2}}{D_e} = 12 \left[ \frac{\frac{5}{2} (\frac{4}{3}\lambda^2 - \tau) \pm \frac{4}{3}\lambda \sqrt{\frac{5}{2} (\frac{10}{9}\lambda^2 - \tau)}}{\left[ \frac{5}{3}\lambda \pm \sqrt{\frac{5}{2} (\frac{10}{9}\lambda^2 - \tau)} \right]^4} \right]. \tag{20g}$$

Furthermore, it follows from Eq. (19c) that the vortex distribution  $\gamma_x(\eta)$ , which is proportional to the first derivative of the circulation distribution  $\Gamma(\eta)$ , is zero at the wing tips if  $\hat{\Gamma}_0 + 2\hat{\Gamma}_1 = 0$  and singular otherwise. Substitution in Eq. (19a) then reveals, since  $\hat{\Gamma}_0 + 2\hat{\Gamma}_1 = 6\sigma^2 - 20\lambda\sigma + 15\tau$ , which is zero according to Eq. (20d), that for minimal induced drag at  $\sigma = \sigma_{opt,1,2}$ , the circulation distribution is a bell-shaped distribution: the one considered in section 3.3, but with the additional term  $\Gamma_2(1-\eta^2)^{3/2}$ :

$$\Gamma(\eta) = \frac{1}{2} \Gamma_0 \{ \sqrt{1 - \eta^2} - \eta^2 \ln \frac{1 + \sqrt{1 - \eta^2}}{|\eta|} \} + \Gamma_2 (1 - \eta^2)^{3/2}, \tag{20h}$$

at  $\sigma_{opt} = b_{opt}/b_e$ . This is the sum of the second and first bell-shaped distributions:  $\sqrt{1-\eta^2} - \eta^2 \ln \frac{1+\sqrt{1-\eta^2}}{|\eta|}$ and  $(1 - \eta^2)^{3/2}$ , respectively, found in the present study.

For  $\lambda=1$  and  $\tau=1$ , i.e., the case considered in [19], [24], the analytic expression Eq. (20e) gives  $\sigma_{opt,1} \approx 1.1396$  and  $\sigma_{opt,2} \approx 2.1936$ , for which Eq. (20g) gives  $D_{opt,1}/D_e \approx 0.9292$  and  $D_{opt,2}/D_e \approx 0.7959$ , respectively. Klein & Viswanathan's ([19], [24]) values for their first optimum ( $\sigma_{opt,1} \approx 1.160$  and  $(D_{opt,1}/D_e) \approx 0.929$ ) are slightly different, while the second optimum, at a much larger, probably nonfeasible, span, is not provided. As already clear from Eq. (20d), giving the first derivative of the induced drag, the second derivative of the induced drag

$$\begin{split} \frac{d^2}{d\sigma^2} \frac{D}{D_e} &= \frac{2}{\sigma^8} (6\sigma^2 - 20\lambda\sigma + 15\tau) (18\sigma^2 - 100\lambda\sigma + 105\tau) \\ &= \frac{216}{\sigma^8} [\left(\sigma - \frac{5}{3}\lambda\right)^2 - \frac{5}{2}\left(\frac{10}{9}\lambda^2 - \tau\right)] [\left(\sigma - \frac{25}{9}\lambda\right)^2 - \frac{35}{6}\left(\frac{250}{189}\lambda^2 - \tau\right)] \end{split} \tag{20i}$$
 is also zero at  $\sigma_{opt,1,2}$ . This reveals that both (local) minima in the induced drag are, again, at inflection

points of the curve  $D/D_e$  as function of  $\sigma = b/b_e$ .

From Eq. (20e) also surfaces that in case  $\sigma_{opt,1}=\sigma_{opt,2}=\frac{5}{3}\lambda$ , i.e., in case the two roots of  $\frac{d}{d\sigma}\frac{D}{D_c}=0$ coincide, the parameters  $\lambda$  and  $\tau$ , that govern the magnitude of the prescribed root-bending-moment  $M_x$  and the span-integrated section-bending-moment  $M_{x,2}$ , respectively, are related through  $\tau = \frac{10}{9} \lambda^2$ .

Eq. (20g) then yields: 
$$\frac{D_{opt,1,2}}{D_e} \Big|_{\tau = \frac{10}{\alpha} \lambda^2} = \frac{108}{125} \frac{1}{\lambda^2},$$
 (20j)

which, for  $\lambda = 1$  results in  $D_{opt,1}/D_e = D_{opt,2}/D_e = 0.8640$ , a value substantially lower than the 0.9292 for the case  $(\lambda, \tau) = (1,1)$  of Klein & Viswanathan ([19], [24]).

Further analysis gives that in the case of coinciding optimal values of  $\sigma_{opt}$ , the relation  $-2\hat{\Gamma}_1 + 3\hat{\Gamma}_2 =$ 0, equivalent to  $\hat{\Gamma}_0 + 3\hat{\Gamma}_2 = 0$ , is valid, which results, with  $\hat{\Gamma}_0 + 2\hat{\Gamma}_1 = 0$ , in the circulation distribution:

$$\Gamma(\eta) = \Gamma_0 \left[ \frac{1}{2} \left\{ \sqrt{1 - \eta^2} - \eta^2 \ln \frac{1 + \sqrt{1 - \eta^2}}{|\eta|} \right\} - \frac{1}{3} (1 - \eta^2)^{\frac{3}{2}} \right].$$
(20k)

At the wing tips this distribution features zero function value, zero first derivative and zero second derivative of the circulation distribution, i.e., the third bell-shaped distribution: a super-bell-shaped distribution. Table 8 summarizes the expressions derived so far in this section.

$\Gamma(\eta) = \Gamma_0 $	$\frac{1-\eta^2}{1-\eta^2} + \Gamma_1 \left( \sqrt{1-\eta^2} + \eta^2 \ln \frac{1+\sqrt{1-\eta^2}}{ \eta } \right) + \Gamma_2 (1-\eta^2)^{3/2}$
$\frac{w_{in}( \eta <1)}{U_{\infty}}$	$ \frac{-1}{2} \left[ \frac{\Gamma_0}{U_{\infty}b} + \frac{\Gamma_1}{U_{\infty}b} \pi  \eta  + \frac{\Gamma_2}{U_{\infty}b} 3(\frac{1}{2} - \eta^2) \right] $
$\frac{w_{in}( \eta >1)}{U_{\infty}}$	$\frac{-1}{2} \left[ \frac{\Gamma_0}{U_{\infty} b} \left( 1 - \frac{ \eta }{\sqrt{\eta^2 - 1}} \right) + \frac{2\Gamma_1}{U_{\infty} b} \left( \frac{- \eta }{\sqrt{\eta^2 - 1}} + \eta \arcsin(\frac{1}{\eta}) \right) + \frac{\Gamma_2}{U_{\infty} b} 3(\frac{1}{2} - \eta^2 +  \eta  \sqrt{\eta^2 - 1}) \right]$
$\frac{\Gamma_0}{\Gamma_{0,e}}$	$\frac{1}{\sigma^3}(126\sigma^2 - 320\lambda\sigma + 195\tau)$
$\frac{\Gamma_1}{\Gamma_{0,e}}$	$\frac{1}{\sigma^3}(-60\sigma^2 + 150\lambda\sigma - 90\tau)$
$\frac{\Gamma_2}{\Gamma_{0,e}}$	$\frac{1}{\sigma^3}(-60\sigma^2+160\lambda\sigma-100\tau)$
$ \begin{array}{c} L \\ L_e \\ \hline D \\ D_e \end{array} $	1
$\frac{D}{D_e}$	$\frac{4}{\sigma^6} [9\sigma^4 - 40\lambda\sigma^3 + \left(\frac{45}{2}\tau + 50\lambda^2\right)\sigma^2 - 60\lambda\tau\sigma + \frac{75}{4}\tau^2]$
$\frac{d}{d\sigma}\frac{D}{D_e}$	$-\frac{2}{\sigma^7}(6\sigma^2 - 20\lambda\sigma + 15\tau)^2 = -\frac{72}{\sigma^7}[\left(\sigma - \frac{5}{3}\lambda\right)^2 - \frac{5}{2}\left(\frac{10}{9}\lambda^2 - \tau\right)]^2$
$\frac{d^2}{d\sigma^2} \frac{D}{D_e}$	$\frac{216}{\sigma^8} \left[ \left( \sigma - \frac{5}{3} \lambda \right)^2 - \frac{5}{2} \left( \frac{10}{9} \lambda^2 - \tau \right) \right] \left[ \left( \sigma - \frac{25}{9} \lambda \right)^2 - \frac{35}{6} \left( \frac{250}{189} \lambda^2 - \tau \right) \right]$
$\frac{M_{\chi}}{M_{\chi,e}}$	λ
$\frac{M_{\chi,2}}{M_{\chi,2,e}}$	τ
$\frac{M_z}{ M_{z,e} }$	$-\frac{12}{7}\frac{1}{\sigma^5}[12\sigma^4 - 71\lambda\sigma^3 + 110(1 - \frac{21\pi^2}{352})\tau\sigma^2 + \frac{340}{3}\lambda^2\sigma^2 - \frac{1255}{4}(1 - \frac{105\pi^2}{2008})\lambda\tau\sigma + 150(1 - \frac{21\pi^2}{320})\tau^2]$
$\frac{y_{COV}}{0.5b_e}$	$\frac{\pi}{4} \frac{\sigma^3}{6\sigma^2 - 10\lambda\sigma + 5\tau}$
$\sigma_{opt} = rac{b_{opt}}{b_e}$	$\frac{5}{3}\lambda \pm \sqrt{\frac{5}{2}\left(\frac{10}{9}\lambda^2 - \tau\right)}$ , for $\tau \le \frac{10}{9}\lambda^2$
$\frac{D_{opt}}{D_e}$	$12\left[\frac{5}{2}\left(\frac{4}{3}\lambda^{2} - \tau\right) \pm \frac{4}{3}\lambda\sqrt{\frac{5}{2}\left(\frac{10}{9}\lambda^{2} - \tau\right)}\right] / \left[\frac{5}{3}\lambda \pm \sqrt{\frac{5}{2}\left(\frac{10}{9}\lambda^{2} - \tau\right)}\right]^{4}$
$\frac{y_{COV,opt}}{0.5b_e}$	$\frac{\pi}{40} \left[ \frac{5}{3} \lambda \pm \sqrt{\frac{5}{2} \left( \frac{10}{9} \lambda^2 - \tau \right)} \right]^2 / \left[ \left( \frac{5}{3} \lambda^2 - \tau \right) \pm \lambda \sqrt{\frac{5}{2} \left( \frac{10}{9} \lambda^2 - \tau \right)} \right]$

Table 8 – Summary solution scenario (d): minimisation of induced drag D, for prescribed free-stream conditions  $(U_{\infty},q_{\infty})$ , lift  $L=L_e$ , root-bending moment  $M_{\chi}=\lambda M_{\chi,e}$ , and span-integrated section-bending-moment  $M_{\chi,2}=\tau M_{\chi,2,e}$ , yielding circulation distribution  $\Gamma(\eta)=\Gamma_0\sqrt{1-\eta^2}+\Gamma_1\left\{\sqrt{1-\eta^2}+\eta^2\ln\frac{1+\sqrt{1-\eta^2}}{|\eta|}\right\}+\Gamma_2(1-\eta^2)^{3/2}$ .

Note: Optimal solution with +sign is invalid solution since resulting  $\Gamma(\eta)$  not positive over part of span.

Figure 11 presents results for the induced drag  $D/D_e$  and the distribution of the circulation  $\Gamma(y/0.5b_e)/\Gamma_e$  as function of the relative span  $\sigma=b/b_e$  and of the spanwise coordinate  $y/0.5b_e$ , respectively. Four cases are considered:

(i) The case of Klein & Viswanathan ([19], [24]), their Figure 1, i.e., for  $(\lambda, \tau) = (1,1)$ . The present result is the black curve in Figure 11. It shows that at  $\sigma = \sigma_{ont.1} = (10 - \sqrt{10})/6 \approx 1.14$ , the curve  $D(\sigma)/D_{\rho}$  features an inflection point (both first and second derivative with respect to  $\sigma$  are zero) at the point where  $D/D_e \approx 0.9292$ . Further down along the curve, the induced drag decreases to still lower values, until at  $\sigma = \sigma_{opt,2} = (10 + \sqrt{10})/6 \approx 2.1936$ , a second local minimum occurs, again an inflection point. However, beyond  $\sigma = \sigma_{opt,1}$  the section-circulation is negative along part of the span, which invalidates the solution. Furthermore, though for these values of  $\sigma = b/b_e$  the induced drag  $D/D_e \approx$ 0.7959 is substantially lower, the large span required to realise this result is not considered to be realistic. Figure 11 – right presents, as reference, the circulation distribution for the elliptic distribution (dotted line), which at the wing tip has a square-root singularity in the first derivative. The circulation distribution for  $(\lambda, \tau) = (1,1)$  plotted as black curve, illustrates the two local minimums: one for  $\sigma =$  $\sigma_{opt,1}$  (solid black curve) and one for  $\sigma=\sigma_{opt,2}$  (dashed black curve). In both cases, the distribution has zero function value and zero first derivative at the wing tip: giving a bell-shaped distribution. However, for  $\sigma = \sigma_{opt,2}$ , the distribution is negative in the region next to the wing tip. Actually, this is true for all cases with  $\sigma_{opt,1} < \sigma \le \sigma_{opt,2}$ , while for still larger spans the region with negative load moves inboard, away from the wing tip. For all such distributions, the integrals of moments of the load (proportional to  $\Gamma(\eta)$ ) should be taken as integrals of the absolute value of the load, not of the load itself, as has been done in the present study. This invalidates the present analysis for prescribed  $M_x$ and  $M_{x,2}$ , for  $\sigma > \sigma_{opt,1}$ .

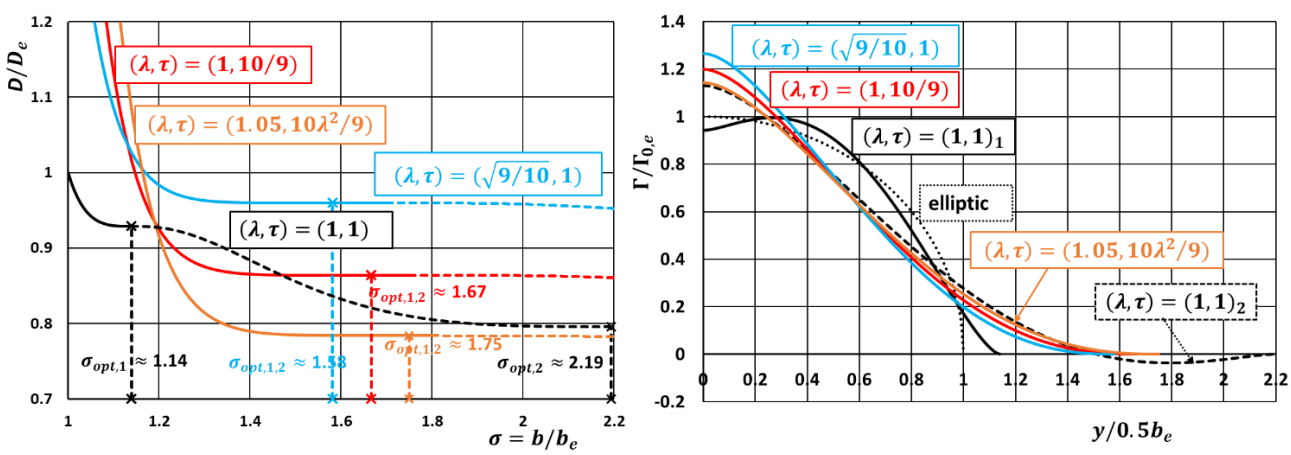


Figure 11 – Results optimisation scenario (d): minimisation of induced drag D, for prescribed free-stream conditions  $(U_{\infty},q_{\infty})$ , lift  $L=L_e$  and root-bending-moment  $M_{\chi}=\lambda M_{\chi,e}$  and span-integrated section-bending-moment  $M_{\chi,2}=\tau M_{\chi,2,e}$ , for 4 combinations of  $\lambda$  and  $\tau$ . Left: Induced drag  $D/D_e$  vs. span  $\sigma=b/b_e$ . Right: Distribution circulation  $\Gamma(y/0.5b_e)/\Gamma_{0,e}$ . Black line, present result Eq. (20c) for  $(\lambda=1,\tau=1)$ , identical to result of [19], [24]. Red line: Eq. (20c) for  $(\lambda=1,\tau=\frac{10}{9}\lambda^2)$  Bluish line: Eq. (20c) for  $(\lambda=(9\tau/10)^{1/2},\tau=1)$ . Ochre line: Eq. (20c) for  $(\lambda=1.05,\tau=10\lambda^2/9)$ . Dashed part of curves: invalid solution because  $\Gamma<0$  for part of span. Vertical dashed lines in the left plot indicate the location of optimal values of  $\sigma$  for minimal induced drag.

(ii) The new case  $(\lambda,\tau)=(\sqrt{9/10},1)$ , corresponding to the bluish curves in Figure 11. This is the first of three examples of cases for which  $\tau=(10/9)\lambda^2$ , i.e., the expression in Eq. (20e) implies that the roots of  $\frac{d}{d\sigma}\frac{D}{D_e}=0$ , Eq. (20d), features a zero discriminant. For such cases the two local minimums of  $D(\sigma)/D_e$  coincide, while, since also  $\frac{d^2}{d\sigma^2}\frac{D}{D_e}=0$  at this point, see Eq. (20i), the minimum is an inflection point as well. Actually, as can be deduced from Eq. (20i), since for  $\tau=\frac{10}{9}\lambda^2$ ,  $\sigma=\sigma_{opt,1}=\sigma_{opt,2}=\frac{5}{3}\lambda$ , the derivative of Eq. (20i) with respect to  $\sigma$ , i.e.,  $\frac{d^3}{d\sigma^3}\frac{D}{D_e}$ , is zero as well.

The present result is the bluish curve in Figure 11 - left. It shows that at  $\sigma = \sigma_{opt,1} = \sigma_{opt,2} = \frac{5}{3}\lambda \approx 1.5811$ , the curve indeed features a super-inflection point at which not only the first and second derivative of  $D(\sigma)/D_e$  with respect to  $\sigma$  are zero, but also the third derivative. The result is that in a relatively large range around  $\sigma = \sigma_{opt}$ ,  $D(\sigma)/D_e$  is about constant at  $\frac{108}{125}\frac{1}{\lambda^2} = \frac{120}{125} = 0.96$ , a modest value, in spite of the 58% increase in wing span with respect to the wing with the elliptic loading. The bell-shaped distribution of the circulation is included in Figure 11 – right, with at the wing tip, zero function value, zero first and zero second derivative with respect to the spanwise coordinate.

- (iii) The next case of a super-bell-shaped is  $(\lambda,\tau)=(1,10/9)$ , corresponding to the red curves in Figure 9. The optimal span is found to be  $\sigma_{opt}=\frac{5}{3}\lambda=5/3\approx 1.6667$ , somewhat longer than the one of case (ii). This longer span pays off in the optimum induced drag, which is now 10% lower than for case (ii), i.e.,  $D/D_e=\frac{108}{125}\approx 0.8640$  and lower than  $D/D_e$  for case (i), the case of Klein & Viswanathan ([19], [24]). But for the longer span, the distribution of the circulation is similar to the each of the three cases with  $\tau=(10/9)\lambda^2$ .
- (iv) The final case of super-bell-shaped distributions considered, is for a higher value of  $\lambda$ , namely  $\lambda$  = 1.05, which translates into a longer optimal span of  $\sigma_{opt} = \frac{5}{3}\lambda = 1.75$ . The results are indicated by the ochre-colored curves in Figure 11. The optimum induced drag achieved equals  $D/D_e = \frac{108}{125} \frac{1}{\lambda^2} \approx 0.7837$ , due to the longer span required for this wing to obey the prescribed constraints.

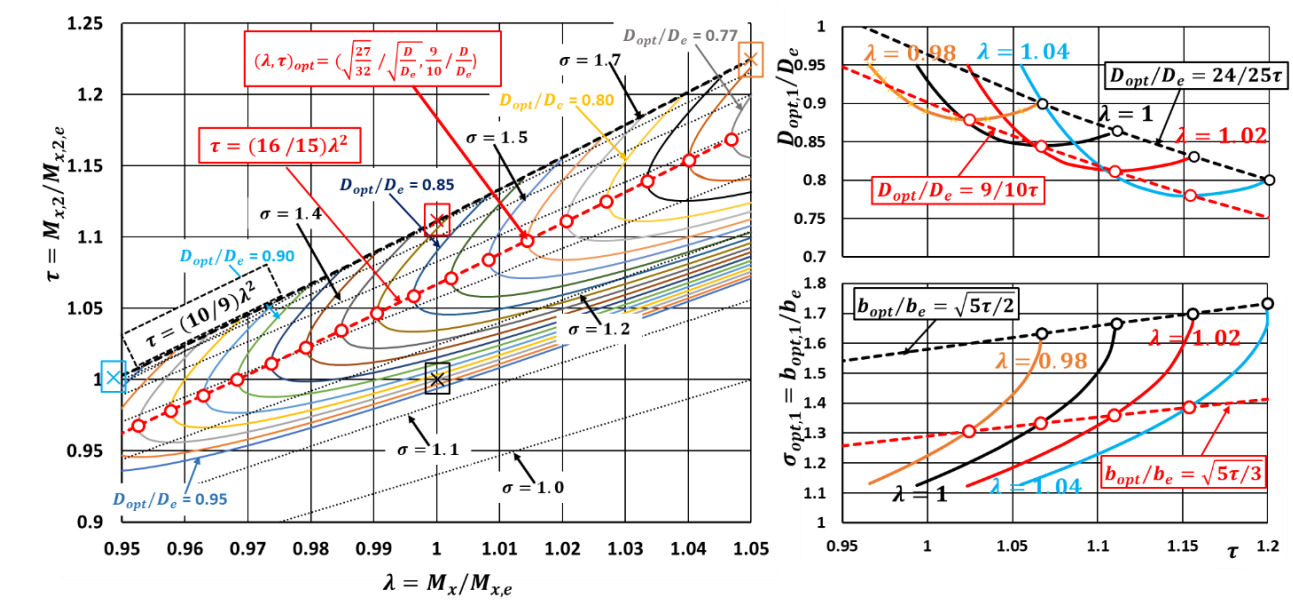


Figure 12 – Results for optimisation scenario (d): prescribed free-stream conditions  $(U_{\infty},q_{\infty})$ , lift  $L=L_e$ , rootbending moment  $M_{\chi}=\lambda M_{\chi,e}$  and span-integrated section-bending-moment  $M_{\chi,2}=\tau M_{\chi,2,e}$  in  $(\lambda,\tau)$ -plane. Left: Solid lines are iso-contours  $D_{opt,1}/D_e=0.77(0.01)0.95$  of optimal values of induced drag  $D_{opt,1}/D_e$  given in Eq. (20g). Dotted lines are iso-contours  $\sigma_{opt,1}=b_{opt,1}/b_e=1.0(0.1)1.7$ . Black dashed line is boundary of domain of validity  $\tau \leq \frac{10}{9}\lambda^2$ . The four crosses-inside-box symbols correspond to the four combinations  $(\lambda,\tau)$ -combinations discussed above. Red dashed line  $\tau = \frac{16}{15}\lambda^2$  with open circles representing ensemble of optimal  $(\lambda,\tau)$ -combinations. Right-upper: Vertical cross-sections  $\lambda = 0.98(0.02)1.04$ , of iso- $D_{opt,1}/D_e$  lines. Right-lower: Vertical cross-sections  $\lambda = 0.98(0.02)1.04$  of iso- $\sigma_{opt,1}$  lines. Black dashed lines with open circles are the ensemble of values of  $(D_{opt,1}/D_e)_{opt}$  and  $(\sigma_{opt,1})_{opt}$ .

To provide an overview of the present results, Figure 12-left presents iso-contours in the  $(\lambda,\tau)$ -plane, obtained from Eq. (20g), of the optimum-induced-drag  $D_{opt,1}/D_e$  and of the optimum span  $\sigma_{opt,1}=b_{opt,1}/b_e$  The induced drag has been minimised for prescribed lift  $L=L_e$ , prescribed root-bending moment  $\lambda=M_x/M_{x,e}$  and prescribed span-integrated section-bending-moment  $\tau=M_{x,2}/M_{x,2,e}$ . All results shown feature bell-shaped distributions of the circulation along the span of the wing. Figure 12-right presents vertical cross-sections of the results in Figure 12-left, which will help in the analysis and interpretation of the results. The herring-bone pattern of the  $D_{opt,1}/D_e$  iso-contours illustrates that in the  $(\lambda,\tau)$ -plane, there is a band-like, valley-type, region of steadily decreasing values of the induced drag. The envelope of the points at the bottom of the valley are found by taking the derivative of  $D/D_e$  with respect to  $\tau$  at  $\sigma=\sigma_{opt}$ . With Eq. (20c):

$$\frac{d}{d\tau}\frac{D}{D_e} = \left[\frac{d}{d\sigma}\frac{D}{D_e}\right]\frac{\partial\sigma}{\partial\tau} + \frac{\partial}{\partial\tau}\frac{D}{D_e} = \frac{\partial}{\partial\tau}\frac{D}{D_e} \text{ since at } \sigma = \sigma_{opt} = \frac{5}{3}\lambda - \sqrt{\frac{5}{2}\left(\frac{10}{9}\lambda^2 - \tau\right)}, \text{ Eq. (20d) gives } \frac{d}{d\sigma}\frac{D}{D_e} = 0.$$
Therefore, 
$$\frac{\partial}{\partial\tau}\frac{D}{D_e} = \frac{4}{\sigma^6}\frac{45}{2}\left[\sigma^2 - \frac{8}{3}\lambda\sigma + \frac{5}{3}\tau\right] = 0, \text{ leading to } \sigma = \frac{4}{3}\lambda \pm \frac{1}{2}\sqrt{\frac{20}{3}\left(\frac{16}{15}\lambda^2 - \tau\right)}.$$
Then it follows that along the bottom of the valley: 
$$\tau = \frac{16}{15}\lambda^2, \text{ while } \sigma_{opt} = \frac{4}{3}\lambda. \tag{20l}$$

In geographically terms, the valley runs from south-west to north-east, with the optimum induced drag decreasing from south-west to north-east along the bottom of the valley  $\tau=(16/15)\lambda^2$ . The iso-contours can be interpreted as altitude lines running clockwise along the flanks of the valley. On the steep, southerly side of the valley the contours are closely packed lines, running in negative  $\lambda$ -direction, from east to south. Then the iso-contours turn north, in positive  $\tau$ -direction. Subsequently the iso-contours cross the valley and turn in positive  $\lambda$ -direction, in north-easterly direction, along the less-steep northerly side of the valley. Finally, the iso-contours abruptly end at the dashed-black curve  $\tau=(10/9)\lambda^2$ . At this "barrier" the discriminant of Eq. (20e) equals zero, becoming negative north of this curve. At all points on the "barrier"  $\tau=(10/9)\lambda^2$ , i.e., the distribution of the circulation is of the super-bell-shaped type, given in Eq. (20k), at all other points in the  $(\lambda,\tau)$ -plane, south of the "barrier", the distribution of the circulation is of the bell-shaped type, given in Eq. (20h).

Within the chosen ranges  $0.95 < \lambda = M_x/M_{x,e} < 1.05$  and  $0.9 < \tau = M_{x,2}/M_{x,2,e} < 1.25$ , the induced drag has values between  $D_{opt,1}/D_e = 0.95$  at the left side of the plot and  $D_{opt,1}/D_e = 0.77$  at the right side of

the plot. So, it becomes clear that increasing  $\lambda$ , i.e., the root-bending-moment and increasing  $\tau$ , i.e., the span-integrated section-bending-moment, along the bottom  $\tau = (16/15)\lambda^2$  of the valley, leads to increasingly lower values of the induced drag. Klein & Viswanathan's ([19], [24]) analysis for just the single combination ( $\lambda = 1, \tau = 1$ ) turns out to be a case for which not much reduction in induced drag can be achieved:  $D_{opt,Klein\&Viswanthan}/D_e = 0.929$ . For example, increasing, for fixed  $\lambda = 1$ , the span-integrated section-bending-moment ( $\tau$ ) by 5% to  $\tau = 1.05$  reduces the induced drag to  $D_{opt,1}/D_e = 0.85$ . Simultaneously decreasing, at fixed  $\tau = 1$ , the root-bending-moment ( $\lambda$ ) by 2% to  $\lambda = 0.98$  would reduce the induced drag to  $D_{opt,1}/D_e = 0.89$ .

Included in the iso-contour plot are iso-contours (dotted black lines running in north-easterly direction) of the span  $\sigma_{opt} = b_{opt}/b_e$  required for achieve the optimum values of the induced drag. This reveals that in the valley of lowest values of the induced drag  $D_{opt}/D_e$ , the span of the wing is in between the reasonable values  $b_{opt}/b_e = 1.3$  and  $b_{opt}/b_e = 1.5$ .

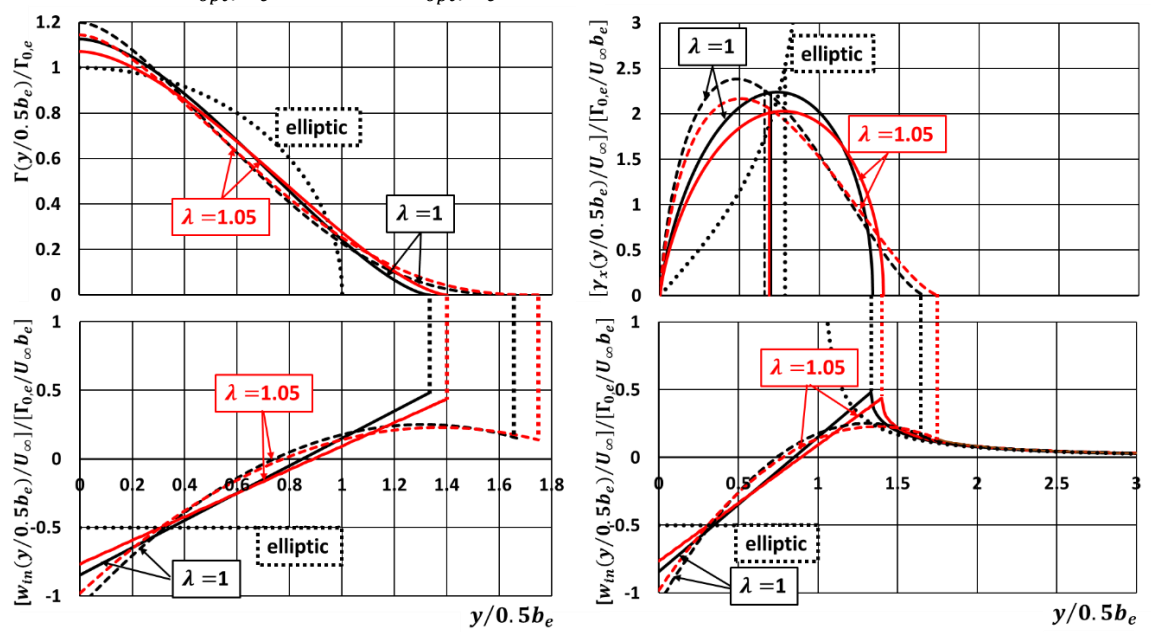


Figure 13 – Results for scenario (d): prescribed free-stream conditions  $(U_{\infty},q_{\infty})$ , lift  $L=L_e$ , root-bending moment  $M_x=\lambda M_{x,e}$  and span-integrated section-bending-moment  $M_{x,2}=\tau M_{x,2,e}$ . Left-upper: Circulation distribution  $\Gamma(y/0.5b_e)$ ; Right-upper: vortex distribution  $\gamma_x(y/0.5b_e)$ ; Left-lower: distribution upwash  $w_{in}(y/0.5b_e)$  for 0< y/0.5b<1; Right-lower: distribution upwash  $w_{in}(y/0.5b_e)$  for  $0< y/0.5b<3/\sigma$ . Solid black and red curves: "bottom valley"  $\tau=(16/15)\lambda^2$ ; Dashed black and red lines: "barrier"  $\tau=(10/9)\lambda^2$ . Solid-black line  $(\lambda,\tau)=(1,(16/15)\lambda^2)$ ; Dashed-black line  $(\lambda,\tau)=(1,(10/9)\lambda^2)$ ; Solid-red line  $(\lambda,\tau)=(1.05,(16/15)\lambda^2)$ ; dashed-red line  $(\lambda,\tau)=(1.04,(10/9)\lambda^2)$ ; dotted-black line: elliptic distribution circulation and wake vortex distribution.

Figure 13 presents detailed results of four  $(\lambda,\tau)$  combinations, selected from Figure 12: two (solid lines) combinations on the "optimum-optimorum" curve ("bottom valley")  $\tau=(16/15)\lambda^2$  and two (dashed-line) combinations on the "barrier" curve  $\tau=(10/9)\lambda^2$ , each pair for  $\lambda=1$  (black) and  $\lambda=1.05$  (red). Eqs. (20g) and (20e) show that along the "optimum-optimorum" curve  $\tau=(16/15)\lambda^2$  the induced drag equals  $D_{opt}/D_e=(27/32)\lambda^{-2}$ , while the wing span equals  $\sigma_{opt}=b_{opt}/b_e=(4/3)\lambda$ . Similarly, along the "barrier"-curve  $\tau=(10/9)\lambda^2$ , the induced drag is somewhat (factor 1.024) higher, equal to  $D_{opt}/D_e=(108/125)\lambda^{-2}$ , even though the wing span is substantially longer (factor 1.25), equal to  $\sigma_{opt}=b_{opt}/b_e=(5/3)\lambda$ , see Table 9.

The circulation distribution at points on the "optimum-optimorum"-curve does not include the  $(1-\eta^2)^{3/2}$ -term, just the first two terms, see Table 9. This solution is equivalent to the solution for scenario (c) investigated in section 3.3: a bell-shaped distribution. with at the wing tips zero function value and zero first derivative. The circulation distribution at points on the "barrier" curve in the  $(\lambda, \tau)$ -plane is also a bell-shaped distribution. This distribution includes all three terms, such that at the wing tips the function value, the first <u>and</u> the second derivatives of the circulation distribution are equal to zero. This is accompanied by, compared to the "optimum-optimorum" case, a longer span, which is lightly loaded in the tip region in combination with higher loads (section circulation) in the wing-root region.

	$\Gamma(\eta) = \Gamma_0 \sqrt{1 - \eta^2} + \Gamma_1 \left( \sqrt{1 - \eta^2} + \eta^2 \ln \frac{1 + \sqrt{1 - \eta^2}}{ \eta } \right) + \Gamma_2 (1 - \eta^2)^{3/2}$			
	"Optimum-optimorum"	"Barrier"		
$\Gamma(\eta)$	$\frac{\Gamma_0}{\Gamma_{0,e}} = \frac{9}{4\lambda}; \Gamma_1 = -\frac{1}{2}\Gamma_0; \Gamma_2 = 0$	$\frac{\Gamma_0}{\Gamma_{0,e}} = \frac{36}{25\lambda}; \Gamma_1 = -\frac{1}{2}\Gamma_0; \Gamma_2 = -\frac{1}{3}\Gamma_0$		
$ au_{opt}$	$\frac{16}{15}\lambda^2$	$\frac{10}{9}\lambda^2$		
$\sigma_{opt} = b_{opt}/b_e$	$\frac{4}{3}\lambda$	$\frac{5}{3}\lambda$		
$L/L_e$	1	1		
$D_{opt}/D_e$	$\frac{27}{32}\frac{1}{\lambda^2}$	$\frac{108}{125} \frac{1}{\lambda^2}$		
$M_{x,opt}/M_{x,e}$	λ	λ		
$M_{x,2,opt}/M_{x,2,e}$	$\tau = \frac{16}{15}\lambda^2$	$\tau = \frac{10}{9}\lambda^2$		
$M_{z,opt}/ M_{z,e} $	$-\frac{27}{16}(1-\frac{3}{40}\pi^2)\frac{1}{\lambda}$	$-\frac{522}{175}(1-\frac{21}{232}\pi^2)\frac{1}{\lambda}$		
$y_{COV,opt}/0.5b_e$	$\frac{\pi}{6}\sigma_{opt} = \frac{\pi}{4}\frac{8}{9}\lambda$	$\frac{\pi}{8}\sigma_{opt} = \frac{\pi}{4} \frac{5}{6}\lambda$		

Table 9 – Summary characteristics solutions on "optimum-optimorum" curve and on "barrier" curve. Scenario (d): minimisation of induced drag D, for prescribed free-stream conditions  $(U_{\infty}, q_{\infty})$ , lift  $L = L_e$ , root-bendingmoment  $M_x = \lambda M_{x,e}$ , and span-integrated section-bending-moment  $M_{x,2} = \tau M_{x,2,e}$ , yielding circulation distribution  $\Gamma(\eta) = \Gamma_0 \sqrt{1-\eta^2} + \Gamma_1 \left\{ \sqrt{1-\eta^2} + \eta^2 \ln \frac{1+\sqrt{1-\eta^2}}{|\eta|} \right\} + \Gamma_2 (1-\eta^2)^{3/2}$ .

The wake-vortex distribution  $\gamma_x(y/0.5b_e)$ , proportional to  $-d\Gamma/dy$ , shows that the principal difference between the two types of bell-shaped distributions of the circulation is the behavior at the wing tip:

- (a) The "optimum-optimorum" vortex distribution has zero function value and infinite slope, which results in an upwash distribution that is continuous in function value but discontinuous in its slope, i.e. a finite slope inboard and a square-root singularity outboard.
- (b) The "barrier" vortex distribution has zero function value and zero slope at the wing tip, which results in an upwash distribution that is continuous in function value as well as in its slope, but discontinuous in higher derivatives.

The upwash  $w_{in}(y/0.5b_e)$  induced along the span of the wing by the optimum-optimorum" distribution is a linear distribution, negative in the wing-root region, positive in the tip region. At the wing tip the upwash distribution is continued slope-discontinuously outboard of the wing tip, see Figure 13. The upwash induced by the 3-term "barrier" circulation distribution is quadratic along the span of the wing, compared to the "optimum-optimorum" distribution, more negative in the wing-root region and less positive in the wing-tip region. At the wing tip, the upwash distribution is continued slope-continuously outboard of the wing tip. For both distributions, the upwash tends to zero in the far-field.

For the "optimum-optimorum" vortex distribution the COV is at  $y_{COV}/y_{COV,e} = 8\lambda/9$ , while for the "barrier" distribution the COV is more inboard at  $y_{COV}/y_{COV,e} = 5\lambda/6$ .

Figure 14 Left-top presents the distribution of the dimensionless section-induced-drag coefficient

$$\frac{d(\eta)}{q_{\infty}b_e} = \frac{\Gamma_{0,e}^2}{v_{\infty}^2b_e^2} \frac{b_e}{b} [\hat{\Gamma}_0 + \hat{\Gamma}_1\pi|\eta| + \hat{\Gamma}_2 3(\frac{1}{2} - \eta^2)] [\hat{\Gamma}_0\sqrt{1 - \eta^2} + \hat{\Gamma}_1 \Big\{\sqrt{1 - \eta^2} + \eta^2 \ln\frac{1 + \sqrt{1 - \eta^2}}{|\eta|} \Big\} + \hat{\Gamma}_2 (1 - \eta^2)^{\frac{3}{2}}], \qquad (20m)$$
 for the pair of points on the "optimum-optimorum" curve  $\tau = (16/15)\lambda^2$  and the pair of points on the "barrier" curve  $\tau = (10/9)\lambda^2$ . Figure 14 shows that for the elliptic distribution  $\Gamma_{0,e}\sqrt{1 - \eta^2}$  of the circulation the distribution of the section-drag  $d(y/0.5b_e)/q_{\infty}b_e$  of the wing is positive along the whole span of the wing. For the 2-term "optimum-optimorum" bell-shaped circulation distributions  $\Gamma_{opt}(\eta) = \frac{1}{2}\Gamma_0[\sqrt{1 - \eta^2} - \eta^2 \ln(1 + \sqrt{1 - \eta^2}/|\eta|)]$ , with  $\Gamma_0/\Gamma_{0,e} = 9/(4\lambda)$ , the tip portion of the wing features much lower and even negative section-drag (section-thrust). In the root portion of the wing, the 2-term bell-shaped circulation distribution generates a considerably higher section-drag, however, for the wing as a whole the net effect is a decrease in overall induced drag, like  $1/\lambda^2$ . It is also clear that increasing  $\lambda$  does not change the section-thrust in the tip region very much, while in the wing-root portion of the wing the section-drag decreases quite a bit. This is the reason that the overall drag decreases quadratically with increasing  $\lambda$ . For the 3-term "barrier" bell-shaped circulation distributions  $\Gamma_{opt}(\eta) = \frac{1}{2}\Gamma_0[\sqrt{1-\eta^2}-\eta^2\ln(1+\sqrt{1-\eta^2}/|\eta|)] - \frac{2}{3}(1-\eta^2)^{3/2}]$ , with  $\Gamma_0/\Gamma_{0,e} = 36/(25\lambda)$ , the tip portion of the wing features similar magnitudes of section-thrust as the 2-term optimum-optimorum" 2-term distribution. However, in the root-section of the wing the 3-term "barrier" distribution shows higher levels of section drag than the 2-term distribution, resulting in a higher overall induced drag  $108/(125\lambda^2)$  for 3-term vs.  $27/(32\lambda^2)$  for 2-term distribution, i.e., an increase in induced drag of  $2.4\%$ .

As far as the section contribution  $m_z(y/0.5b_e)/q_\infty b_e^2$  to the starboard-yawing moment  $M_z/q_\infty b_e^3$  is concerned, it is clear that for both bell-shaped distributions the yawing moment is much smaller in magnitude than that of the elliptic circulation distribution. For increasing  $\lambda = M_x/M_{x,e}$ , the yawing moment quite drastically decreases in magnitude, like  $1/\lambda$  because the contribution of the root portion of the wing, with negative, adverse, yawing moment, decreases. The 3-term, "barrier", circulation distribution, with its longer span  $\sigma = b/b_e$ , features, at equal  $= M_x/M_{x,e}$  a 27.5% lower magnitude of yawing moment than the 2-term optimum-optimorum" circulation distribution.

The plot of the distributions of the section contribution  $m_x(y/0.5b_e)$  to the root-bending-moment  $M_x$  indicates that the root-bending moment due to the bell-shaped distributions and that due to the elliptic circulation distribution differ in amplitude and in shape. For  $\lambda=M_x/M_{x,e}=1$ , the elliptic circulation distribution and the two bell-shaped distributions have identical  $M_x/M_{x,e}=1$ , while the distributions of  $m_x(y/0.5b_e)$  is quite different. For the bell-shaped distributions, the longer wing span and the wing-tip continuity conditions result in a shift of the outboard half of the distributions of  $m_x(y/0.5b_e)$ . The amplitude of the distribution  $m_x(y/0.5b_e)$  depends stronger on the type of bell-shaped distribution than on  $\lambda$ . With increasing  $\lambda$  the distribution  $m_{x,2}(y/0.5b_e)$  of the section-contribution to the starboard-side integrated-bending-moment  $M_{x,2,opt}$  increases in amplitude, while simultaneously the distribution stretches in outboard direction because of the increasing span. For the "optimum-optimorum" distribution this causes  $M_{x,2}$  to increase quadratically with increasing  $\lambda$ : for  $\lambda=1$ ,  $M_{x,2,opt}/M_{x,2,e}\approx 1.0667$ , for  $\lambda=1.05$ ,  $M_{x,2,opt}/M_{x,2,e}\approx 1.1760$  an increase by 10%.

Therefore increasing  $\lambda = M_x/M_{x,e}$ , in optimisation scenario (d), results in a quadratic increase with  $\lambda$  in the integrated section-bending-moment  $M_{x,2}/M_{x,2,e}$ , similar to scenario (c). Of course, choosing for a somewhat higher root-bending moment, of span-integrated section-bending-moment pays off in a considerable decrease in induced drag.

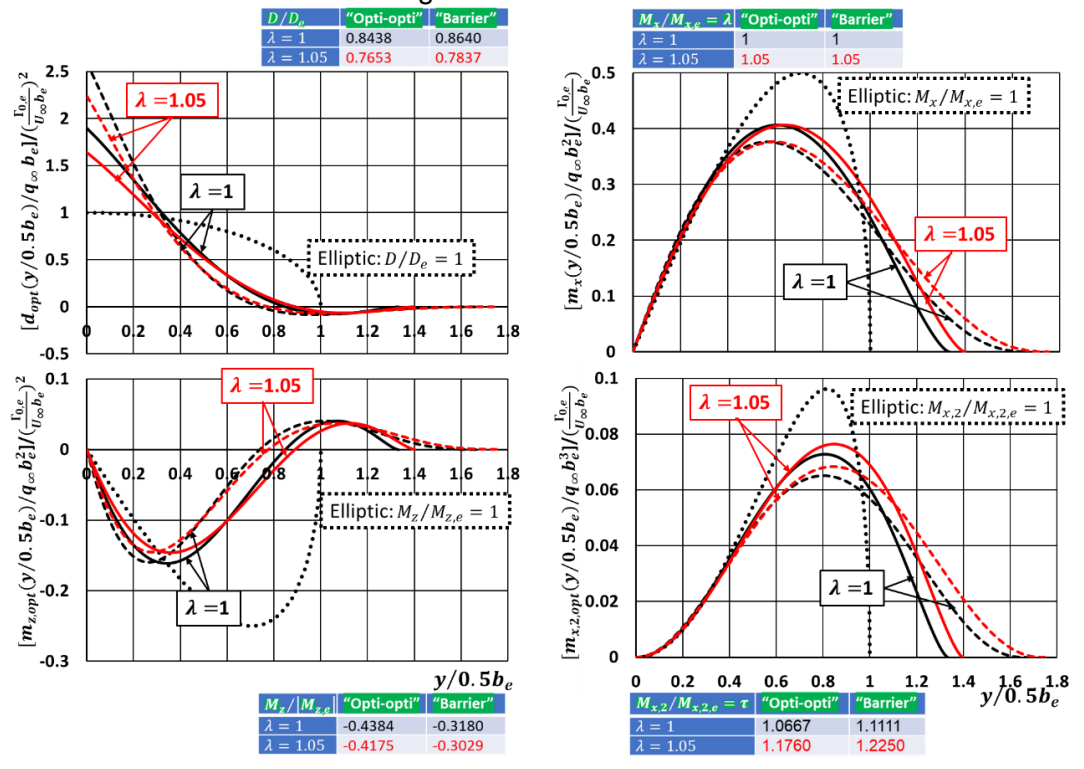


Figure 14 - Results optimisation scenario (d): minimisation of induced drag D, for prescribed free-stream conditions  $(U_{\infty},q_{\infty})$ , lift  $L=L_e$ , root-bending-moment  $M_x=\lambda M_{x,e}$  and span-integrated section-bending-moment  $M_{x,2}=\tau M_{x,2,e}$ . Solid black and red curves: "optimum-optimorum"  $\tau=(16/15)\lambda^2$ ; Dashed black and red lines: "barrier"  $\tau=(10/9)\lambda^2$ . Solid-black line  $(\lambda,\tau)=(1,(16/15)\lambda^2)$ ; Dashed-black line  $(\lambda,\tau)=(1,(10/9)\lambda^2)$ ; Solid-red line  $(\lambda,\tau)=(1.05,(16/15)\lambda^2)$ ; dashed-red line  $(\lambda,\tau)=(1.04,(10/9)\lambda^2)$ ; dotted-black line: results for elliptic distribution circulation. Left-top: spanwise distributions dimensionless section drag  $[d_{opt}(y/0.5b_e)/q_{\infty}b_e]/(\Gamma_{0,e}/U_{\infty}b_e)^2$  vs.  $y/0.5b_e$ ; Left-bottom: spanwise distributions dimensionless section yawing moment  $[m_{z,opt}(y/0.5b_e)/q_{\infty}b_e^2]/(\Gamma_{0,e}/U_{\infty}b_e)^2$  vs.  $y/0.5b_e$ . Right-top: spanwise distributions dimensionless root-bending-moment  $[m_{x,opt}(y/0.5b_e)/q_{\infty}b_e^2]/(\Gamma_{0,e}/U_{\infty}b_e)$ . Right-bottom: spanwise distributions dimensionless integrated-bending-moment  $[m_{x,opt}(y/0.5b_e)/q_{\infty}b_e^2]/(\Gamma_{0,e}/U_{\infty}b_e)$ . Sub-tables provide integrated: drag, starboard-yawing-moment, root-bending moment and span-integrated section-bending-moment, see Table 9.

Finding the distribution of the twist angle

In order to generate the circulation distribution that produces the prescribed lift  $L_e$ , root-bending-moment  $\lambda M_{x,e}$  and integrated section-bending-moment  $\tau M_{x,2,e}$  at minimum induced drag, the wing is required to possess twist. The distribution of the section chord c(y) is specified. The wing selected has a linear distribution of the chord:

$$c(\eta)/b_e = (c_r/b_e)(1-\eta) + (c_t/b_e)\eta$$
, with  $c_r/b_e = 0.16$  and  $c_t/b_e = 0.04$ . (20n)  
The geometric mean chord is equal to  $\bar{c}/b_e = [c_r/b_e + c_t/b_e]/2$ .

The spanwise distribution of the section  $\Delta\alpha$  follows from  $\Delta\alpha(y/0.5\,b_e) = \alpha - \alpha_0(y/0.5\,b_e) + \beta(y/0.5\,b_e)$ , with  $\alpha$  the wing angle-of-attack,  $\alpha_0(y)$  the section zero-lift angle and  $\beta$  the section twist angle. The section  $\Delta\alpha(y/0.5\,b_e)$  follows from Eq. (4b) as

$$\Delta\alpha(y) = \frac{2}{a_0} \frac{\Gamma_{0,e}}{U_{\infty}b_e} \frac{b_e}{c(y)} \frac{\Gamma(y)}{\Gamma_{0,e}} - \frac{w_{in}(y)}{U_{\infty}}$$

$$= \frac{2}{\pi} C_{L,e} \left[ \frac{2}{a_0} \frac{\bar{c}}{c(\eta)} \left\{ \hat{\Gamma}_0 \sqrt{1 - \eta^2} + \hat{\Gamma}_1 \left( \sqrt{1 - \eta^2} + \eta^2 \ln \frac{1 + \sqrt{1 - \eta^2}}{|\eta|} \right) + \hat{\Gamma}_2 (1 - \eta^2)^{3/2} \right\} + \frac{1}{2} \frac{\bar{c}}{b_e} \frac{b_e}{b} \left\{ \hat{\Gamma}_0 + \hat{\Gamma}_1 \pi |\eta| + \hat{\Gamma}_2 3 \left( \frac{1}{2} - \eta^2 \right) \right\} \right], (200)$$

with  $C_{L,e}=L_e/q_\infty b_e \bar{c}$ , the lift coefficient of the wing with the elliptic loading. Note that  $C_L=L/q_\infty b\bar{c}=C_{L,e}\,b_e/b=C_{L,e}/\sigma$ . Figure 15 shows the resulting distributions of  $\Delta\alpha(y/0.5\,b_e)$  for the "optimum-optimorum" distribution and for the "barrier" distribution. Included in Figure 15 is the result for the elliptic distribution of the circulation, obtained by substituting  $b=b_e$ ,  $\hat{\Gamma}_1=0$  and  $\hat{\Gamma}_2=0$  in Eq. (200). For the elliptic distribution the section-drag is positive all along the span of the wing, due to the induced (negative) upwash being constant along the entire span.

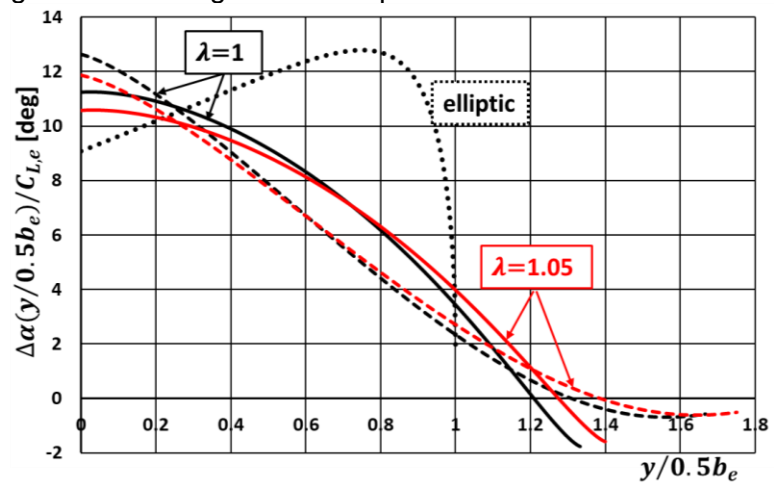


Figure 15 – Scenario (d): prescribed free-stream conditions  $(U_{\infty},q_{\infty})$ , lift  $L=L_e$ , root-bending moment  $M_{\chi}=\lambda M_{\chi,e}$  and span-integrated section-bending-moment  $M_{\chi,2}=\tau M_{\chi,2,e}$ . Chord  $c(\eta)$ : linear distribution, see Section 4. Distribution required section  $\Delta\alpha(y/0.5\,b_e)=\alpha-\alpha_0(y/0.5\,b_e)+\beta(y/0.5\,b_e)$ , with  $\alpha$  angle-of-attack,  $\alpha_0$  section zero-lift angle and  $\beta$  the section twist angle, for two points on "optimum-optimorum" curve  $\tau=(16/15)\lambda^2$  and two points on "barrier" curve  $\tau=(10/9)\lambda^2$ . Solid-black line  $(\lambda,\tau)=(1,(16/15)\lambda^2)$ ; dashed-black line  $(\lambda,\tau)=(1,(10/9)\lambda^2)$ ; solid-red line  $(\lambda,\tau)=(1.05,(10/9)\lambda^2)$ ; dotted-black line elliptic distribution.

Figure 15 illustrates that, in order to achieve the optimum distributions of the circulation, the distribution of  $\Delta\alpha(y/0.5\,b_e) = \alpha - \alpha_0(y/0.5\,b_e) + \beta(y/0.5\,b_e)$ , i.e., the distribution of the wing-twist angle  $\beta(y/0.5\,b_e)$ , is required to adjust considerably from a high value in the root region to a lower and even negative value in the tip region, with a wash-out of the twist angle in case of  $(\lambda,\tau)$ -values on the "barrier"-curve. The distribution of  $\Delta\alpha(y/0.5\,b_e)$  required to achieve the elliptic distribution of the circulation, given by

$$\Delta \alpha(y) = \frac{2}{\pi} C_{L,e} \left[ \frac{2}{a_0} \frac{\bar{c}}{c(y)} \sqrt{1 - \eta^2} + \frac{1}{2} \frac{\bar{c}}{b_e} \right], \tag{20p}$$

is of guite different from that required for the bell-shaped distributions of the circulation.

3.5 Comparison performance bell-shaped distributions circulation

Apart from the elliptic distribution 
$$\Gamma(\eta) = \Gamma_0 (1 - \eta^2)^{1/2}$$
, (21a)

associated with a constant (negative) upwash distribution 
$$\frac{w_{in}(|\eta|<1)}{U_{\infty}} = -\frac{1}{2} \frac{\Gamma_0}{U_{\infty}b}$$
, (21b)

considered in section 3.1, in the present study three bell-shaped distributions of the circulation have been discussed:

(1) 
$$\Gamma(\eta) = \Gamma_{22}(1 - \eta^2)^{3/2}$$
, also, as  $\Gamma(\eta) = \Gamma_2(1 - \eta^2)^{3/2}$ , (21c)

(1) 
$$\Gamma(\eta) = \Gamma_{22}(1 - \eta^2)^{3/2}$$
, also, as  $\Gamma(\eta) = \Gamma_2(1 - \eta^2)^{3/2}$ , associated with a quadratic upwash distribution  $\frac{w_{in}(|\eta|<1)}{U_{\infty}} = -\frac{1}{2}\frac{\Gamma_2}{U_{\infty}b}3(\frac{1}{2}-\eta^2)$ , (21d)

discussed in section 3.2 and also, section 3.3, respectively;

(2) 
$$\Gamma(\eta) = \frac{1}{2} \Gamma_0 [(1 - \eta^2)^{1/2} - \eta^2 \ln \{ (1 + (1 - \eta^2)^{1/2}) / |\eta| \} ],$$
 (21e)

associated with a linear upwash distribution 
$$\frac{w_{in}(|\eta| < 1)}{U_{\infty}} = -\frac{1}{2} \frac{\Gamma_0}{U_{\infty} b} (1 - \frac{\pi}{2} |\eta|),$$
 (21f) discussed in section 3.3 and section 3.4: and

discussed in section 3.3 and section 3.4; and

(3) 
$$\Gamma(\eta) = \frac{1}{2} \Gamma_0 \left[ (1 - \eta^2)^{1/2} - \eta^2 \ln \left\{ (1 + (1 - \eta^2)^{1/2}) / |\eta| \right\} - \frac{2}{3} (1 - \eta^2)^{3/2} \right],$$
 (21g) associated with a quadratic upwash distribution  $\frac{w_{in}(|\eta| < 1)}{U_{\infty}} = -\frac{1}{2} \frac{\Gamma_0}{U_{\infty b}} \left[ 1 - \frac{\pi}{2} |\eta| - 2 \left( \frac{1}{2} - \eta^2 \right) \right],$  (21h) discussed in section 3.4.

(4) In addition, here a fourth bell-shaped distribution is introduced:  $\Gamma(\eta) = \Gamma_3 (1 - \eta^2)^{5/2}$ , that satisfies the conditions at the wing tip of distribution (3), namely zero function value, zero first and zero second derivative. This distribution generates a quartic-polynomial upwash distri

$$\frac{w_{in}(|\eta|<1)}{U_{\infty}} = -\frac{1}{2} \frac{\Gamma_3}{U_{\infty,b}} 5 \left[\frac{3}{8} - \eta^2 \left(\frac{3}{2} - \eta^2\right)\right]. \tag{21j}$$

Table 10 collects the expressions for the performance of the four bell-shaped distributions and in addition, the "stretched" elliptic distribution for wings of span b. The parameter in these four expressions is the relative span  $\sigma = b/b_e$ .

	$\frac{\Gamma_0\sqrt{1-\eta^2}}{\text{(reference distribution)}}$	$\Gamma_2(1-\eta^2)^{3/2}$ , or $\Gamma_{2,2}(1-\eta^2)^{3/2}$	$ \frac{1}{2} \Gamma_0 [\sqrt{1 - \eta^2} - \eta^2 \ln(\frac{1 + \sqrt{1 - \eta^2}}{ \eta })] $	$ \frac{\frac{1}{2}\Gamma_0[\sqrt{1-\eta^2} - \frac{1}{\eta^2 \ln\left(\frac{1+\sqrt{1-\eta^2}}{ \eta }\right)} - \frac{\frac{2}{3}(1-\eta^2)^{3/2}] } $	$\Gamma_3(1-\eta^2)^{5/2}$ (additional bellshaped distribution)
$\frac{L}{L_e} = 1$	$\sigma \frac{\Gamma_0}{\Gamma_{0,e}} = 1$	$\frac{3}{4}\sigma\frac{\Gamma_2}{\Gamma_{0,e}}=1$	$\frac{1}{3}\sigma\frac{\Gamma_0}{\Gamma_{0,e}}=1$	$\frac{1}{12}\sigma\frac{\Gamma_0}{\Gamma_{0,e}}=1$	$\frac{5}{8}\sigma\frac{\Gamma_3}{\Gamma_{0,e}}=1$
$\frac{\frac{D_{opt}}{D_e}}{\frac{M_X}{M_X}} = \lambda$	$\left(\frac{\Gamma_0}{\Gamma_{0,e}}\right)^2 = \frac{1}{\sigma^2}$	$\frac{3}{4} \left(\frac{\Gamma_2}{\Gamma_{0,e}}\right)^2 = \frac{4}{3} \frac{1}{\sigma^2}$	$\frac{1}{6} \left(\frac{\Gamma_0}{\Gamma_{0,e}}\right)^2 = \frac{3}{2} \frac{1}{\sigma^2}$	$\frac{12}{5} \frac{1}{\sigma^2}$	$\frac{45}{64} \left(\frac{\Gamma_3}{\Gamma_{0,e}}\right)^2 = \frac{9}{5} \frac{1}{\sigma^2}$
$\frac{M_{x}}{M_{x,e}} = \lambda$	$\sigma^2 \frac{\Gamma_0}{\Gamma_{0,e}} = \sigma$	$\frac{3}{5}\sigma^2 \frac{\Gamma_2}{\Gamma_{0,e}} = \frac{4}{5}\sigma$	$\frac{1}{4}\sigma^2 \frac{\Gamma_0}{\Gamma_{0,e}} = \frac{3}{4}\sigma$	$\frac{3}{5}\sigma$	$\frac{3}{7}\sigma^2 \frac{\Gamma_3}{\Gamma_{0,e}} = \frac{24}{35}\sigma$
$\frac{M_{\chi,2}}{M_{\chi,2}} = \tau$	$\sigma^3 \frac{\Gamma_0}{\Gamma_{0,e}} = \sigma^2$	$\frac{1}{2}\sigma^3 \frac{\Gamma_2}{\Gamma_{0,e}} = \frac{2}{3}\sigma^2$	$\frac{1}{5}\sigma^3 \frac{\Gamma_0}{\Gamma_{0,e}} = \frac{3}{5}\sigma^2$	$\frac{2}{5}\sigma^2$	$\frac{5}{16}\sigma^3 \frac{\Gamma_3}{\Gamma_{0,e}} = \frac{1}{2}\sigma^2$
$\frac{M_{X,2,e}}{\left M_{Z}\right } = \iota$	$-\sigma(\frac{\Gamma_0}{\Gamma_{0,e}})^2 = \frac{-1}{\sigma}$	$\frac{-27}{70}\sigma(\frac{\Gamma_2}{\Gamma_{0,e}})^2 = \frac{-24}{35}\frac{1}{\sigma}$	$\frac{-1}{4}\sigma\left(\frac{\Gamma_0}{\Gamma_{0,e}}\right)^2\left(1-\frac{3\pi^2}{40}\right) =$	$\frac{-29}{840}\sigma\left(\frac{\Gamma_0}{\Gamma_{0,e}}\right)^2\left(1-\frac{21\pi^2}{232}\right)$	$\frac{-485}{1848}\sigma(\frac{\Gamma_3}{\Gamma_{0,e}})^2 = \frac{-776}{1155}\frac{1}{\sigma}$
			$\frac{-9}{4}(1-\frac{3\pi^2}{40})\frac{1}{\sigma}$	$=\frac{-174}{35}\left(1-\frac{21\pi^2}{232}\right)\frac{1}{\sigma}$	
$\frac{y_{COV}}{0.5b_e}$	$\sigma \frac{\pi}{4}$	$\sigma \frac{3\pi}{16}$	$\sigma \frac{\pi}{6}$	$\sigma \frac{\pi}{8}$	$\sigma \frac{5\pi}{32}$
$\tau = \tau(\lambda)$	$\tau = \lambda^2$	$\tau = \frac{25}{24}\lambda^2$	$\tau = \frac{16}{15}\lambda^2$	$\tau = \frac{10}{9}\lambda^2$	$\tau = \frac{1225}{1152}\lambda^2$ $\sigma = \frac{35}{24}\lambda = \sqrt{2\tau}$
$\sigma_{opt} = \frac{b}{b_e}$	$\sigma = \lambda = \sqrt{\tau}$		$\sigma = \frac{4}{3}\lambda = \sqrt{\frac{5}{3}\tau}$	$\sigma = \frac{5}{3}\lambda = \sqrt{\frac{5}{2}\tau}$	$\sigma = \frac{35}{24}\lambda = \sqrt{2\tau}$

Table 10 - Performance, relative to performance wing of span  $b_e$  with elliptic circulation distribution  $\Gamma_{0,e}(1-\hat{\eta}^2)^{1/2}$ , where  $\hat{\eta}=y/0.5b_e$ , of optimised bell-shaped circulation distributions considered in present study. Most-left to most-right columns list wings of span b and  $\eta = y/0.5b$ : Stretched elliptic distribution  $\Gamma_0(1-\eta^2)^{1/2}$ (reference); 3/2-power distribution  $\Gamma_2(1-\eta^2)^{3/2}$ ; "optimum-optimorum" distribution  $\frac{1}{2}\Gamma_0[\sqrt{1-\eta^2}-\eta^2\ln(\frac{1+\sqrt{1-\eta^2}}{|\eta|})]$ ; "barrier" distribution  $\frac{1}{2}\Gamma_0[\sqrt{1-\eta^2}-\eta^2\ln\left(\frac{1+\sqrt{1-\eta^2}}{|\eta|}\right)-\frac{2}{3}(1-\eta^2)^{3/2}]$ ; 5/2-power distribution  $\Gamma_3(1-\eta^2)^{5/2}$ . Relative span:  $\sigma=b/b_e$ .

Figure 16 presents the three moments induced by the four bell-shaped circulation distributions, considered in the present study, as function of the induced drag. From the plots it becomes clear that for prescribed root-bending moment  $M_x = \lambda M_{x,e}$ , the "optimum-optimorum" distribution (red curve), for which  $\tau = 16/(15 \lambda^2)$ , yields the lowest values of the induced drag, with reductions up to 30% with respect to the induced drag of the wing of span  $b_e$  with elliptic circulation distribution.

In the  $(D_{opt}/D_e, \lambda)$ -plane the results for the four bell-shaped circulation distributions are quite close together, i.e., within 2.5% in induced drag  $D_{opt}/D_e$ . The result for the additional fourth distribution (blue) is within 0.2%, i.e., nearly identical, to the result for the "optimum-optimorum" distribution (red). Increasing the relative span  $\sigma = b/b_e$  of the wing with elliptic circulation distribution by 10% decreases the induced drag by 17.5%, while the span-integrated section-bending-moment increases by 22.5%.

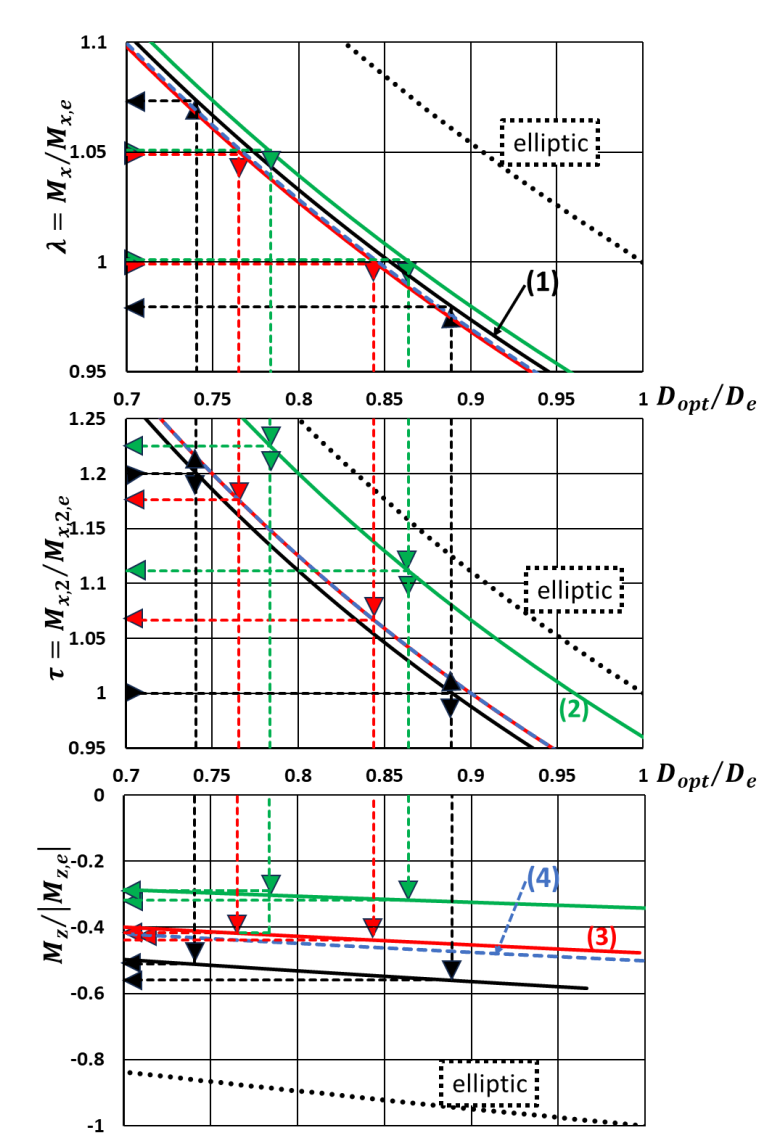


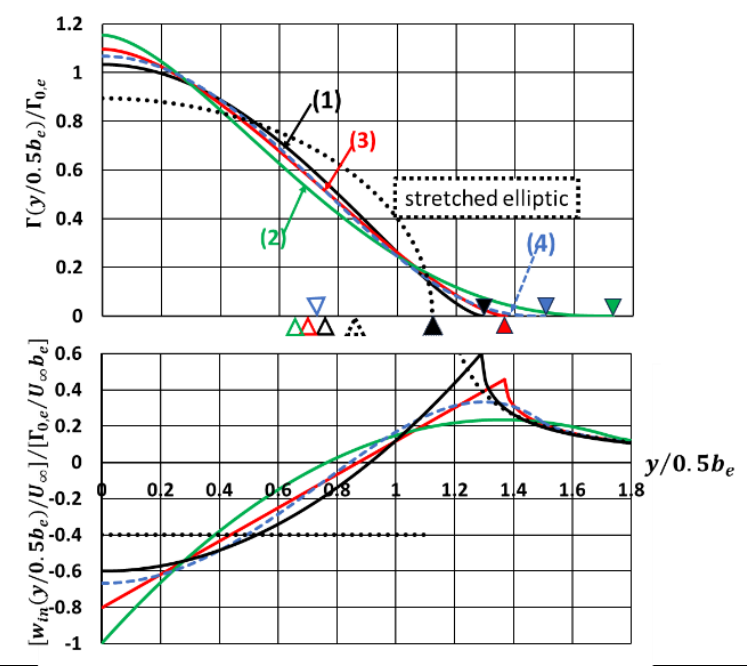
Figure 16 – Root-bending-moment  $M_x$ , spanintegrated section-bending-moment  $M_{x,2}$  and yawing moment  $M_z$ , all presented as function of induced drag  $D_{opt}$ , for four bell-shaped circulation distributions described in sections 3.2 to 3.4 for minimising induced drag for prescribed free-stream conditions  $(U_\infty,q_\infty)$  and lift  $L=L_e$ , in combination with (1) prescribed span-integrated section-bending-moment  $M_{x,2}=\tau M_{x,2,e}$ ; (2) prescribed root-bending moment  $M_x=\lambda M_{x,e}$ ; (3) both  $M_{x,2}=\tau M_{x,2,e}$  and  $M_x=\lambda M_{x,e}$ . See table 10.

Solid-black curves: distribution (1); solid-red curves: "optimum-optimorum" distribution (2); solid-green curves: "barrier" distribution (3), and; dashed-blue curves: additional, fourth, bell-shaped distribution (4). For reference, results for elliptic circulation distribution (black-dotted curves).

Horizontal/vertical straight dashed lines indicate how for given  $\lambda$  or  $\tau$  the value of  $M_{x,2}$  or  $M_x$ , respectively, of  $M_z$  and of induced drag  $D_{opt}$  can be found.

In the  $(D_{opt}/D_e, \tau)$ -plane the results for the four bell-shaped circulation distributions are also close together, i.e., within 7.5%, with the result for the additional fourth distribution (blue) exactly identical to the result for the "optimum-optimorum" distribution (green). Here the result for the first bell-shaped distribution (black) gives the most reduction in induced drag. Figure 16 also shows that, compared to the result for the stretched elliptic circulation distribution, for all four bell-shaped distributions, the vawing-moment is substantially, order 50%, smaller in magnitude.

#### Comparison at equal lift and equal induced drag



	$L/L_e = 1$ and $D_{opt}/D_e = 0.8$				
$\Gamma(\eta)$	$\sigma = b/b_e$	$\lambda = M_x/M_{x,e}$	$\tau = M_{x,2}/M_{x,2,e}$	$M_z/ M_{z,e} $	$y_{cov}/0.5b_e$
$\frac{4}{3\sigma}(1-\eta^2)^{3/2}$	1.2910	1.0328	1.1111	-0.5312	0.7605
$\left[\frac{3}{\sigma^2}\left[\sqrt{1-\eta^2}-\eta^2\ln\frac{1+\sqrt{1-\eta^2}}{ \eta }\right]\right]$	1.3693	1.0270	1.125	-0.4269	0.7170
$\frac{\frac{12}{\sigma^{\frac{1}{2}}}[\sqrt{1-\eta^{2}}-\eta^{2}\ln\frac{1+\sqrt{1-\eta^{2}}}{ \eta }-\frac{2}{3}(1-\eta^{2})^{3/2}]}{ \eta }$	1.7321	1.0392	1.2	-0.3061	0.6802
$\frac{8}{5\sigma}(1-\eta^2)^{5/2}$	1.5	1.0286	1.125	-0.4479	0.7363
$\frac{1}{\sigma}\sqrt{1-\eta^2}$	1.1180	1.1180	1.25	-0.8944	0.8781

Figure 17 – Top plot: Optimal distributions of circulation, see Figure 16. Bottom-plot: Corresponding upwash distributions. Solid-black curve: 3/2-power distribution (1); solid-red curve: "optimum-optimorum" distribution (2); solid-green curve: "barrier" distribution (3), and; dashed-blue curve: 5/2-power bell-shaped distribution (4). Black-dotted curve: stretched elliptic circulation distribution. Solid triangular symbols along horizontal axis indicate location wing tip. Open triangular symbols indicate location COV. Table provides numerical values for: dimensionless span  $\sigma = b/b_e$ ; dimensionless root-bending moment  $\lambda = M_x/M_{x,e}$ ; dimensionless span-integrated section-bending-moment  $\tau = M_{x,2}/M_{x,2,e}$ ; dimensionless yawing moment  $M_z/|M_{z,e}|$ ; location  $y_{COV}/b_e$  along span.

Noteworthy, in spite of a difference in the behavior of the distributions at the wing tip: the second derivative of the circulation is zero for the 5/2-power distribution and infinite for the "optimum-optimorum" (red) distribution. For induced-drag  $D_{opt}/D_e=0.8$ , the wing tip of the 5/2-power distribution is located in between that of the "optimum-optimorum" distribution (red) and that of the "barrier" distribution (green). At the wing tip of the latter distribution both first and second derivative of the distribution are zero, which in order to preserve the prescribed lift, forces the wing tip to a more outboard location than the tip of the "optimum-optimorum" distribution.

The table in Figure 17 provides the numerical data for the performance indicators. Clearly, the "stretched" elliptic distribution, in spite of its shorter span, leads to substantial higher values of the root-bending-moment  $M_x/M_{x,e}$  and the span-integrated section-bending-moment  $M_{x,2}/M_{x,2,e}$ , as well as the magnitude of the yawing-moment  $M_z/|M_{z,e}|$ . The "optimum-optimorum" distribution (red) and the 5/2-power distribution (blue) result in the lowest values of the root-bending-moment  $\lambda = M_x/M_{x,e}$ , the span-integrated section-bending-moment  $\tau = M_{x,2}/M_{x,2,e}$  and the magnitude of the yawing moment  $M_z/|M_{z,e}|$ . For these two distributions the root-bending moments differ 0.0016 (0.16%), the span-integrated section-bending-moments are identical and the yawing moments differs 0.0210 (4.7%).

The center of the vortex distribution COV, which is approximately the center of roll-up of the trailing vortex wake, is most inboard, at  $y_{COV}/0.5b_e=0.6802$ , i.e.,  $y_{COV}/0.5b=0.3927$ , for the very stretched "barrier" circulation distribution (green triangle). The COV of the other three bell-shaped distributions are at  $y_{COV}/0.5b=0.5236$ , 0.4909 and 0.5890, for the "optimum-optimorum" distribution (red), 5/2-power distribution and 3/2-power distribution, respectively, so, around 50% semi-span of these distributions. The stretched-elliptic distribution has its COV at  $y_{COV}/0.5b=0.7854$ , about three-quarter semi-span, i.e., much closer to the wing tip than the COV of the bell-shaped distributions.

Comparison at equal lift and equal span

An alternative to compare results for equal induced drag, is to consider the span of the wing fixed and determine the performance of the four bell-shaped distributions. The span of the wing with the 5/2-power distribution of the circulation has been chosen as the reference case. So, all wings have dimensionless span  $\sigma = b/b_e = 1.5$ . Subsequently the last row in Table 10 gives  $\lambda = M_x/M_{x,e}$  and  $\tau = M_{x,2}/M_{x,2,e}$ , different for each distribution. Figure 18 presents the plot with the distributions as function of  $y/0.5b_e$ . In addition, the Table in Figure 18 gives the numerical values of the aerodynamic performance indicators: induced drag  $D_{opt}/D_e$ , root-bending-moment  $M_x/M_{x,e}$ , span-integrated section-bending-moment  $M_{x,2}/M_{x,2,e}$ , as well as the magnitude of the yawing-moment  $M_z/|M_{z,e}|$ . Also, the location of  $y_{COV}/0.5b_e$  is listed in the table.

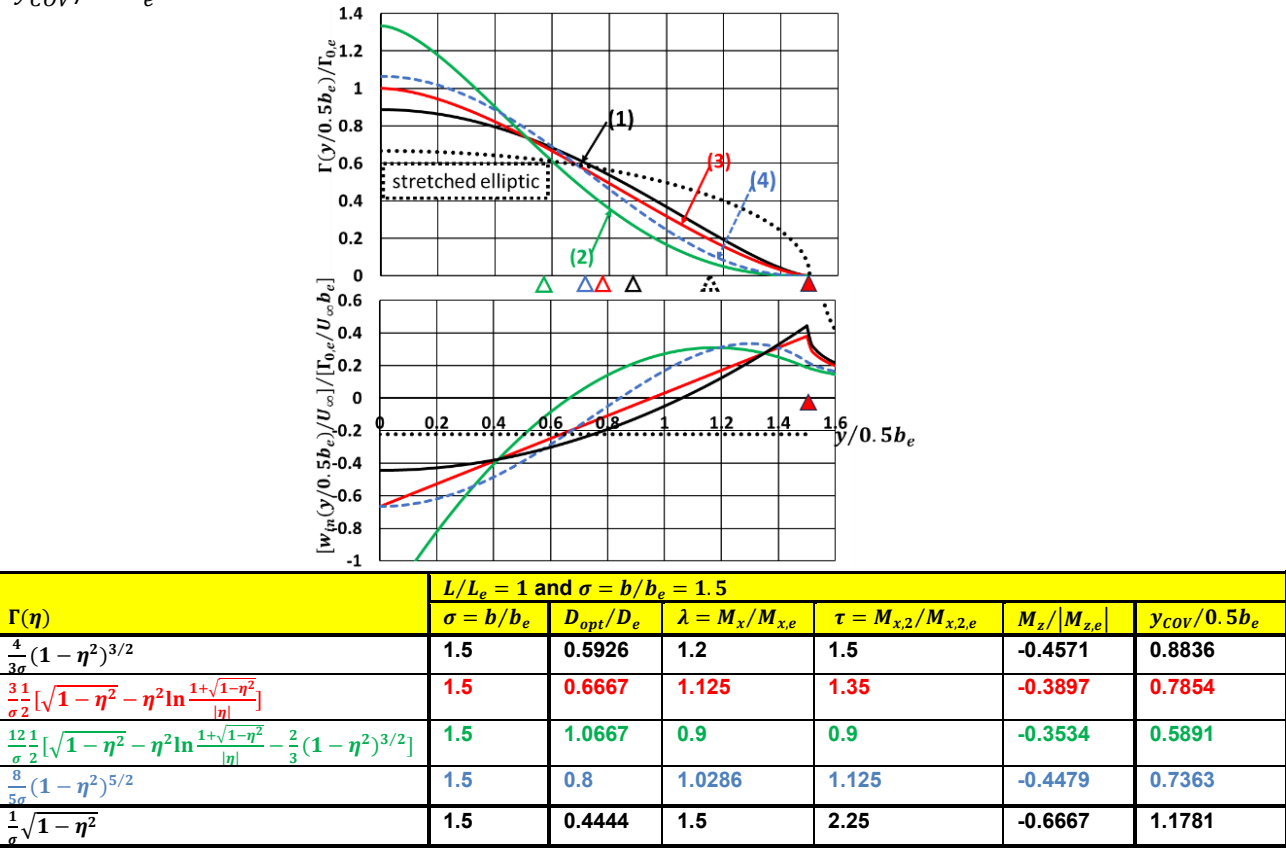


Figure 18 – Top: Optimal distributions of circulation  $\Gamma(y/0.5b_e)/\Gamma_{0,e}$ , see Figure 16. Bottom: Upwash distribution  $[w_{in}(y/0.5b_e)/U_{\infty}]/(\Gamma_{0,e}/U_{\infty}b_e)$ . Solid-black curve: 3/2-power distribution (1); solid-red curve: "optimum-optimorum" distribution (2); solid-green curve: "barrier" distribution (3), and; dashed-blue curve: additional, 5/2-power bell-shaped distribution (4). Black-dotted curve: stretched elliptic circulation distribution. Solid red triangular symbol on horizontal axis indicates location wing tip for all 5 distributions:  $y/0.5b_e = 1.5$ . Open triangular symbols indicate location COV. Table provides numerical values for: dimensionless span  $\sigma = b/b_e$ ; dimensionless induced drag  $D_{opt}/D_e$ ; dimensionless root-bending moment  $\lambda = M_x/M_{x,e}$ ; dimensionless span-integrated section-bending-moment  $\tau = M_{x,2}/M_{x,2,e}$ ; dimensionless yawing moment  $M_z/|M_{z,e}|$  and; location COV.

The top plot in Figure 18 shows that near the wing tip the black (1) 3/4-power distribution and the red (3) "optimum-optimorum" distribution behave similarly: at the wing tip zero function value and zero first derivative, but a square-root singularity in the second derivative of the distribution. Near the wing tip the 3/2-power distribution (1) is above the "optimum-optimorum" distribution. In the wing-root region this is the other way around. The 5/2-power distribution (4) and the "barrier" distribution (2) behave in a similar fashion, although at the wing tip, these two distributions have, apart from zero function value and zero first derivative, in addition zero second derivative. The lower plot in Figure 18 presents the upwash distributions corresponding with the circulation distributions. Note that also a small part of the distribution for  $\eta > 1$  has been included, revealing the continuation of the upwash distribution outboard of the wing tip. Note that the section-induced-drag equals minus section-circulation times section-upwash. Since the circulation always has positive sign, negative section-upwash corresponds to positive section drag and positive section upwash corresponds to negative section-drag (i.e., section-thrust). For example, in case of the "barrier" distribution (green), section-drag is negative in the region between  $y/0.5b_e = 0.65$  and the tip at  $y/0.5b_e = 1.5$ . However, since the

section-circulation has high values in the inboard part of the span, the section-thrust is not large enough to render the overall induced drag small, i.e.,  $D_{opt}/D_e = 1.0667$ . The other three bell-shaped distributions do result in a sizable reduction of the induced drag.

The induced drag of the 3/2-power distribution is lower than that of the "optimum-optimorum" distribution, which is associated with the lower strength of the vortex distribution  $\gamma_x$  (minus first derivative circulation) of the 3/2-power distribution in the mid semi-span region. Similarly, the induced drag of the "barrier" distribution (2) is higher (even > 1) than that of the 5/2-power distribution (4) because of the higher strength of the vortex distribution in the mid semi-span region. Clearly, the induced drag of the stretched-elliptic distribution is lowest because of the low level of circulation in the root region of the wing. However, the magnitude of the root-bending-moment, the span-integrated section-bending-moment and the yawing moment are substantially larger than those of the bell-shaped distributions. As far as the COV is concerned, the "barrier" distribution (green) has its COV most inboard, at  $y_{COV}/0.5b_e = 0.5891$ , i.e.,  $y_{COV}/0.5b = 0.3927 = \pi/8$ . The COV of the stretched-elliptic distribution is most outboard at  $y_{COV}/0.5b_e = 0.7854 = \pi/4$ . The remaining three bell-shaped distribution have their COV around  $y_{COV}/0.5b_e = 0.8$ , i.e.,  $y_{COV}/0.5b = 0.53 = \pi/6$ 

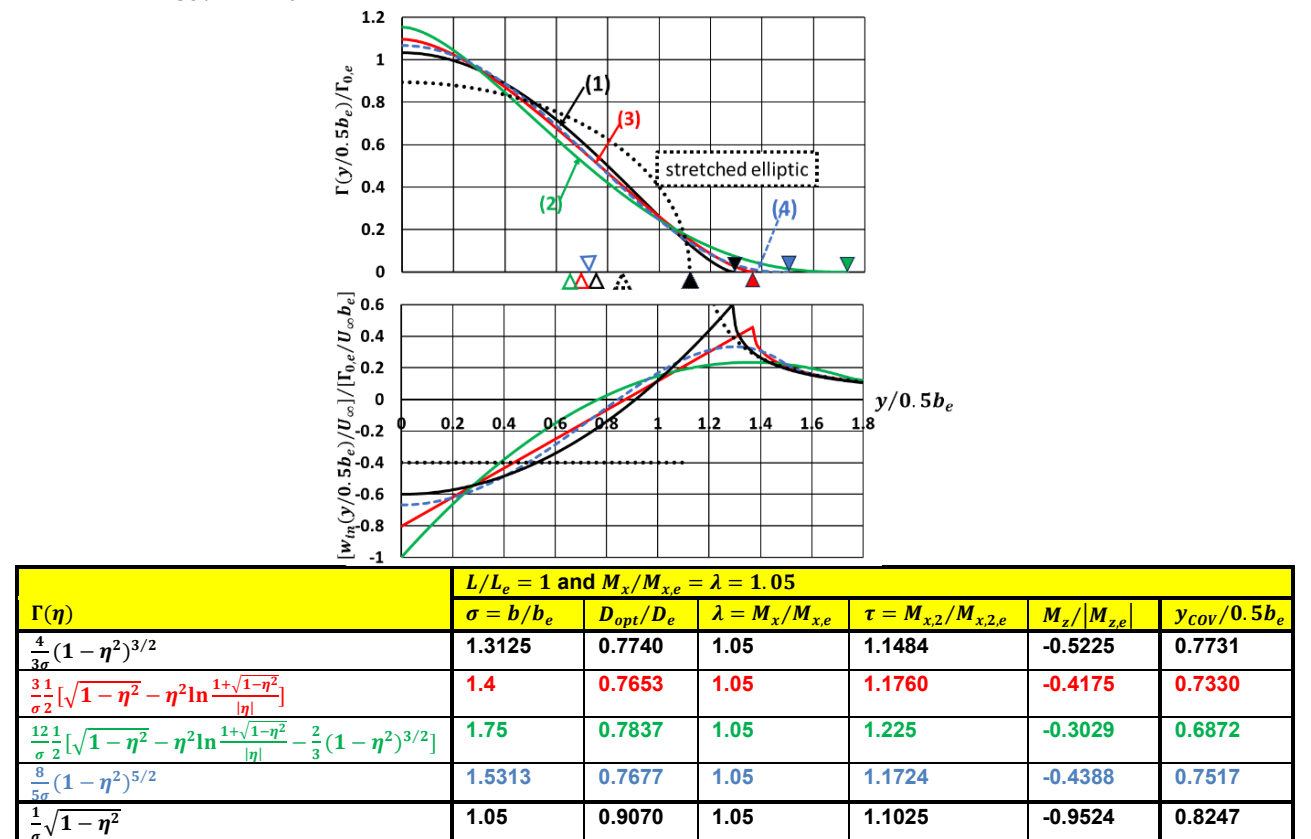


Figure 19 – Top: Optimal distributions of circulation  $\Gamma(y/0.5b_e)/\Gamma_{0,e}$ , see Figure 16. Bottom: Upwash distribution  $[w_{in}(y/0.5b_e)/U_{\infty}]/(\Gamma_{0,e}/U_{\infty}\,b_e)$ . Solid-black curve: 3/2-power distribution (1); solid-red curve: "optimum-optimorum" distribution (2); solid-green curve: "barrier" distribution (3), and; dashed-blue curve: additional, 5/2-power bell-shaped distribution (4). Black-dotted curve: stretched elliptic circulation distribution. Solid red triangular symbols on horizontal axis indicate location wing tips. Open triangular symbols indicate location COV. Table provides numerical values for: dimensionless span  $\sigma = b/b_e$ ; dimensionless induced drag  $D_{opt}/D_e$ ; dimensionless root-bending moment  $\lambda = M_x/M_{x,e}$ ; dimensionless span-integrated section-bending-moment  $\tau = M_{x,2}/M_{x,2,e}$ ; dimensionless yawing moment  $M_z/|M_{z,e}|$  and; location COV along span of wing.

For the case that the four bell-shaped circulation distribution have equal root-bending moment  $\lambda=M_x/M_{x,e}$ =1.05, the circulation distributions are close to each other, but for the wing-tip region, where the differences in the tip conditions affect the wing span  $\sigma=b/b_e$ . The induced drag  $D_{opt}/D_e$  of the four bell-shaped distributions does not differ very much, all are in the narrow range [0.7677,0.7837]. Actually, this was already evident from the results for  $M_x/M_{x,e}$  vs.  $D_{opt}/D_e$ , presented in Figure 16, which illustrate the closeness of the curves for the four bell-shaped distributions. The induced drag of  $D_{opt}/D_e=0.9070$  for the stretched-elliptic distribution is 15% above that of the bell-shaped distributions. Similarly, the results in Figure 17 for constant induced drag show values of  $M_x/M_{x,e}$  that are within a narrow band in the  $(D_{opt}/D_e, M_x/M_{x,e})$ -plane. In the table in Figure 19, the values of the span-

integrated section-bending-moment  $M_{x,2}/M_{x,2,e}$  of the bell-shaped circulation distributions are within a slightly wider band. The results for the smallest-span 3/2-power (black) distribution are the best.

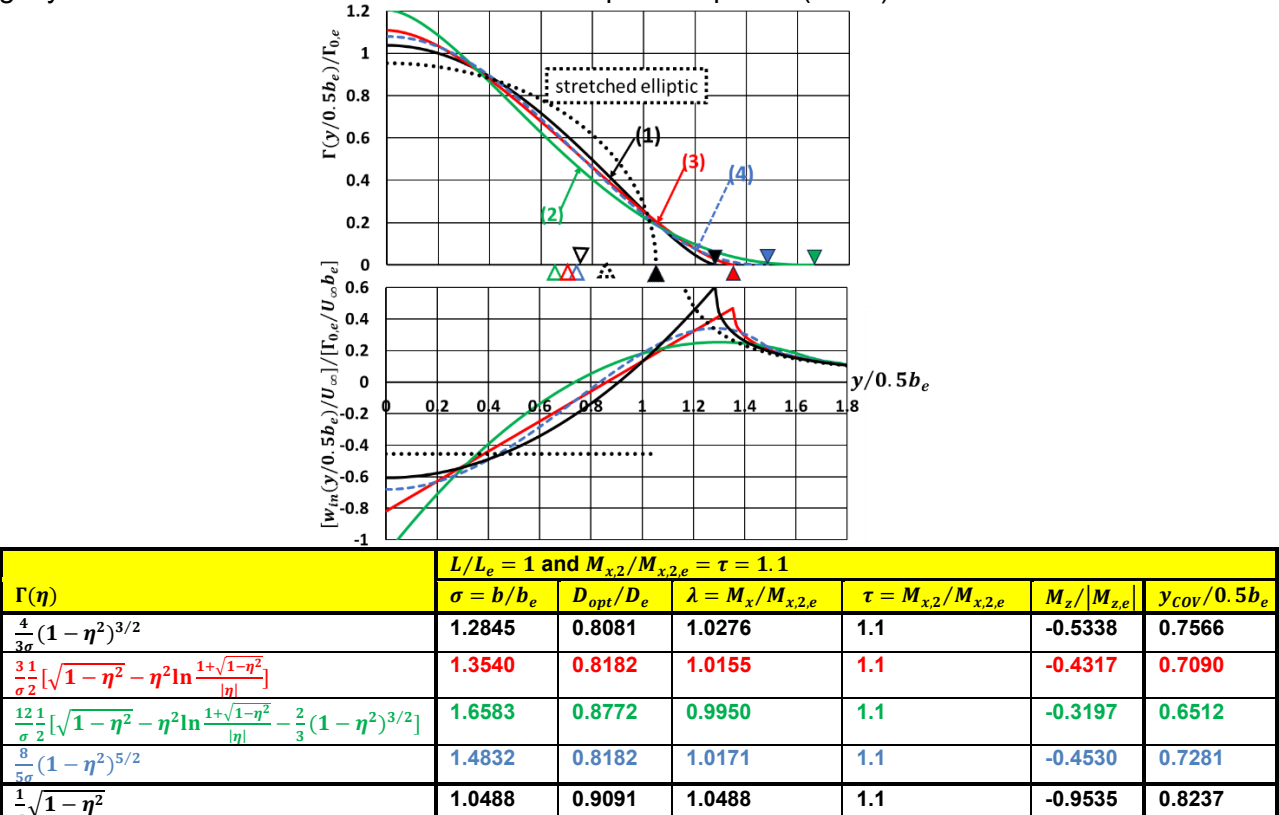
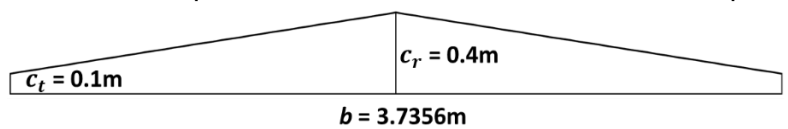


Figure 20 – Top: Optimal distributions of circulation  $\Gamma(y/0.5b_e)/\Gamma_{0,e}$ , see Figure 16. Bottom: Upwash distribution  $[w_{in}(y/0.5b_e)/U_{\infty}]/(\Gamma_{0,e}/U_{\infty}b_e)$ . Solid-black curve: 3/2-power distribution (1); solid-red curve: "optimum-optimorum" distribution (2); solid-green curve: "barrier" distribution (3), and; dashed-blue curve: additional, 5/2-power bell-shaped distribution (4). Black-dotted curve: stretched elliptic circulation distribution. Solid red triangular symbol on horizontal axis indicates location wing tip for all 5 distributions:  $y/0.5b_e=1.5$ . Open triangular symbols indicate location COV. Table provides numerical values for: dimensionless span  $\sigma=b/b_e$ ; dimensionless induced drag  $D_{opt}/D_e$ ; dimensionless root-bending moment  $\lambda=M_x/M_{x,e}$ ; dimensionless span-integrated section-bending-moment  $\tau=M_{x,2}/M_{x,2,e}$ ; dimensionless yawing moment  $M_z/|M_{z,e}|$  and; location COV.

Finally, Figure 20 presents the comparison of the aerodynamic performance of the four bell-shaped distributions for the case the span-integrated section-bending-moment is kept the same for each distribution at  $\tau = M_{x,2}/M_{x,2,e} = 1.1$ . For this case the induced drag for all bell-shaped distributions but the "barrier" distribution, falls within the narrow band [0.8081,0.8182]. The "barrier" distribution, with its longer span, features a 6% higher induced drag, while the stretched-elliptic distribution's induced drag is 10% higher. The table in Figure 20 also shows that the variation in the root-bending-moment  $\lambda = M_x/M_{x,e}$  is small.

## 4 Prandtl-D wing

In the literature the aerodynamics of the so-called Prandtl-D wing has received quite some attention. Such a flying wing has a bell-shaped distribution of the circulation: the 3/2-power distribution.



From the report of Bowers [6] the specification of the trapezoidal wing of the RC sub-scale flying-wing aircraft (25% Horten H Xc glider) has been extracted as:

Span: b = 3.7356 m;

Chord:  $c(\eta) = c_r(1 - |\eta|) + c_t |\eta|$ , with  $c_r = 0.4$ m and  $c_t = 0.1$ m, so that  $\bar{c} = 0.25$ m; (22a)

Aspect ratio: AR = 14.9422;

Sweep: not taken into account in present study; Wing dihedral: not taken into account in present study.

The specified data on root-section and (symmetric) tip section have been used to determine, using a panel method, the zero-lift angle of attack as:

$$\alpha_0(\eta) = -0.1178(1 - |\eta|) \text{ deg.}$$
 (22b)

The list with the distribution of the wing-twist angle has been least-squares fitted in the third-degree polynomial:

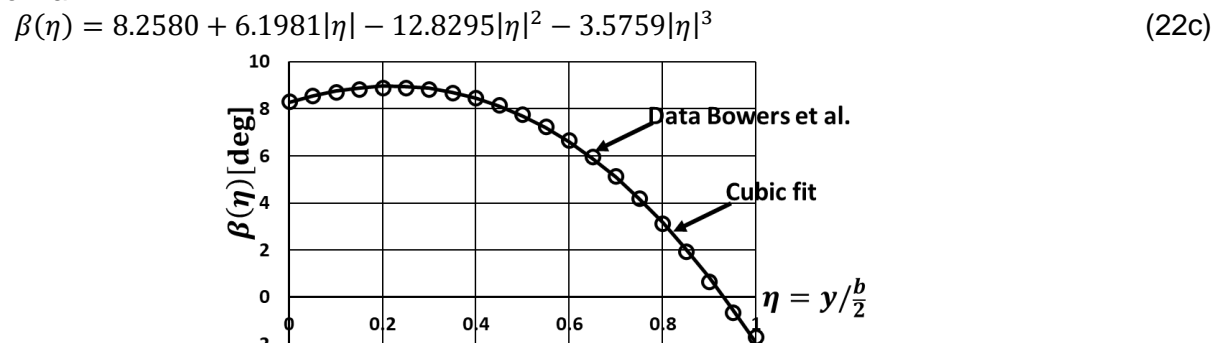


Figure 21 – Prandtl-D wing: section wing-twist angle  $\beta(\eta)$ .

Figure 21 shows the excellent agreement of the present fit with the data from Bowers' report [6], with the L2-norm of the difference equal to 0.01 deg. The geometric twist of the wing increases the section angle of attack in the root section and lowers it in the tip region. Such type of distribution of  $\beta(\eta)$ , with unloading the tip region, is necessary to generate a bell-shaped distribution of the circulation.

Now all data, except the angle-of-attack  $\alpha$  of the wing, required to solve Prandtl's Lifting-line integro-differential equation (1c) is available. In dimensionless form Prandtl's equation becomes:

$$\frac{\Gamma(\eta)}{U_{\infty}\bar{c}} = \frac{1}{2} \frac{c(\eta)}{\bar{c}} a_0 \left[ \alpha - \alpha_0(\eta) + \beta(\eta) + \frac{w_{in}(\eta)}{U_{\infty}} \right], \text{ for } |\eta| < 1 \text{ and } \Gamma(|\eta| \uparrow 1) = 0,$$
(23a)

with  $a_0$  the slope of the 2D-section-lift curve, chosen here as a constant  $a_0 = 2\pi$ .

The upwash  $w_{in}(\eta)$ , induced at the lifting line by the wake vortex sheet downstream of the lifting line, expressed as the Cauchy-Principle-Value integral, follows from Eq. (1d) as

$$\frac{w_{in}}{U_{\infty}}(|\eta|<1) = \frac{1}{4\pi} \text{CPV} \int_{-\frac{1}{U_{\infty}}}^{1} \frac{\gamma_x}{\eta - \eta'} (\eta') \frac{d\eta'}{\eta - \eta'}. \tag{23b}$$

The *x*-component of the wake vortex distribution equals  $\frac{\gamma_x(\eta t)}{U_{\infty}} = -\frac{2}{AR} \frac{d}{d\eta'} \frac{\Gamma(\eta')}{U_{\infty}\bar{c}} (\eta')$ . (23c)

Eq. (23a) is solved numerically employing a second-order panel method that provides the solution in the form of function value, first and second derivative of the circulation at the midpoints of the panels used to discretise the lifting line.

Eq. (23) has been applied for a sequence of angles-of-attack, for which the lift coefficient and the induced-drag coefficient have been obtained, see Figure 20.

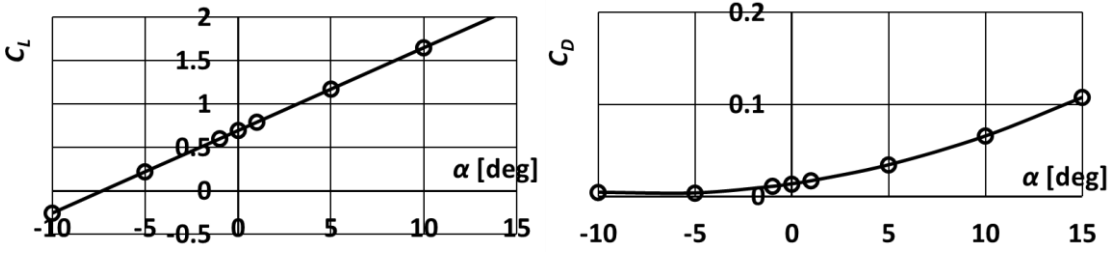


Figure 22 – Prandtl-D wing: Lift coefficient  $C_L = L/q_{\infty}b\bar{c}$  and induced-drag coefficient  $C_D = D/q_{\infty}b\bar{c}$  vs. angle-of-attack  $\alpha$ .

Figure 22 shows, as expected, the linear dependence of the lift coefficient  $C_L$  on angle-of-attack  $\alpha$  and the quadratic dependence of induced drag on angle-of-attack  $\alpha$  and thus on lift coefficient  $C_L$ . The numerical results show that the zero-lift angle-of-attack of the wing  $\alpha_{L=0}$  is close to -7.3 deg, while the design lift coefficient, according to Bowers [6], is  $C_{L,design} = 0.6$ , which is achieved for  $\alpha = -1$  deg. The slope of the lift curve is  $dC_L/d\alpha = 1.74\pi$ . The results in Figure 22 correlate with the wind-tunnel data of Zelenka et al. [31] (Figure 5) acquired for a Prandtl-D test model, at  $Re_{m,a,c} = 210k$ .

The distribution of the circulation and the distribution of the upwash, computed for design condition  $C_{L.design}$ = 0.6, are presented in Figure 23.

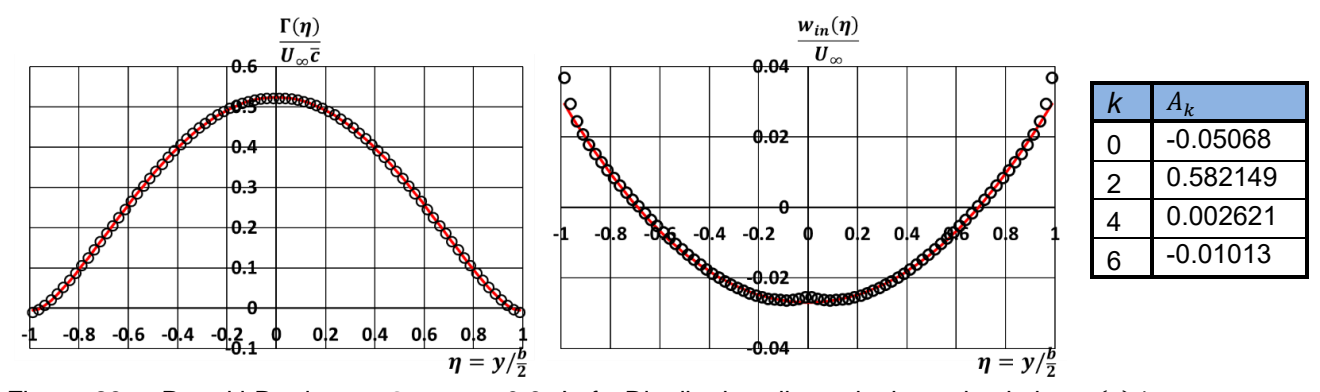


Figure 23 – Prandtl-D wing at  $C_{L,design}$ = 0.6. Left: Distribution dimensionless circulation  $\Gamma(\eta)/U_{\infty}\bar{c}$  vs.  $\eta=$ y/0.5b. Middle: Distribution dimensionless upwash  $w_{in}(\eta)/U_{\infty}$  vs.  $\eta = y/0.5b$ . Right: Table with coefficients in series expansion circulation and upwash distributions. Black open circles: numerical solution. Solid red curve: Four term least-squares fit. Number of panels: N = 80.

In order to obtain insight in the character of the found circulation distribution, the numerical solution has been subjected to a least-squares fit consisting of four terms, for the circulation distribution:

$$\frac{\Gamma(\eta)}{U_{\infty}\bar{c}} = A_0 (1 - \eta^2)^{1/2} + A_2 (1 - \eta^2)^{3/2} + A_4 (1 - \eta^2)^{5/2} + A_6 (1 - \eta^2)^{7/2}.$$
(24a)

Using the expressions for the upwash induced by each of these terms yields: 
$$\frac{w_{in}(\eta)}{U_{\infty}} = \frac{-1}{2AR} \left[ A_0 + 3A_2(-\frac{1}{2} + \eta^2) + 5A_4(\frac{3}{8} - \frac{3}{2}\eta^2 + \eta^4) + 7A_6(\frac{5}{16} - \frac{15}{8}\eta^2 + \frac{5}{2}\eta^4 - \eta^6) \right]$$
 (24b)

L2-norm fit circulation distribution: 1.37×10<sup>-3</sup> and upwash distribution: 1.41×10<sup>-3</sup>, respectively.

Figure 23 shows that the circulation distribution generated for the prescribed wing planform and prescribed  $\Delta \alpha = \alpha - \alpha_0(\eta) + \beta(\eta)$  is indeed a bell-shaped distribution, e.g., compare Figure 23 and black lines in Figure 20. The least-squares four-term fit consisting of the elliptic distribution and three bell-shaped distributions illustrates that indeed, the dominating term is Horten's bell-shaped distribution  $A_2(1-\eta^2)^{3/2}$ .

The series for the upwash, Eq. (24b), consists of the polynomial upwash generated by the corresponding terms in Eq. (24a). The first three have been calculated in section 3. Computing the 7/2power term requires some algebra, but is not too cumbersome, see also Appendix C. Note that the order of the even-degree polynomials in the expression for the upwash corresponds to the order of the corresponding terms in the circulation distribution written as  $(1 - \eta^2)^{(k+1)/2} = P_{2k}(\eta)(1 - \eta^2)^{1/2}$ , for k = 0, 2, 4 and 6.

#### Determination distribution required twist

So far, the aerodynamic analysis of the Prandtl-D wing has been carried out for the distribution of the section twist angle  $\beta(\eta)$ , specified in Figure 19. Subsequently it was shown that the resulting distribution of the circulation is dominated by the bell-shaped distribution  $(1 - \eta^2)^{3/2}$  In a wing-design process, one has to determine the distribution of the twist angle  $\beta(\eta)$  that generates the bell-shaped circulation distribution. This process would determine the twist angle distribution from Prandtl's integro-differential equation, Eq. (23a), by substituting:

- 1.
- the required circulation distribution  $\Gamma(\eta) = \Gamma_2 (1 \eta^2)^{3/2}$ ; the corresponding upwash distribution  $\frac{w_{in}(\eta)}{u_{\infty}} = \frac{-1}{2AR} \Gamma_2 (-\frac{1}{2} + 3\eta^2)$ ; 2.
- the chosen distribution of the section chord  $c(\eta)$ ; and 3.
- the chosen distribution of the section zero-lift angle  $\alpha_0(\eta)$ . 4.

For the present case one obtains:

$$\Delta \alpha(\eta) = \alpha - \alpha_0(\eta) + \beta(\eta) = \frac{\Gamma_2}{U_{\infty}\bar{c}} \left[ \frac{2}{a_0} \frac{\bar{c}}{c(\eta)} (1 - \eta^2)^{3/2} + \frac{3}{2AR} \left( \frac{1}{2} - \eta^2 \right) \right], \text{ with } AR = b/\bar{c}.$$

From Table 3 it follows, with  $\Gamma_{20}=0$ ,  $\Gamma_{22}=\Gamma_2$  and  $\frac{\Gamma_2}{U_\infty \bar{c}}=\frac{8}{3\pi}\mathcal{C}_L$ , that, with Eq. (20n):

$$\Delta\alpha(\eta) = \frac{8}{3\pi} C_L \frac{1}{2} (c_r + c_t) \left[ \frac{2}{a_0} \frac{(1 - \eta^2)^{3/2}}{c_r (1 - |\eta|) + c_t |\eta|} + \frac{3}{2b} \left( \frac{1}{2} - \eta^2 \right) \right]$$
 (25)

 $\Delta\alpha(\eta) = \frac{8}{3\pi} C_L \frac{1}{2} (c_r + c_t) \left[ \frac{2}{a_0} \frac{(1 - \eta^2)^{3/2}}{c_r (1 - |\eta|) + c_t |\eta|} + \frac{3}{2b} \left( \frac{1}{2} - \eta^2 \right) \right] \tag{25}$  Substituting  $C_L = 0.6$ ,  $c_r = 0.4$ m,  $c_t = 0.1$ m,  $a_0 = 2\pi$  and b = 3.7356m yields the curve for  $\Delta\alpha(\eta)$  in Figure 24. Adding  $\alpha_0(\eta)$ , given in Eq. (22b) and subtracting the design angle-of-attack of -1 deg, results in the desired curve for  $\beta(\eta)$ .

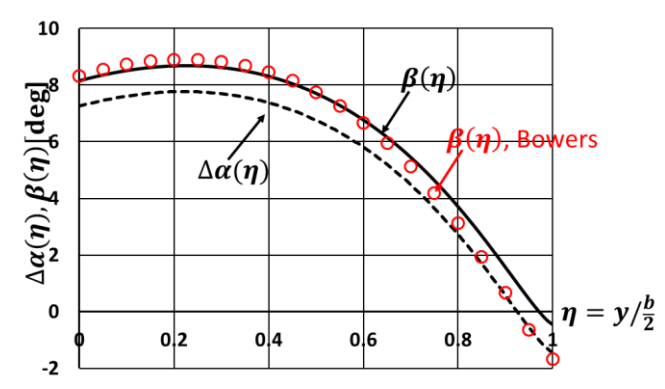


Figure 24 – Prandtl-D wing at  $C_{L,design} = 0.6$ ,  $\alpha_{design} = -1$  deg: Comparison computed distribution desired wing twist angle  $\beta(\eta)$ , required to generate bell-shaped circulation distribution, with distribution used by Bowers [6]. Also presented  $\Delta\alpha(\eta) = \alpha - \alpha_0(\eta) + \beta(\eta)$ .

Figure 24 presents the results for the desired wing twist angle vs.  $\eta$ . The agreement with the distribution used by Bowers [6] is quite reasonable. Only in the tip region the two results diverge giving a difference of 1 degree at the tip.

# 5. Wing Robotic Bird Robird

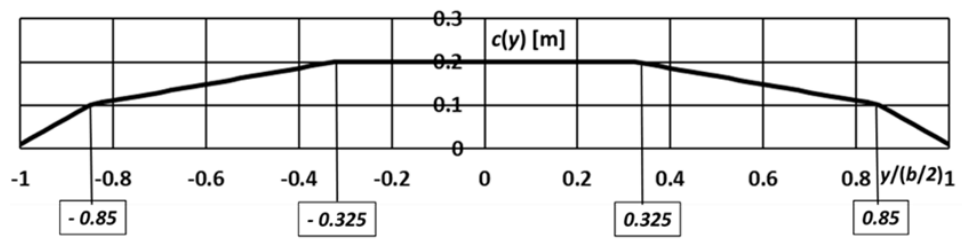
The wind-tunnel model of the Robird (Figure 1f) is a wing-only half-model. Its spanwise distribution of the chord c(y) (Figure 25) has been simplified to a piece-wise linear distribution, symmetric with respect to the plane-of-symmetry y=0. The semi-span is subdivided in three parts, see Figure 25:

```
y \in [0.0, 0.182] \text{ m} : c(y) = 0.2 \text{ m}
```

 $y \in [0.182, 0.476] \text{ m}: c(y) = [0.200(0.476 - y) + 0.102(y - 0.182)]/0.294 \text{ m}$ 

 $y \in [0.476, 0.560] \text{ m}$ : c(y) = [0.102(0.560 - y) + 0.010(y - 0.476)]/0.084 m

Figure 25 provides the dimensions of the wing planform.



b	1.12 m
c(0)	0.2 m
<u></u> <u> </u>	0.1527 m
AR	7.34

Figure 25 - Spanwise distribution of chord c(y/0.5b) of simplified planform of wind-tunnel model Robird. Table provides the main geometric parameters.

In the present analysis the gap between the root of the wing and the wall of the wind tunnel is closed for reasons of convenience of modeling. Therefore, the span of the wing of the simplified configuration extends from the plane of symmetry y=0 to the tip of the wing.

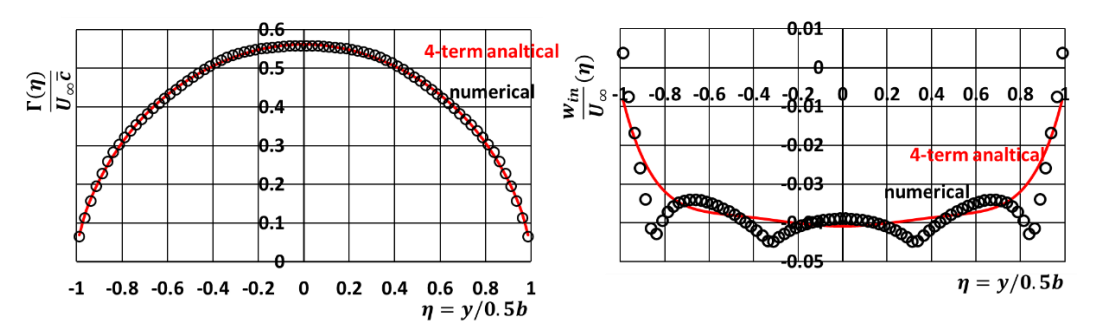
Furthermore, it is assumed that:

Section zero-lift angle-of-attack  $\alpha_0(y) = -5$  deg is constant;

Section twist angle  $\beta(y) = 0$ ; and

Angle of attack, equal to wing pitch angle, is in the range  $\alpha = -10(5)15$  deg.

In the left plot of Figure 26 the symbols denote the spanwise distribution of the dimensionless circulation  $\Gamma(y/0.5b)/U_\infty \bar{c}$  as numerically solved from Eq. (24a) for  $\alpha=5$  deg. The red solid line represents the four-term least-squares fit, in terms of the sum  $A_{2k}(1-\eta^2)^{(k+1)/2}$ , k=0, 2, 4 and 6 of the calculated circulation distribution. This fit agrees quite well with the numerical solution. The coefficients in the expansion have been determined through the least-squares fit and are listed in the table in Figure 26. It shows that the first three terms are dominant, i.e., the elliptic and two bell-shaped distributions: the 3/2-power and the 5/2-power distributions. Rewriting the circulation distribution in terms of a polynomial times the square-root yields  $B_{2k}\eta^{2k}(1-\eta^2)^{1/2}$ , with k=0, 2, 4 and 6. It reveals that the first term,  $B_0(1-\eta^2)^{1/2}$ , with  $B_0=A_0+A_2+A_4+A_6$ , is the dominant term.



k	$A_k$
0	0.43063
2	0.33502
4	-0.3493
6	0.14641

Figure 26 - Lifting-line solution for gliding flight Robird. Left: Spanwise distribution circulation  $\Gamma/U_\infty \bar{c}$  vs.  $\eta=y/0.5b$ . Symbols denote numerical solution (N=80); red lines denote four-term least-squares fits based on Eqs. (24a, b). Right: spanwise distribution induced upwash  $w_{in}/U_\infty$  vs.  $\eta=y/0.5b$ .  $\alpha=5$  deg,  $\alpha_0=-5$  deg. Table provides constants  $B_k$ , k=0, 2, 4, 6 in Eqs. (24a, b). L2-norm fit equals  $4.2\times10^{-3}$  and  $4.9\times10^{-3}$  for the circulation distribution and the upwash distribution, respectively.

Figure 26–right, shows that the four-term fit gives a reasonable match of the numerical solution of the upwash  $w_{in}(\eta)/U_{\infty}$ . Note that the numerical upwash distribution features discontinuities in the slope at locations at which the distribution of the chord  $c(\eta)$  is slope-discontinuous, see Figure 25.

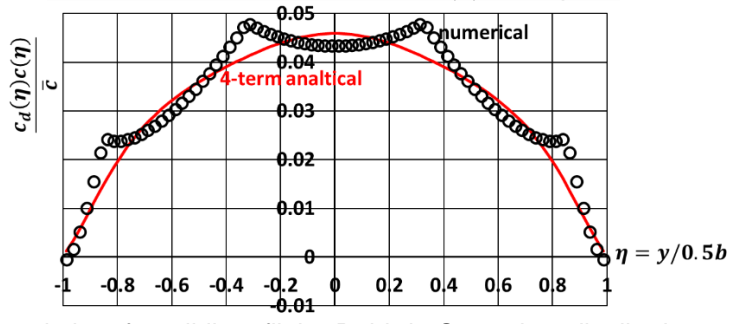
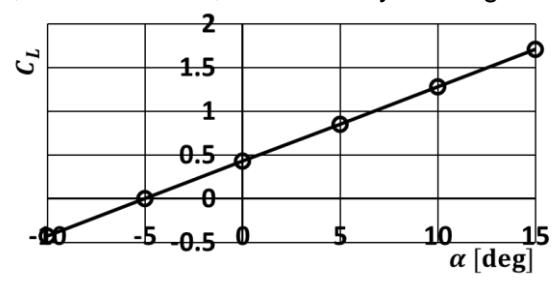


Figure 27 - Lifting-line solution for gliding flight Robird. Spanwise distribution section drag coefficient  $c_d(\eta)c(\eta)/\bar{c}$  vs.  $\eta=y/0.5b$ . Symbols denote numerical solution; solid red line denotes four-term least-squares fit based on Eqs. (24a, b).  $\alpha=5$  deg,  $\alpha_0=-5$  deg. N=80.

The distribution of the section-drag coefficient  $c_d(\eta)c(\eta)/\bar{c} = -2\left[w_{in}(\eta)/U_{\infty}\bar{c}\right]$ , see Table 1, is presented in Figure 27, derived from the numerical solution (symbols), as well as from Eqs. (24a, b) (red line). This shows that the four-term least-squares fit of the product of the circulation distribution and that of the upwash distribution, matches the numerical results quite reasonably (L2-norm difference equals  $3.3\times10^{-3}$ ). The location of the slope discontinuities corresponds to the location of the discontinuities in the chord distribution  $c(\eta)$ . Note that the section drag is positive along almost the entire span, only very close to the wing tips the section-drag turns into section-thrust. However, as illustrated in [9], [32], for the case of flapping flight. the Robird generates, cycle-integrated, not only lift, but also thrust, as shown by utilising the unsteady-flow extension of the lifting-line theory.



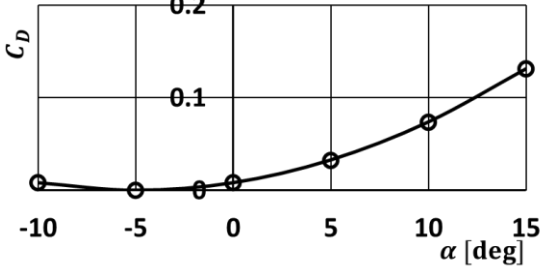


Figure 28 - Lifting-line solution for gliding flight Robird. Left: Overall lift coefficient  $C_L$  as function of angle-of-attack  $\alpha$ , calculated from numerical solution. Right: Overall (induced) drag coefficient  $C_D$  as function of angle-of-attack, calculated from numerical solution.  $\alpha_0 = -5 \text{ deg. } N = 80$ .

In Figure 28 the overall lift coefficient  $\mathcal{C}_L$  and the overall (induced-)drag coefficient  $\mathcal{C}_D$  are presented as function of angle-of-attack  $\alpha$ , derived from the numerical values obtained from the method based on the lifting-line theory. The lift coefficient is linear in terms of  $\alpha-\alpha_0$ , the induced drag coefficient is quadratic in  $\alpha-\alpha_0$ . i.e., quadratic in lift coefficient  $\mathcal{C}_L$ . Given the numerical data, or using the expressions from the 4-term fit of the circulation distribution, the lift coefficient  $\mathcal{C}_L$  and the induced-

drag coefficient  $C_D$  can be expressed to give a perfect fit, as

$$C_L = \frac{a_0}{1 + \frac{a_0}{\pi ARe_\ell}} (\alpha - \alpha_0)$$
, and  $C_D = \frac{C_L^2}{\pi ARe_d}$ , respectively, (26)

with the span-efficiencies for lift and drag,  $e_{\ell} = 0.9594$  and  $e_{d} = 0.9642$ , respectively.

# 6. Vortex Wake Roll-Up

The distribution of the circulation  $\Gamma(\eta)$  of the lifting line, or rather, the associated vortex distribution  $\frac{\gamma_x(y)}{U_\infty} = \frac{-1}{U_\infty} \frac{d}{dy} \Gamma(y)$  along the span, determines not only the flow field, it also determines the way in which the vortex wake rolls up. In the present notation  $\frac{\gamma_x(\eta)}{U_\infty} = \frac{\Gamma_{0,e}}{U_\infty b_e} \frac{-2}{\sigma} \frac{d}{d\eta} \frac{\Gamma(\eta)}{\Gamma_{0,e}}$ . To get insight in the tendency of the wake to roll up, consider the induced velocity at points along the lifting line  $|\eta| < 1$  and at points on its extension from the wing tip outwards  $|\eta| > 1$ . Considered are three cases: Stretched elliptic circulation distribution, the 3/2-power bell-shaped distribution and the 5/2-power bell-shaped distribution, i.e., a selection from the solutions presented in Figure 18.

	Elliptic	3/2-power bell-shaped	5/2-power bell-shaped
$\frac{\Gamma(\eta)}{\Gamma_{0,e}}$	$\frac{1}{\sigma}\sqrt{1-\eta^2}$	$\frac{4}{3\sigma}(1-\eta^2)^{3/2}$	$\frac{8}{5\sigma}(1-\eta^2)^{5/2}$
$\frac{\gamma_x(\eta)}{U_\infty} / \frac{\Gamma_{0,e}}{U_\infty b_e}$	$\frac{1}{\sigma} \frac{2}{\sigma} \frac{\eta}{\sqrt{1 - \eta^2}}$	$\frac{4}{3\sigma}\frac{2}{\sigma}3\eta\sqrt{1-\eta^2}$	$\frac{8}{5\sigma} \frac{2}{\sigma} 5\eta (1-\eta^2)^{3/2}$
$\frac{w_{in}( \eta <1)}{U_{\infty}}/\frac{\Gamma_{0,e}}{U_{\infty}b_{e}}$	$\frac{1}{\sigma} \frac{-1}{2\sigma}$	$\frac{4}{3\sigma}\frac{-1}{2\sigma}3(\frac{1}{2}-\eta^2)$	$\frac{8}{5\sigma^2} \frac{-1}{2\sigma^2} 5(-\frac{3}{8} - \frac{3}{2}\eta^2 + \eta^4)$
$\frac{w_{in}( \eta >1)}{U_{\infty}} / \frac{\Gamma_{0,e}}{U_{\infty}b_{e}}$	$\frac{1}{\sigma^2\sigma} \left(1 - \frac{ \eta }{\sqrt{\eta^2 - 1}}\right)$	$\frac{\frac{4}{3\sigma} \frac{-1}{2\sigma} 3(\frac{1}{2} - \eta^2 +  \eta  \sqrt{\eta^2 - 1})$	$\frac{8 - 1}{5\sigma 2\sigma} 5(-\frac{3}{8} - \frac{3}{2}\eta^2 + \eta^4 -  \eta (1 - \eta^2)^{3/2})$

Table 11 – Expressions for elliptic and two bell-shaped distributions: Circulation distribution  $\Gamma(\eta)/\Gamma_{0,e}$ ; vortex distribution  $[\gamma_x(\eta)/U_\infty]/[\Gamma_{0,e}/U_\infty b_e]$  and upwash distribution  $[w_{in}(\eta)/U_\infty]/[\Gamma_{0,e}/U_\infty b_e]$  along lifting line  $(|\eta| < 1)$  and along extensions  $(|\eta| > 1)$ .

The expressions for the induced upwash were included in Tables 2 - 8. Table 11 provides a summary of the expressions for circulation distribution  $\Gamma(\eta)$ , the vortex distribution  $\gamma_{\chi}(\eta)$  and the upwash distribution  $w_{in}(\eta)$  for the three cases considered. The lift  $(L/q_{\omega}b_e^2)/(\Gamma_{0,e}/U_{\omega}b_e) = \sigma \int_{-1}^1 [\Gamma(\eta)/\Gamma_{0,e}] d\eta$  and span b are identical for these three distributions. The distribution of the circulation and of the upwash along the wing span were presented in Figure 18. For the sake of completeness, Figure 29 again presents the vortex distribution along the wing span, as well as the induced upwash distribution not only along the wing span but also along its outward extension.

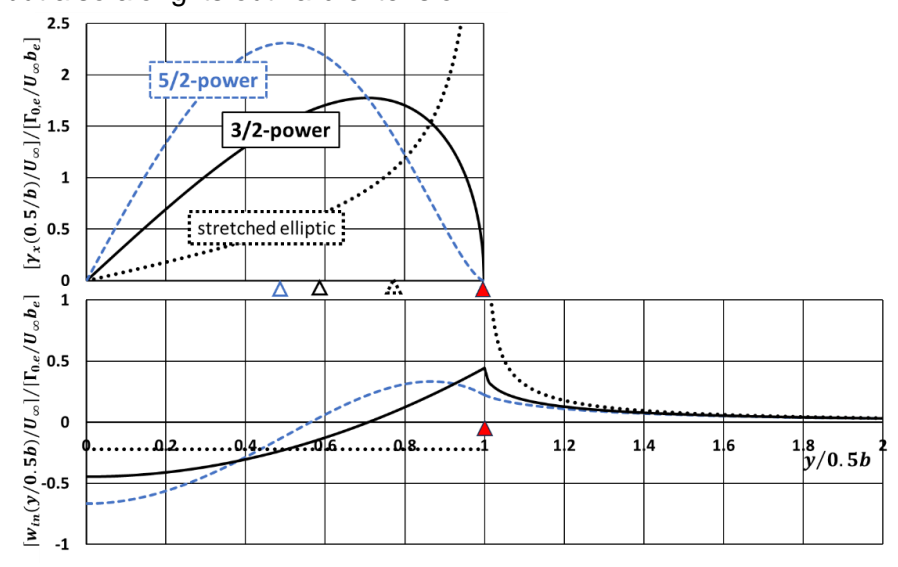


Figure 29 – Comparison of vortex distributions and upwash distributions induced by elliptic and two bell-shaped circulation distributions, see Table 11. Note that the dimensionless spanwise coordinate, for these wings of equal span b, is chosen as  $\eta = y/b$ , with  $\sigma = b/b_e = 1.5$ . The red triangle denotes the location of the wing tip, the open triangles denote the location of COV, the center of the vortex distribution.

Figure 29 shows that the upwash is (negative-)constant along the span; quadratic, partly negative, partly positive; and quartic, partly negative, partly positive, for the elliptic, 3/2-power and 5/2-power distributions. The latter two are bell-shaped circulation distributions. For all three distributions, along the extension of the lifting line, the upwash tends to zero quite quickly.

For the stretched-elliptic distribution the upwash distribution is discontinuous, as well as singular at the wing tip, when approaching the tip along the extension from outside. For the 3/2-power distribution, for which at the wing tip the vortex distribution is zero, but its derivative is infinite and discontinuous, the upwash distribution is continuous, but its derivative is discontinuous across  $|\eta|=1$ . For the 5/2-power distribution for which at the wing tip the vortex distribution is zero in function value and in its first derivative, the upwash distribution is continuous in function value and in its first derivative, resulting in a relatively smooth upwash distribution.

Remarkably, the upwash distribution presented by Bowers et al. [6] (Figure 1b, page 2) for the 3/2-power bell-shaped circulation distribution is quite different near the wing tip for  $|\eta| > 1$ . As also stated in their text, the upwash distribution is not only continuous in function value, but also in its first derivative, which is not the case in our analysis. Unfortunately for  $|\eta| > 1$  a formula for the upwash distribution has not been provided in their report.

In the context of lifting-line theory, vortex wake roll-up is approximated by converting it to a 2D time-dependent problem, in which the evolution is followed of the cross-section of a double-infinite,  $x \in (-\infty, \infty)$ , wake vortex sheet of constant cross-section, with  $t \propto b/U_{\infty}$ . At each time step this results in a 2D flow field (v,w) in the plane of the cross-section The initial condition of the cross-section of the vortex sheet is the projection of the wing trailing edge on the cross-flow plane perpendicular to the x-axis. At the next time step the cross-section of the wake vortex sheet is convected, within the cross-sectional plane, with the local velocity induced by the 2D wake vortex sheet. This yields the updated shape of the cross-section of the wake vortex sheet. The vortex distribution is convected as an invariant with the velocity field. Next the velocity field induced by the new shape of the wake vortex sheet is computed, the vortex sheet and vortex distribution are convected with the flow to their next position, etc. The method [33], [34] used to compute the velocity field induced by the wake-vortex sheet is a second-order panel method that employs a curvature-adaptive discretization scheme for 2D time-dependent vortex sheets. The segmented vortex sheets include single and double-branched discrete vortices that represent tightly rolled-up parts of the vortex sheets.

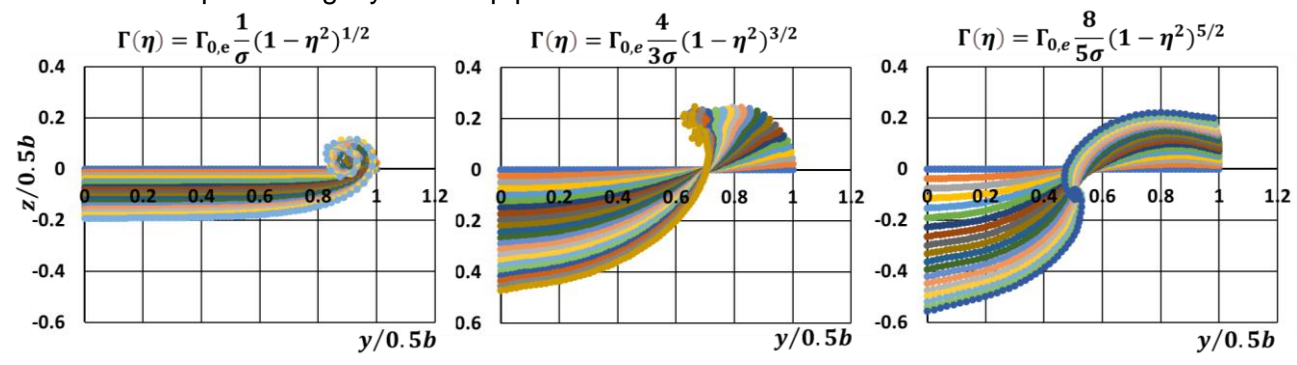


Figure 30 - Computed roll-up of starboard side of vortex wake for elliptic circulation distribution (left), 3/2-power bell-shaped distribution (middle) and 5/2-power bell-shaped distribution of circulation (right). Amplitude distributions warrants equal lift and span. Here  $\sigma = b/b_e = 1.5$ . The time step is kept constant.

Figure 30- left shows results for the wake roll-up for the elliptic distribution of circulation. Since the velocity field is singular and discontinuous at the wing tip, see Figure 29, at the tip the wake rolls up instantaneously at  $t=0^+$ . For that problem Kaden [35] developed a similarity solution, that can be, or should be used, as initial de-singularised solution for the rolled-up vortex-wake spiral. Figure 30-left shows that for the elliptic circulation distribution, just one single-branch spiral wake-vortex evolves, located just outboard of the COV of the vortex distribution. As time progresses, more and more of the vortex distribution is convected into the spiral vortex core, which ultimately has circulation equal to  $\Gamma_{0,e}/\sigma$  and ends up at the location of the COV of the initial vortex sheet:  $\eta_{COV} = y_{COV}/0.5b = \pi/4 \approx 0.785$ .

Figure 30-middle gives the initial evolution for the 3/2-power bell-shaped circulation distribution. For this case at the wing tip the initial flow field is continuous, see Figure 29, with a weaker singularity

than for the elliptic circulation distribution. This is evident in the vortex sheet remaining smooth at the wing tip, i.e., no single-branched spiral-type of roll-up. For this case, the vortex distribution, e.g., see Figure 29, has a plateau region in the vortex distribution of maximum strength, around  $\eta = y_{COV}/0.5b \approx 0.7$ . At this spanwise location the vortex sheet appears to feature a Kelvin-Helmholtz type of instability that results in two double-branched centers of roll-up, which rotate around  $\eta \approx 0.7$ . The COV for this vortex distribution is at  $\eta = y_{COV}/0.5b = 3\pi/16 = 0.59$ , which, compared to the elliptic distribution, is further inboard.

Figure 30-right presents the initial evolution of the roll-up of the wake-vortex sheet for the 5/2-power bell-shaped circulation distribution. For this case Figure 29 shows that at the wing tip the initial flow field is slope-continuous, with a singularity that is even weaker than for the 3/2-power bell-shaped circulation distribution. The vortex sheet remains smooth in the wing-tip region, with no tendency to roll-up. However, for this case the strength of the vortex distribution peaks near the mid-semi-span location, where a center of roll-up forms as a double-branched vortex, which ultimately collects all vorticity of the starboard side of the vortex sheet. The COV for this vortex distribution is, not surprisingly, at  $\eta = y_{COV}/0.5b = 5\pi/32 = 0.49$ .

Bembrekar et al. [36] analysed a constant-airfoil-section (NACA0012) wing of modest AR = 6.6667,  $c_t/c_r$  = 0.2 and sweep angle  $\Lambda$  = 24deg. Similarly to Bowers [6], see section 4 above, the spanwise distribution of geometric twist was constructed such that the distribution of section-circulation is bell-shaped: i.e., a 3/2-power distribution. A Vortex-Latice-Method was used to compute the wing-surface-pressure distribution, lift and induced-drag. The roll-up of the wake-vortex-sheet of this wing is presented up to about 8 chord lengths behind the wing. This result illustrates the gradual development of a center of roll-up at about 2/3 semi-span, which is in reasonable agreement with the corresponding present result in Figure 30.

Hammer & Garmann [37], [38] carried out RaNS computations for a Prandtl-D wing, see section 4 above, with an aspect-ratio of 15.5 and slightly rounded wing tips. The distribution of the geometric twist ([37], Figure 3) is very similar to the distribution computed in the present study, see Figure 8, as is the 3/2-power bell-shaped distribution of the section-circulation. Contours of the vortical wake are shown in two crossflow-planes, i.e., at  $0.5\bar{c}$  and  $2.82\bar{c}$  downstream of the wing. At the design angle-of-attack of 8 deg, this part of the wake does not appear to feature any roll-up of the wake. However, at off-design angles-of-attack a tip-vortex structure develops rapidly, but a mid-semi-span double-branched vortex does not appear.

## 7 Concluding Remarks

- 1) The application of Prandtl's lifting-line theory, for the incompressible, inviscid, irrotational, steady flow about thin, mildly-cambered, high-aspect-ratio, non-swept wings, has brought much insight in the aerodynamic performance associated with bell-shaped distributions of section-circulation.
- 2) In the optimisation, the use of the inverted Biot-Savart law on the relation between vortex distribution and upwash distribution facilitates the direct determination of the vortex distribution and therewith the circulation distribution, required to achieve the minimal induced drag subject to various structure-related constraints.
- 3) The solution of four analysis/design problems has been pursued of minimisation of induced drag, subject to:
  - (i) prescribed lift and span;
  - (ii) prescribed lift and span-integrated section-bending-moment;
  - (iii) prescribed lift and root-bending moment (equal to span-integrated section-shear-force), and;
  - (iv) prescribed lift, root-bending-moment and span-integrated section-bending-moment.
- 4) For these cases detailed expressions have been derived for circulation distribution and distribution of upwash along the lifting line and its outward extension. Furthermore, expressions have been derived for the span of the wing (for cases (ii), (iii) and (iv)), overall lift, drag, span-integrated section-bending-moment, root-bending-moment and yawing-moment, as well as location of the center of the vortex distribution (COV). The latter is relevant for vortex-wake roll-up.
- 5) The elliptic distribution of the circulation  $\sqrt{1-\eta^2}$  is the classical solution of the first minimisation problem. The solution of the three further minimisation problems brings to light four bell-shaped

distributions of the section circulation:

 $(1-\eta^2)^{3/2}$ : (i)

(ii) 
$$\sqrt{1-\eta^2} - \eta^2 \ln \frac{1+\sqrt{1-\eta^2}}{|\eta|}$$

$$\begin{split} \text{(ii)} & \qquad \sqrt{1-\eta^2} - \eta^2 \ln \frac{1+\sqrt{1-\eta^2}}{|\eta|}; \\ \text{(iii)} & \qquad \frac{1}{2} \bigg\{ \sqrt{1-\eta^2} - \eta^2 \ln \frac{1+\sqrt{1-\eta^2}}{|\eta|} \bigg\} - \frac{1}{3} (1-\eta^2)^{3/2} \text{ and}; \end{split}$$

(iv) 
$$(1-\eta^2)^{5/2}$$

These four distributions have zero function value and zero first derivative at the wing tip. The last two distributions have in addition zero second derivative of the circulation distribution at the tip. This has a large effect on the induced upwash distribution, as well as vortex-wake roll-up.

- 6) The prescribed span-integrated section-bending-moment and root-bending moment are expressed as a factor ( $\lambda$  and  $\tau$ , respectively) times their value for a wing with elliptic circulation distribution and identical lift. In literature the factor is taken to be unity. In the present study the factor is arbitrary and its value is shown to have a significant effect on the outcome of the optimization: an increase in the factor results in a decrease of the minimum induced drag. During wing design, this facilitates a trade-off between aerodynamic performance and structural weight.
- 7) Successful verification of the methodology has been achieved by application of the developed expressions to cases considered in literature by Prandtl, Munk, Jones, Nickel and Klein & Viswanathan. Furthermore, the present methodology has been applied with success to the Prandtl-D(rag) wing of Bowers et al. [6], a design based on Prandtl's  $(1 - \eta^2)^{3/2}$  bell-shaped circulation distribution.
- 8) The present lifting-line methodology has been applied, with success, to the analysis of the aerodynamic performance of the wing planform of the robotic bird Robird;
- 9) For all circulation distributions the corresponding upwash distributions along the lifting line and along its outward extensions have been obtained in closed form. Results for the initial roll-up of the vortex wake of wings with a bell-shaped distribution of the circulation have been obtained.
- 10) The observation in Figure 1 (j) of the wake downstream of the trailing-edge of the wing of the model of the B747-8 in our wind tunnel triggered the present study. Though the section-circulation distribution of the wing (AR = 8.5) is not known, it is hypothesized that the location of the tuft  $(v/0.5b \approx 0.8)$  corresponds with the change in sign of the upwash distribution typical for a bellshaped distribution of the section-circulation.

### **Contact Author Email Address**

Contact author: Harry Hoeijmakers. Mail to: H.W.M.Hoeijmakers@gmail.com

## **Copyright Statement**

The authors confirm that they, and/or their company or organization, hold copyright on all of the original material included in this paper. The authors also confirm that they have obtained permission, from the copyright holder of any third-party material included in this paper, to publish it as part of their paper. The authors confirm that they give permission, or have obtained permission from the copyright holder of this paper, for the publication and distribution of this paper as part of the ICAS proceedings or as individual off-prints from the proceedings.

# **Acknowledgements**

The authors acknowledge the support of Walter Lette and Elise Leusink of the technical staff of Engineering Fluid Dynamics in accomplishing the experiments with the 747-8 model aircraft.

#### References

- 1. Lilienthal O. Der Vogelflug als Grundlage der Fliegerkunst. Series Klassische Texte der Wissenschaft. Springer Spektrum, 2010. ISBN 978-3-642-41811-2.
- 2. Horten R and Selinger P. Nurflügel: Die Geschichte der Horten-Flugzeuge 1933-1960. Weishaupt Verlag; Graz, Austria; 1982. Translation in English, see next reference.
- 3. Horten R, Selinger P and Scott J (translator). Nurflügel: the Story of Horten Flying Wings 1933 1960; Weishaupt Verlag; Graz, Austria; 1985. Note: Anhang Zur Theorie des Nurflügelflugzeugs, pp. 230-239.
- 4. Dobrenz T, Spadoni A and Jorgensen M. Aviation archaeology of the Horten 229 v3 aircraft. *Proceedings* 10th AIAA Aviation, Technology, Integration and Operations (ATIO) Conference, September 13-15, 2010,

- Fort Worth, TX, USA. AIAA Paper 2010-9214, 9 pages. https://www.reddit.com/r/MachinePorn/comments/1b0ikq/the\_horten\_ho229\_flying\_wing\_fighter\_first\_flown/
- 5. Chong T. *Flying Wings & Radical Things. Northrop's Secret Aerospace Projects & Concepts* 1939-1994. Speciality Press, Forest Lake, Mn, USA, 2016. ISBN 978-1-58007-229-8.
- 6. Bowers AH, Murillo OJ, Jensen R, Eslinger B and Gelzer Ch. *On Wings of the minimum induced drag: Spanload implications for aircraft and birds*. NASA/TP-2016-219072, 2016, 18 pages.
- 7. Northern Gannet. <a href="https://en.wikipedia.org/wiki/Northern gannet">https://en.wikipedia.org/wiki/Northern gannet</a>. June 3, 2024.
- 8. Folkertsma GA, Straatman W, Nijenhuis N, Venner CH and Stramigioli S. Robird: a robotic bird of prey. *IEEE Robotics and Automation Magazine*, Vol. 24, No. 3, 2017, pp. 22–29. https://doi.org/10.1109/MRA.2016.2636368.
- Hoeijmakers HWM, Groot Koerkamp LH, de Santana LD, Venner CH, Stramigioli S, Mulder JL, Brentjes A, Gijsman F and Hartman SA. Investigation of flapping-flight aerodynamics of a robotic bird. *Proceedings* 33<sup>rd</sup> Congress ICAS 2022, Stockholm, Sweden September 4 - 9, 2022. Paper ICAS2022-0653, 26 pages.
- 10.AeroVironment Inc. 1986.
- 11.van Dam CP. Induced-drag characteristics of crescent-moon shaped wings. *Journal of Aircraft*, Vol. 24, No. 2, pp 115-119, 1987.
- 12.van Dam CP, Vijgen PMHW and Holmes BJ. Experimental investigation on the effect of crescent planform on lift and drag. *Journal of Aircraft*, Vol. 28, No. 11, pp 713-720, 1991.
- 13.de Santana LD, Sanders MP, Venner CH, and Hoeijmakers HWM. The UTwente aeroacoustics wind tunnel upgrade. *AIAA AVIATION Forum*, 2018 *AIAA/CEAS Aeroacoustics Conference*, Atlanta, Georgia, USA, AIAA Paper 2018-3136, 12 pages, 2018.
- 14. Prandtl L. Tragflügeltheorie I und II. Nachrichten der Gesellschaft der Wissenschaften zu Göttingen, Mathematisch-physikalische Klasse, I: S. 151-177, 1918; II: S. 107-137, 1919. See also Tollmien W, Schlichting H and Görtler H. Ludwig Prandtl Gesammelte Abhandlungen zur angewandten Mechanik, Hydro- und Aerodynamik," Erster Teil, I: pp 322-345; II: pp 346-372, Springer Verlag Berlin, GmbH, 1961. Also, in Prandtl L and Betz A. Vier Abhandlungen zur Hydrodynamik und Aerodynamik. Im Selbstverlag des Kaiser Wilhelm-Institut für Strömungsforschung. Göttingen, 1927. Reproduced in Dillmann A. Göttinger Klassiker der Strömungsmechanik, Bd 3. Universitätsverlag Göttingen, 2010.
  - See also: Prandtl L. Application of modern hydrodynamics to aeronautics. NACA Report No. 116, 1923. Munk MM. The minimum induced drag of aerofoils. NACA Report 121, 1923.
- 15. Prandtl L. Über Tragflügeltheorie kleinsten induzierten Widerstandes, Zeitschrift für Flugtechnik und Motorluftschiffahrt, Vol. 24, pp 305-306, 1933. See also Tollmein W, Schlichting H and Görtler H. Ludwig Prandtl Gesammelte Abhandlungen zur angewandten Mechanik, Hydro- und Aerodynamik. Erster Teil, pp 556-561, Springer Verlag Berlin, GmbH, 1961. For translation in English, see [16].
- 16. Hunsaker DF and Phillips WF. Ludwig Prandtl's 1933 paper concerning wings for minimum induced drag, translation and commentary. *AIAA Scitech 2020 Forum*, 6-10 January 2020, Orlando, FL, USA. Paper AIAA2020-0644, 2020.
- 17. Jones RT. The spanwise distribution of lift for minimum induced drag of wings having a given lift and a given bending moment. NACA-TN-2249, 1950.
- 18. Munk MM. Elements of the wing section theory and of the wing theory. NACA Report 191, 1924.
- 19. Klein A and Viswanathan S. Minimum induced drag of wings with given lift and root-bending moment. *Zeitschrift für angewandte Mathematik und Physik, ZAMP,* Vol. 24, No. 6, pp 886-892, 1973.
- 20. Nickel K. Lösung eines speziellen Minimumproblems. Mathematisch Zeitschrift, Vol. 53, pp 21-52, 1950.
- 21. Nickel K. Lösung eines Minimumproblems der Tragflügeltheorie. *Zeitschrift für angewandte Mathematik und Mechanik*, Vol. 31, Nr. 8, pp 72-77, 1952.
- 22. Ashley H and Landahl MT. *Aerodynamics of wings and bodies*. Addison-Wesley Publishing Company. Reading, Ma, USA. 1965. Also, Dover Publications, Inc, NY, USA, 1985.
- 23. Drela M. Flight vehicle aerodynamics. The MIT Press, Cambridge, Ma, USA. 2014.
- 24. Klein A and Viswanathan S. Approximate solution for minimum induced drag of wings with a given structural weight. *Journal of Aircraft*, Vol. 12, No. 2, p. 124-126, 1975. See also Errata of article. *Journal of Aircraft*, Vol. 12, No. 9, p. 756, 1975.
- 25. Löbert G. Spanwise lift distribution of forward- and aft-swept wings in comparison to optimum distribution form. *Journal of Aircraft*, Vol. 18, No. 6, pp. 496-498, 1981.
- 26.McGeer T. Wing design for minimum drag with practical constraints. *Journal of Aircraft*, Vol. 21, No. 11, pp. 879-886, 1984.
- 27. Iglesias S and Mason WH. Optimum spanloads incorporating wing structural weight. 1st AIAA Aircraft Technology, Integration, and Operations Forum, Los Angeles, CA, USA. AIAA Paper 2001-5234, 2001.
- 28.Bragado-Aldana E and Riaz A. Assessment of structurally-constrained spanloads for span-extended wing design. *AIAA SciTech Forum*, Orlando, FL, USA, AIAA Paper 2024-0004, 20 pages, 2024.
- 29. Anderson Jr. JD. Fundamentals of aerodynamics. 6th edition, McGraw-Hill Education, 2017.
- 30. Pate DJ and German BJ. Lift distributions for minimum induced drag with generalized bending moment constraints. *Journal of Aircraft*, Vol. 50, No. 3, pp. 936-946, 2013.
- 31.Zelenka B, Olson ED and Liu X. Prandtl-D qualitative and quantitative wind tunnel tests. AIAA SciTech

- Forum, San Diego, CA, USA, AIAA Paper 2022-0545, 10 pages, 2022.
- 32.Groot Koerkamp LH, Hoeijmakers HWM, Venner CH and Stramigioli S. Aerodynamics flapping robotic bird using unsteady lifting-line method. *AIAA AVIATION Forum*, 2023 *Applied Aerodynamics Conference*, San Diego, California, USA. AIAA Paper 2023-4527, 37 pages, 2023.
- 33. Hoeijmakers HWM and Vaatstra W. A higher-order panel method applied to vortex sheet roll up. *AIAA Journal*, Vol. 21, No. 4, pp 516-523, 1983.
- 34. Hoeijmakers HWM. *Computational aerodynamics of ordered vortex flows*. PhD thesis Delft University of Technology, Delft, The Netherlands, 200 pages, May 30, 1989.
- 35. Kaden H. Aufwicklung einer unstabielen Unstetigkeitsfläche. Ing. Arch, Vol. 2, pp 140-168, 1931.
- 36.Brembrekar V, Rasane A, Jadhav A, Vaishnav O and Mirdude S. Design of a wing with bell-shaped spanload using VLM Method. *International Journal of Engineering Trends and Technology* (IJETT), Vol. 59, No. 4, 2018, pp.182-185.
- 37. Hammer PR and Garmann DJ. Simulations of a bell-shaped spanloaded swept wing. *AIAA SciTech Forum*, National Harbor, MD, USA, AIAA Paper 2023-1979, 20 pages, 2023.
- 38. Hammer PR and Garmann DJ. Wake structures of the Prandtl-D. *AIAA AVIATION 2023 Forum,* San Diego, CA, USA, AIAA Paper 2023-4003, 21 pages, 2023.

## **APPENDIX A: Aerodynamic Performance Indicators**

Quantities are made dimensionless using:

Free-stream dynamic pressure  $\frac{1}{2}\rho_{\infty}U_{\infty}^2$ 

 $U_{\infty}$ : Free-stream velocity

Free-stream density  $\rho_{\infty}$ :

and quantities of the wing with elliptic circulation distribution with prescribed span  $b_e$  and lift  $L_e$ :

Span of wing with elliptic loading and lift  $L_e$ 

Amplitude elliptic circulation distribution  $\Gamma(y) = \Gamma_{0,e} (1 - (y/0.5b_e)^2)^{1/2}$  $\Gamma_{0.e}$ 

## Section forces and moments:

1.1. Section lift force 
$$\ell(y) = \rho_{\infty} U_{\infty} \Gamma(y)$$

$$\ell(y) = [q_{\infty}b_e][\frac{\Gamma_{0,e}}{U_{\infty}b_e}]2\frac{\Gamma(y)}{\Gamma_{0,e}}$$

$$d(y) = -[q_{\infty}b_e]\left[\left(\frac{\Gamma_{0,e}}{U_{\infty}b_e}\right)^2\right] 2 \frac{w_{in}(y)/U_{\infty}}{\Gamma_{0,e}/U_{\infty}b_e} \frac{\Gamma(y)}{\Gamma_{0,e}}$$

1.2. Section drag force  $d(y) = -\rho_{\infty} w_{in}(y) \Gamma(y)$   $d(y) = -[q_{\infty}b_e] \left[ \left( \frac{\Gamma_{0,e}}{U_{\infty}b_e} \right)^2 \right] 2 \frac{w_{in}(y)/U_{\infty}}{\Gamma_{0,e}/U_{\infty}b_e} \frac{\Gamma(y)}{\Gamma_{0,e}}$ 1.3. Section contribution starboard-side root-bending-moment  $m_{\chi}(y) = y\ell(y)$ 

$$m_x(y) = [q_{\infty}b_e^2] \left[\frac{\Gamma_{0,e}}{U_{\infty}b_e}\right] \frac{\Gamma(y)}{\Gamma_{0,e}} \frac{y}{0.5b_e}$$

1.4. Section contribution starboard-side section-bending-moment  $m_{x,2}(y) = \frac{1}{2}y^2\ell(y)$ 

$$m_{x,2}(y) = [q_{\infty}b_e^3] \left[\frac{\Gamma_{0,e}}{U_{\infty}b_e}\right] \frac{1}{4} \frac{\Gamma(y)}{\Gamma_{0,e}} \left(\frac{y}{0.5b_e}\right)^2$$

$$\begin{split} m_{x,2}(y) &= [q_{\infty}b_e^3] [\frac{\Gamma_{0,e}}{l_{\infty}b_e}] \frac{1}{4} \frac{\Gamma(y)}{\Gamma_{0,e}} (\frac{y}{0.5b_e})^2 \\ \text{1.5. Section contribution starboard-side section-yawing-moment } m_z(y) &= -yd(y) \\ m_z(y) &= [q_{\infty}b_e^2] \left[ (\frac{\Gamma_{0,e}}{l_{\infty}b_e})^2 \right] \frac{w_{in}(y)/l_{\infty}}{\Gamma_{0,e}/l_{\infty}b_e} \frac{\Gamma(y)}{\Gamma_{0,e}} \frac{y}{0.5b_e} \end{split}$$

$$m_z(y) = [q_{\infty}b_e^2] \left[ \left( \frac{\Gamma_{0,e}}{U_{\infty}b_e} \right)^2 \right] \frac{w_{in}(y)/U_{\infty}}{\Gamma_{0,e}/U_{\infty}b_e} \frac{\Gamma(y)}{\Gamma_{0,e}} \frac{y}{0.5b_e}$$

Full-span, or semi-span-integrated overall forces and moments, with  $b/b_e$  the dimensionless span: 2.1. Full-span lift force  $L = \int_{-b/2}^{b/2} \ell(y) dy$   $L = [q_{\infty}b_e^2] [\frac{\Gamma_{0,e}}{U_{\infty}b_e}] \int_0^{b/b_e} 2 \frac{\Gamma(y)}{\Gamma_{0,e}} d\frac{y}{0.5b_e}$ 

$$L = [q_{\infty}b_e^2][\frac{\Gamma_{0,e}}{U_{\infty}b_e}] \int_0^{b/b_e} 2\frac{\Gamma(y)}{\Gamma_{0,e}} d\frac{y}{0.5b_e}$$

2.2. Full-span drag force 
$$D = \int_{-b/2}^{b/2} d(y) dy$$

$$D = -[q_{\infty}b_e^2] \left[ \left( \frac{\Gamma_{0,e}}{U_{\infty}b_e} \right)^2 \right] \int_0^{b/b_e} 2 \frac{w_{in}(y)/U_{\infty}}{\Gamma_{0,e}/U_{\infty}b_e} \frac{\Gamma(y)}{\Gamma_{0,e}} d\frac{y}{0.5b_e}$$
2.3. Starboard-side root-bending-moment  $M_x = \int_0^{b/2} m_x(y) dy$ 

$$M_{x} = [q_{\infty}b_{e}^{3}] \left[\frac{\Gamma_{0,e}}{U_{\infty}b_{e}}\right] \frac{1}{2} \int_{0}^{b/b_{e}} \frac{\Gamma(y)}{\Gamma_{0,e}} \frac{y}{0.5b_{e}} d\frac{y}{0.5b_{e}}$$

 $M_{x} = [q_{\infty}b_{e}^{3}][\frac{\Gamma_{0,e}}{U_{\infty}b_{e}}]^{\frac{1}{2}} \int_{0}^{b/b_{e}} \frac{\Gamma(y)}{\Gamma_{0,e}} \frac{y}{0.5b_{e}} d\frac{y}{0.5b_{e}}$ 2.4 Starboard-side integrated-bending-moment  $M_{x,2} = \int_{0}^{b/2} m_{x}(y) dy$   $M_{x,2} = [q_{\infty}b_{e}^{4}][\frac{\Gamma_{0,e}}{U_{\infty}b_{e}}]^{\frac{1}{2}} \int_{0}^{b/b_{e}} \frac{1}{4} \frac{\Gamma(y)}{\Gamma_{0,e}} (\frac{y}{0.5b_{e}})^{2} d\frac{y}{0.5b_{e}}$ 

$$M_{x,2} = [q_{\infty}b_e^4][\frac{\Gamma_{0,e}}{U_{\infty}b_e}]\frac{1}{2}\int_0^{b/b_e}\frac{1}{4}\,\frac{\Gamma(y)}{\Gamma_{0,e}}(\frac{y}{0.5b_e})^2d\,\frac{y}{0.5b_e}$$

2.5 Starboard-side integrated-yawing-moment 
$$M_z = \int_0^{b/2} m_z(y) dy$$

$$M_z = \left[q_\infty b_e^3\right] \left[\left(\frac{\Gamma_{0,e}}{U_\infty b_e}\right)^2\right] \frac{1}{2} \int_0^{b/b_e} \frac{w_{in}(y)/U_\infty}{\Gamma_{0,e}/U_\infty b_e} \frac{\Gamma(y)}{\Gamma_{0,e}} \frac{y}{0.5b_e} d\frac{y}{0.5b_e}$$
2.6 Starboard-side center of vortex distribution

$$y_{COV} \equiv \int_0^{b/2} \gamma_x(y) y dy / \int_0^{b/2} \gamma_x(y) dy = \frac{1}{\Gamma(0)} \int_0^{b/2} \Gamma(y) dy = \frac{0.5b_e}{\Gamma(0)/\Gamma_{0,e}} \int_0^{b/b_e} \frac{\Gamma(y)}{\Gamma_{0,e}} d\frac{y}{0.5b_e}.$$

## **Appendix B: Variational Formulation**

This Appendix considers the variational expressions of lift L, induced-drag D, root-bending-moment  $M_{\gamma}$ and span-integrated section-bending-moment  $M_{x,2}$ . The analysis is based on Prandtl and Munk [14], Prandtl and Betz [15], Nickel [21], Jones [17], Klein & Viswanathan [19], [24], Drela [23], ...

## Lifting-line Theory

The lifting line geometry considered consists of a discrete, y-symmetric, line-vortex, circulation  $\Gamma(y)$ , with attached to it the downstream flat wake-vortex-sheet of strength  $\gamma_x(x,y) = -d\Gamma/dy$ , in the plane z =0, which extends from the lifting line to infinity downstream. This vortex system defines the velocity potential  $\varphi(x,y,z)$  and induced velocity field  $\vec{u}(x,y,z) = \vec{\nabla}\varphi$  in the whole 3D space. In the present study the lifting line is taken as the straight line x = 0,  $|y| \le b/2$ , z = 0.

 $\Gamma(y)$  is the distribution of the circulation:  $\Gamma(y) = \varphi(0, y, 0^+) - \varphi(0, y, 0^-) = \Delta \varphi(y)$  in terms of the perturbation velocity potential, with  $\vec{u}(0, y, z) = \vec{\nabla} \varphi$  in the (y, z)-plane. The perturbation velocity potential satisfies Laplace's equation  $\vec{\nabla} \cdot (\vec{\nabla} \varphi) = 0$ .

The lift, induced drag, root-bending-moment and the span-integrated section-bending-moment follow from Table 1 and Appendix A. The lift of the wing is expressed as

$$L = \rho_{\infty} U_{\infty} \int_{-h/2}^{h/2} \Gamma(y) dy. \tag{B.1}$$

The induced-drag is given by 
$$D = -\rho_{\infty} \int_{-b/2}^{b/2} \Gamma(y) dy, \tag{B.1}$$

$$D = -\rho_{\infty} \int_{-b/2}^{b/2} w_{in}(y) \Gamma(y) dy, \tag{B.2}$$

with the upwash distribution 
$$w_{in}(|y| < b/2)$$
 along the lifting line expressed as  $w_{in}(|y| < b/2) = w(0, y, 0) = \frac{1}{4\pi} \text{CPV} \int_{-b/2}^{b/2} \gamma_x(y') \frac{dy'}{y-y'}$ . (B3) The distribution of the upwash  $w_{in}(y)$  along the lifting-line is continuous over the wake-vortex-sheet:

 $w_{in}(y) = \frac{\partial \varphi}{\partial z}(0, y, 0^+) = \frac{\partial \varphi}{\partial z}(0, y, 0^-).$ (B.4)

The root-bending-moment 
$$M_x$$
, see Table 1 and Appendix A, equals: 
$$M_x = \rho_\infty U_\infty \int_0^{b/2} \Gamma(y) y dy = \frac{1}{2} \rho_\infty U_\infty \int_{-b/2}^{b/2} \Gamma(y) |y| dy,$$
 while the span-integrated section-bending-moment follows from 
$$(B.5)$$

$$M_{x,2} = \frac{1}{2} \rho_{\infty} U_{\infty} \int_{0}^{b/2} \Gamma(y) y^{2} dy = \frac{1}{4} \rho_{\infty} U_{\infty} \int_{-b/2}^{b/2} \Gamma(y) y^{2} dy$$
 (B.6)

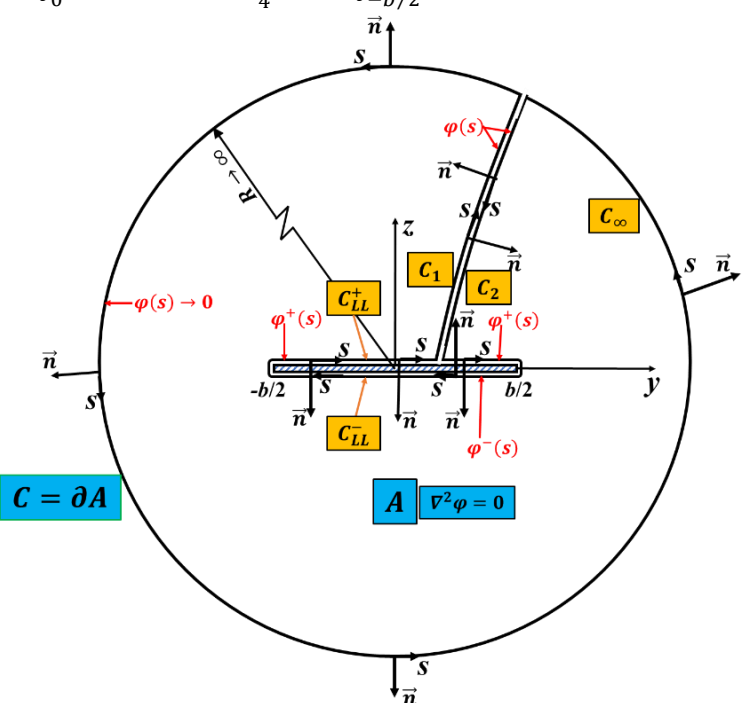


Figure B.1 – Trefftz-plane at  $x \to \infty$ . Area A is in plane x = constant, with  $C = \partial A$  closed contour forming its boundary, which wraps around cross-section of wake-vortex-sheet ( $\mathcal{C}_{LL}^+,\mathcal{C}_{LL}^-$ ). It is connected to contour  $\mathcal{C}_{\infty}$  in far-field by cut consisting of parallel, closely-spaced, curves  $C_1$  and  $C_2$ .  $\vec{n}$  is unit normal on C pointing out of A, s denotes coordinate along contour C. Within A perturbation potential  $\varphi(y,z)$  is continuous and satisfies

Laplace's equation  $\nabla^2 \varphi = 0$ . Distribution of circulation lifting line:  $\Gamma(s) = \Delta \varphi(s) = \varphi^+(s) - \varphi^-(s)$ .

In the further analysis, the expressions for lift, induced-drag, root-bending-moment and span-integrated section-bending-moment are generalised in terms of expressions in the so-called Trefftzplane: the (y, z)-plane at  $x \to \infty$ , see Figure B.1. This yields:

$$L = \rho_{\infty} U_{\infty} \int_{c}^{\Box} \varphi(s) \left| \frac{d\vec{y}}{ds} \right| ds, \text{ with } \vec{y}(s) = y(s) \vec{e}_{y} + z(s) \vec{e}_{z}, \tag{B.7}$$

$$M_{x} = \frac{1}{2} \rho_{\infty} U_{\infty} \int_{C}^{\square} \varphi(s) |y(s)| \left| \frac{d\vec{y}}{ds} \right| ds \text{ and}$$
(B.8)

$$M_{x,2} = \frac{1}{4} \rho_{\infty} U_{\infty} \int_{C}^{\square} \varphi(s) y^{2}(s) \left| \frac{d\vec{y}}{ds} \right| ds. \tag{B.9}$$

In this notation, the contributions of the integration along  $C_{LL}^+$  and  $C_{LL}^-$  combine to

$$L_{LL} = \rho_{\infty} U_{\infty} \int_{C_{LL}}^{\square} \Delta \varphi(s) dC, \text{ with } dC = \left| \frac{d\vec{y}}{ds} \right| ds, \tag{B.10}$$

$$M_{x,LL} = \frac{1}{2} \rho_{\infty} U_{\infty} \int_{C_{LL}}^{\square} \Delta \varphi(s) |y(s)| d\mathcal{C}$$
 and (B.11)

$$M_{x,2,LL} = \frac{1}{4} \rho_{\infty} U_{\infty} \int_{C_{LL}}^{\frac{1}{2}} \Delta \varphi(s) y^{2}(s) dC$$
, with  $\Delta \varphi(s) = \varphi^{+}(s) - \varphi^{-}(s) = \Gamma(s)$ . (B.12)

Furthermore, the contributions of the two sides of the cut,  $C_1$  and  $C_2$ , cancel because  $\varphi(s)$  and  $\vec{y}(s)$ are continuous across the cut. Finally, the contribution of  $C_{\infty}$  equals zero because  $\varphi(s) \to 0$  along  $C_{\infty}$ , the far-field part of the closed contour. Therefore, the results in Eqs. (B.1), (B.5) and (B.6) are indeed equivalent to the results in Eqs. (B.7), (B.8) and (B.9), respectively.

For the induced drag D, given in Eq. (B.2), the distribution of the upwash  $w_{in}(s)$  along the closed contour, as given in Eq. B.4, can be expressed as the normal component of the induced velocity along C in the Trefftz-plane, i.e.,

$$w_{in}(s) = -\frac{1}{2}(\vec{\nabla}\varphi.\vec{n}), \text{ with outward unit normal } \vec{n} = \frac{d\vec{y}}{ds} \times \vec{e}_x.$$
 (B.13)

The factor 0.5 accounts for the upwash velocity induced in the Trefftz-plane  $(x \to \infty)$ , by the infinite wake-vortex-sheet extending from x = 0 to  $x \to \infty$ , to be twice the upwash velocity induced by the semiinfinite wake-vortex-sheet in the plane (x = 0) of the lifting-line. The generalized expression for the induced drag becomes:

$$D = \frac{1}{2} \rho_{\infty} \int_{C}^{\square} \varphi(s) (\vec{\nabla} \varphi \cdot \vec{n}) dC. \tag{B.14}$$

In this notation, the contributions of the integration along  $C_{LL}^+$  and  $C_{LL}^-$  combine to the expression for the induced-drag given in Eq. (B.2).

# Calculus of Variations

In the method of Calculus of Variations, the unknown function  $\varphi(s)$  is perturbed by an infinitesimal perturbation function  $\delta \varphi(s)$ . For the case of the straight lifting-line, considered in detail in the present study, the result for prescribed lift L is:

$$L + \delta L = \rho_{\infty} \int_{-b/2}^{b/2} \Delta \varphi(y) dy + \rho_{\infty} \int_{-b/2}^{b/2} \Delta \delta \varphi(y) dy, \tag{B.15}$$

where  $\delta L = \rho_{\infty} \int_{-b/2}^{b/2} \Delta \delta \varphi(y) dy = \rho_{\infty} \int_{-b/2}^{b/2} \delta \Gamma(y) dy$  should be zero.

For prescribed root-bending-moment 
$$M_x$$
 it follows from Eq. (B.8):  

$$M_x + \delta M_x = \frac{1}{2} \rho_\infty U_\infty \int_{-b/2}^{b/2} |y| \Delta \varphi(y) dy + \frac{1}{2} \rho_\infty U_\infty \int_{-b/2}^{b/2} |y| \Delta \delta \varphi(y) dy, \tag{B.16}$$

where 
$$\delta M_{\chi} = \frac{1}{2} \rho_{\infty} \int_{0}^{b/2} |y| \Delta \delta \varphi(y) dy = \frac{1}{2} \rho_{\infty} \int_{-b/2}^{b/2} |y| \delta \Gamma(y) dy$$
 should be zero. (B.17)

For prescribed span-integrated section-bending-moment  $M_{x,2}$  it follows from Eq. (B.9):

$$M_{x,2} + \delta M_{x,2} = \frac{1}{4} \rho_{\infty} U_{\infty} \int_{-b/2}^{b/2} y^2 \Delta \varphi(y) dy + \frac{1}{4} \rho_{\infty} U_{\infty} \int_{-b/2}^{b/2} y^2 \Delta \delta \varphi(y) dy,$$
 (B.16)

where 
$$\delta M_{x,2} = \frac{1}{4} \rho_{\infty} \int_{-b/2}^{b/2} y^2 \Delta \delta \varphi(y) dy = \frac{1}{4} \rho_{\infty} \int_{-b/2}^{b/2} y^2 \delta \Gamma(y) dy$$
 should be zero. (B.17)

For the induced drag it follows from Eq. (B.14) that:

$$D + \delta D = \frac{1}{2} \rho_{\infty} \int_{C}^{\square} \varphi(s) (\vec{\nabla} \varphi \cdot \vec{n}) dC + \frac{1}{2} \rho_{\infty} \int_{C}^{\square} [\varphi(s) (\vec{\nabla} \delta \varphi \cdot \vec{n}) + \delta \varphi(s) (\vec{\nabla} \varphi \cdot \vec{n})] dC + \frac{1}{2} \rho_{\infty} \int_{C}^{\square} \delta \varphi(s) (\vec{\nabla} \delta \varphi \cdot \vec{n}) dC.$$
(B.18)

If the last integral in the right-hand-side, a second-order term in  $\delta \varphi$ , is neglected, the induced drag

$$\delta D = \frac{1}{2} \rho_{\infty} \int_{\mathcal{C}}^{\square} [\varphi(s) (\vec{\nabla} \delta \varphi \cdot \vec{n}) + \delta \varphi(s) (\vec{\nabla} \varphi \cdot \vec{n})] d\mathcal{C} = 0.$$
(B.19)

Applying the Divergence Theorem of Gauss for the 2D area A with boundary  $C = \partial A$ :

$$\iint_{A} \vec{\nabla} \cdot \vec{F} dA = \int_{C=\partial A} \vec{F} \cdot \vec{n} dC, \tag{B-20}$$

to the integral with the first part of the integrand in Eq. (B.19), yields, with  $\vec{F} = \varphi \vec{\nabla} \delta \varphi$ :

$$\int_{C}^{\square} \varphi(\vec{\nabla}\delta\varphi.\vec{n})dC = \iint_{A}^{\square} [\vec{\nabla}\varphi.\vec{\nabla}\delta\varphi + \varphi\nabla^{2}\delta\varphi]dA, \text{ resulting with } \nabla^{2}\delta\varphi = 0 \in A \text{ in}$$

$$= \iint_{A}^{\square} (\vec{\nabla}\varphi.\vec{\nabla}\delta\varphi)dA. \tag{B.21}$$

The integral with the second part of the integrand in Eq. (B.19) yields, with  $\vec{F} = \delta \varphi \vec{\nabla} \varphi$ :

$$\int_{C}^{\square} \delta\varphi(\vec{\nabla}\varphi.\vec{n})dC = \iint_{A}^{\square} [\vec{\nabla}\delta\varphi.\vec{\nabla}\varphi + \delta\varphi\nabla^{2}\varphi]dA, \text{ resulting, with } \nabla^{2}\varphi = 0 \in A \text{ in}$$

$$= \iint_{A}^{\square} (\vec{\nabla}\delta\varphi.\vec{\nabla}\varphi)dA. \tag{B.22}$$

This proves that the two contributions in Eq. (B.19) are identical, sometimes referred to as the Munk's Mutual Drag Theorem, see [15]. Using Eqs. (B.21) and B.22) results in the condition for optimality becoming:

$$\delta D = \rho_{\infty} \int_{C}^{\Box} \delta \varphi(\vec{\nabla} \varphi. \vec{n}) dC = 0. \tag{B.23}$$

For the case of the straight lifting-line considered in detail in the present study, upon converting  $\nabla \varphi$ .  $\vec{n}$ into  $w_{in}(y)$ , condition (B.23) becomes:

$$\delta D = -2\rho_{\infty} \int_{-b/2}^{b/2} w_{in}(y) \delta \Gamma dy = 0.$$
(B.24)

Note that in Eq. (B.18) the induced drag D and the neglected higher-order term in  $\delta D$ , using the Divergence Theorem, can be expressed as:

$$D = \iint_A^{\square} |\vec{\nabla}\varphi|^2 dA$$
 and  $\delta D_{h.o.t} = \iint_A^{\square} |\vec{\nabla}\delta\varphi|^2 dA$ , respectively. Both terms are positive.

In summary for the flat, y-symmetric wake-vortex-sheet.

$$\delta D = -2\rho_{\infty} \int_{-b/2}^{b/2} w_{in}(y) \delta \Gamma dy = 0, \text{ subject to:}$$
 (B.25a)

$$\delta D = -2\rho_{\infty} \int_{-b/2}^{b/2} w_{in}(y) \delta \Gamma dy = 0, \text{ subject to:}$$

$$\delta L = \rho_{\infty} \int_{-b/2}^{b/2} \delta \Gamma(y) dy = 0,$$
(B.25a)

$$\delta M_{x} = \frac{1}{2} \rho_{\infty} \int_{-b/2}^{b/2} |y| \delta \Gamma(y) dy = 0,$$
(B.25c)

$$\delta M_{x,2} = \frac{1}{4} \rho_{\infty} \int_{-b/2}^{b/2} y^2 \delta \Gamma(y) dy = 0, \text{ etc.},$$
(B.25d)

Note that the infinitesimally small  $\delta\Gamma(y)$  is arbitrary but for the conditions in Eqs. (B.25b-d). Therefore, condition (B.25a) is satisfied by the upwash distribution  $w_{in}(y)$  specified as

$$w_{in}(y) = a_0 + a_1|y| + a_2y^2 + \cdots,$$
 (B.25e)

for arbitrary constants  $a_0$ ,  $a_1$ ,  $a_2$ , ....

The inverted Biot-Savart relation then provides the corresponding terms in the vortex distribution  $\gamma_x(y)$  that generates the upwash distribution  $w_{in}(y)$  given in Eq. (B.25e). Integrating the relation  $\gamma_x(y) = -d\Gamma/dy$  results in the circulation distribution along the lifting line.

## Formulation in terms of Lagrangian function

An alternative formulation is to force the Lagrangian function  $\mathcal{L}$ , which contains the induced drag D, as well as all constraints, to be stationary. The Lagrangian function  $\mathcal{L}$  is defined as:

$$\mathcal{L}(\Gamma(y), \kappa_0, \kappa_1, \kappa_2, \dots) \equiv D + \kappa_0(L - L_e) + \kappa_1(M_x - \lambda M_{x,e}) + \kappa_2(M_{x,2} - \tau M_{x,2,e}) + \dots, \tag{B.26}$$

with  $\kappa_0$ ,  $\kappa_1$ ,  $\kappa_2$ , ... the so-called Lagrangian multipliers associated with the constraints on lift L, root-bending-moment  $M_x$ , span-integrated section-bending-moment  $M_{x,2}$ , ..., respectively, to be determined as part of the solution.

The solution of the minimisation problem should be stationary with respect to variations in the circulation distribution  $\Gamma(y)$ , i.e.,  $\delta \mathcal{L}$  should be zero. This leads to

$$\delta \mathcal{L} = \delta D + \delta \kappa_0 (L - L_e) + \kappa_0 \delta L + \delta \kappa_1 (M_x - \lambda M_{x,e}) + \kappa_1 \delta M_x + \delta \kappa_2 (M_{x,2} - \tau M_{x,2,e}) + \kappa_2 \delta M_{x,2} \dots = 0.$$
 (B.27a) With the variations given in Eqs. (B.25a-d), it follows:

$$\delta \mathcal{L} = \rho_{\infty} \int_{-b/2}^{b/2} \left[ -2w_{in}(y) + \kappa_{0}U_{\infty} + \frac{1}{2}\kappa_{1}U_{\infty}|y| + \frac{1}{4}\kappa_{2}U_{\infty}y^{2} + \cdots \right] \delta\Gamma(y)dy + \delta\kappa_{0}(L - L_{e}) + \delta\kappa_{1}(M_{x} - \lambda M_{x,e}) + \delta\kappa_{2}(M_{x,2} - \tau M_{x,2,e}) + \cdots = 0.$$
 (B.27b)

Note that the variation of the span b in the upper and lower limits of integration does not contribute in Eq. (B.27b) for  $\delta \mathcal{L}$ .

Therefore, since  $\delta\Gamma$ ,  $\delta\kappa_0$ ,  $\delta\kappa_1$ ,  $\delta\kappa_2$ , ... are arbitrary, we find the system of relations:

$$w_{in}(y) = \frac{1}{2} U_{\infty} \left[ \kappa_0 + \frac{1}{2} \kappa_1 |y| + \frac{1}{4} \kappa_2 y^2 + \dots \right], \text{ for } |y| < b/2,$$
(B.28a)

$$L = L_e: \qquad \rho_{\infty} U_{\infty} \int_{-b/2}^{b/2} \Gamma(y) dy = L_e, \tag{B.28b}$$

$$M_x = \lambda M_{x,e}$$
:  $\rho_\infty U_\infty \int_0^{b/2} |y| \Gamma(y) dy = \lambda M_{x,e}$ , (B.28c)  $M_{x,2} = \tau M_{x,2,e}$ :  $\frac{1}{2} \rho_\infty U_\infty \int_0^{b/2} y^2 \Gamma(y) dy = \tau M_{x,2,e}$ , etc. (B.28d) The relation for the induced upwash distribution  $w_{in}(y)$ , Eq. (B.28a), yields, through the inverted Biot-

$$M_{x,2} = \tau M_{x,2,e}$$
:  $\frac{1}{2} \rho_{\infty} U_{\infty} \int_0^{b/2} y^2 \Gamma(y) dy = \tau M_{x,2,e}$ , etc. (B.28d)

The relation for the induced upwash distribution  $w_{in}(y)$ , Eq. (B.28a), yields, through the inverted Biot-Savart relation the vortex distribution  $\gamma_x(y)$  and subsequently the circulation distribution  $\Gamma(y)$ . These involve the yet unknown Lagrangian multipliers  $\kappa_0$ ,  $\kappa_1$ ,  $\kappa_2$ , ...in a linear manner, i.e.,

$$\Gamma(y) = \kappa_0 \Gamma_0(y) + \kappa_1 \Gamma_1(y) + \kappa_2 \Gamma_2(y) + \cdots ]. \tag{B.28e}$$

Substituting the circulation distribution  $\Gamma(y)$  in the expressions for lift L, root-bending-moment  $M_x$ , spanintegrated section-bending-moment  $M_{x,2}$ , ... in Eqs. (B.28b-d), gives as many linear equations as there are Lagrangian multipliers,  $\kappa_0, \kappa_1, \kappa_2, ...$  involving the prescribed  $L_e, \lambda M_{x,e}, \tau M_{x,2,e}, ...$  as parameters. Furthermore, in these equations, the span b of the wing is an additional variable. Substituting the resulting expressions for  $\kappa_0, \kappa_1, \kappa_2, \ldots$  in the expression for the induced drag D, Eq. (B.2), provides the induced drag as function of  $L_e$ ,  $\lambda M_{x,e}$ ,  $\tau M_{x,2,e}$ , ... and span b, i.e.,

$$D = D(L_e, \lambda M_{x,e}, \tau M_{x,2,e}, ...; b).$$
(B.29)

The minimum induced drag  $D_{opt}(L_e, \lambda M_{x,e}, \tau M_{x,2,e}, ...; b_{opt})$  is found by setting

$$\frac{\partial}{\partial b}D(L_e,\lambda M_{x,e},\tau M_{x,2,e},\ldots;b)=0,$$

 $\frac{\partial}{\partial b}D\big(L_e,\lambda M_{x,e},\tau M_{x,2,e},...;b\big)=0,$  solving for optimal wing-span  $b_{opt}(L_e,\lambda M_{x,e},\tau M_{x,2,e},...)$  and substitution of  $b_{opt}$ in Eq. (B.29) for the induced drag, which provides  $D_{opt}$ .

# APPENDIX C Some Integrals

Integrals over circulation distributions and vortex distributions Integrals over circulation distributions and vortex distributions  $1.1.0 \int_0^1 \frac{d\eta}{\sqrt{1-\eta^2}} = \frac{\pi}{2} \qquad 1.2.0 \int_0^1 \sqrt{1-\eta^2} d\eta = \frac{\pi}{4} \qquad 1.3.0 \int_0^1 (1-\eta^2)^{3/2} d\eta = \frac{3\pi}{16}$   $1.1.1 \int_0^1 \frac{\eta d\eta}{\sqrt{1-\eta^2}} = 1 \qquad 1.2.1 \int_0^1 \eta \sqrt{1-\eta^2} d\eta = \frac{1}{3} \qquad 1.3.1 \int_0^1 \eta (1-\eta^2)^{3/2} d\eta = \frac{1}{5}$   $1.1.2 \int_0^1 \frac{\eta^2 d\eta}{\sqrt{1-\eta^2}} = \frac{\pi}{4} \qquad 1.2.2 \int_0^1 \eta^2 \sqrt{1-\eta^2} d\eta = \frac{\pi}{16} \qquad 1.3.2 \int_0^1 \eta^2 (1-\eta^2)^{3/2} d\eta = \frac{\pi}{32}$   $1.1.3 \int_0^1 \frac{\eta^3 d\eta}{\sqrt{1-\eta^2}} = \frac{2}{3} \qquad 1.2.3 \int_0^1 \eta^3 \sqrt{1-\eta^2} d\eta = \frac{2}{15} \qquad 1.3.3 \int_0^1 \eta^3 (1-\eta^2)^{3/2} d\eta = \frac{2}{35}$   $1.1.4 \int_0^1 \frac{\eta^4 d\eta}{\sqrt{1-\eta^2}} = \frac{3\pi}{16} \qquad 1.2.4 \int_0^1 \eta^4 \sqrt{1-\eta^2} d\eta = \frac{\pi}{32} \qquad 1.3.4 \int_0^1 \eta^4 (1-\eta^2)^{3/2} d\eta = \frac{3\pi}{256}$   $1.1.5 \int_0^1 \frac{\eta^5 d\eta}{\sqrt{1-\eta^2}} = \frac{8}{15} \qquad 1.3.5 \int_0^1 \eta^5 (1-\eta^2)^{3/2} d\eta = \frac{8}{315}$ 

1.1.0 
$$\int_0^1 \frac{d\eta}{\sqrt{1-\eta^2}} = \frac{\pi}{2}$$
1.1.1 
$$\int_0^1 \frac{\eta d\eta}{\sqrt{1-\eta^2}} = 1$$

1.2.0 
$$\int_0^1 \sqrt{1 - \eta^2} d\eta = \frac{\pi}{4}$$

1.3.0 
$$\int_0^1 (1 - \eta^2)^{3/2} d\eta = \frac{3\pi}{16}$$

1.1.1 
$$\int_0^1 \frac{\eta d\eta}{\sqrt{1-n^2}} = 1$$

1.2.1 
$$\int_0^1 \eta \sqrt{1-\eta^2} d\eta = \frac{1}{2}$$

1.3.1 
$$\int_0^1 \eta (1 - \eta^2)^{3/2} d\eta = \frac{1}{5}$$

1.1.2 
$$\int_0^1 \frac{\eta^2 d\eta}{\sqrt{1-\eta^2}} = \frac{\pi}{4}$$

1.2.2 
$$\int_{0}^{1} \eta^{2} \sqrt{1 - \eta^{2}} d\eta = \frac{\pi}{1 + \eta^{2}}$$

1.3.2 
$$\int_0^1 \eta^2 (1 - \eta^2)^{3/2} d\eta = \frac{\pi}{2}$$

1.1.3 
$$\int_0^1 \frac{\eta^3 d\eta}{\sqrt{1-\eta^2}} = \frac{2}{3}$$

1.2.3 
$$\int_{0}^{1} \eta^{3} \sqrt{1 - \eta^{2}} d\eta = \frac{2}{15}$$

1.3.3 
$$\int_0^1 \eta^3 (1 - \eta^2)^{3/2} d\eta = \frac{2}{35}$$

$$1.1.4 \int_0^1 \frac{\eta^4 d\eta}{\sqrt{1-\eta^2}} = \frac{3\pi}{16}$$

1.2.4 
$$\int_{0}^{1} \eta^{4} \sqrt{1 - \eta^{2}} d\eta = \frac{\pi}{100}$$

1.3.4 
$$\int_0^1 \eta^4 (1 - \eta^2)^{3/2} d\eta = \frac{3\pi}{2\pi}$$

1.1.5 
$$\int_0^1 \frac{\eta^5 d\eta}{\sqrt{1-\eta^2}} = \frac{8}{15}$$

1.3.5 
$$\int_0^1 \eta^5 (1 - \eta^2)^{3/2} d\eta = \frac{8}{315}$$

$$1.4.0 \int_0^1 (1 - \eta^2)^{5/2} d\eta = \frac{5\pi}{32}$$

$$1.5.0 \int_0^1 (1 - \eta^2)^{7/2} d\eta = \frac{35\pi}{256}$$

$$1.6.0 \int_0^1 (1 - \eta^2)^{9/2} d\eta = \frac{63\pi}{512}$$

$$\begin{array}{ll} 1.4.0 \int_{0}^{1} (1-\eta^{2})^{5/2} d\eta = \frac{5\pi}{32} & 1.5.0 \int_{0}^{1} (1-\eta^{2})^{7/2} d\eta = \frac{35\pi}{256} & 1.6.0 \int_{0}^{1} (1-\eta^{2})^{9/2} d\eta = \frac{63\pi}{512} \\ 1.4.1 \int_{0}^{1} \eta (1-\eta^{2})^{5/2} d\eta = \frac{1}{7} & 1.5.1 \int_{0}^{1} \eta (1-\eta^{2})^{7/2} d\eta = \frac{1}{9} \\ 1.4.2 \int_{0}^{1} \eta^{2} (1-\eta^{2})^{5/2} d\eta = \frac{5\pi}{256} & 1.5.3 \int_{0}^{1} (1-\eta^{2})^{7/2} d\eta = \frac{7\pi}{512} \\ 1.4.3 \int_{0}^{1} \eta^{3} (1-\eta^{2})^{5/2} d\eta = \frac{2}{63} & 1.5.4 \int_{0}^{1} \eta^{3} (1-\eta^{2})^{7/2} d\eta = \frac{2}{99} \\ 1.4.4 \int_{0}^{1} \eta^{4} (1-\eta^{2})^{5/2} d\eta = \frac{3\pi}{512} \\ 1.4.5 \int_{0}^{1} \eta^{5} (1-\eta^{2})^{5/2} d\eta = \frac{8}{693} \end{array}$$

1.5.3 
$$\int_0^1 (1 - \eta^2)^{7/2} d\eta = \frac{7\pi}{513}$$

$$\eta^{2}(1-\eta^{2})^{5/2}a\eta = \frac{1}{256}$$
$$\eta^{3}(1-\eta^{2})^{5/2}d\eta = \frac{2}{62}$$

1.5.3 
$$\int_0^1 (1 - \eta^2)^{7/2} d\eta = \frac{7\pi}{512}$$

$$1.4.4 \int_0^1 \eta^4 (1 - \eta^2)^{5/2} d\eta = \frac{37}{51}$$

$$1.4.5 \int_0^1 \eta^5 (1 - \eta^2)^{5/2} d\eta = \frac{8}{693}$$

$$2.1.1 \int_0^1 \eta \ln \frac{1 + \sqrt{1 - \eta^2}}{\eta} d\eta = \frac{1}{2}$$

$$2.1.2 \int_0^1 \eta^2 \ln \frac{\eta}{\eta} d\eta = \frac{\pi}{12}$$

$$2.1.3 \int_0^1 \eta^3 \ln \frac{\eta}{\eta} d\eta = \frac{1}{6}$$

$$2.1.4 \int_0^1 \eta^4 \ln \frac{\eta}{\eta} d\eta = \frac{6}{80}$$

$$2.1.5 \int_0^1 \eta^5 \ln \frac{1 + \sqrt{1 - \eta^2}}{\eta} d\eta = \frac{4}{45}$$

Integrals in upwash generated by vortex distributions  $|\eta| < 1$ 

3.1.1 
$$I_{0,0}(|\eta| < 1) = \text{CPV} \int_{-1}^{1} \frac{d\eta'}{\eta - \eta'} (1 - {\eta'}^2)^{\frac{-1}{2}} = 0$$

3.1.2 
$$I_{0,2}(|\eta| < 1) = \text{CPV} \int_{-1}^{1} \frac{d\eta'}{\eta - \eta'} (1 - {\eta'}^2)^{\frac{1}{2}} = \pi \eta$$

$$3.1.3 I_{0,4}(|\eta| < 1) = \text{CPV} \int_{-1}^{1} \frac{d\eta'}{\eta - \eta'} (1 - {\eta'}^2)^{\frac{3}{2}} = \pi \eta (\frac{3}{2} - \eta^2)$$

$$3.1.4 I_{0,6}(|\eta| < 1) = \text{CPV} \int_{-1}^{1} \frac{d\eta'}{\eta - \eta'} (1 - {\eta'}^2)^{\frac{5}{2}} = \pi \eta \left(\frac{15}{8} - \frac{5}{2}\eta^2 + \eta^4\right)$$

Integrals in upwash generated by vortex distributions  $|\eta| > 1$ 

3.2.1 
$$I_{0,0}(|\eta| > 1) = \int_{-1}^{1} \frac{d\eta'}{\eta - \eta'} (1 - {\eta'}^2)^{\frac{-1}{2}} = \pi (\eta^2 - 1)^{-1/2}$$

$$3.2.2 I_{0,2}(|\eta| > 1) = \int_{-1}^{1} \frac{d\eta'}{\eta - \eta'} (1 - {\eta'}^{2})^{\frac{1}{2}} = \pi \eta - \pi (\eta^{2} - 1)^{1/2}$$

$$3.2.3 I_{0,4}(|\eta| > 1) = \int_{-1}^{1} \frac{d\eta'}{\eta - \eta'} (1 - {\eta'}^{2})^{\frac{3}{2}} = \pi \eta (\frac{3}{2} - \eta^{2}) + \pi (\eta^{2} - 1)^{3/2}$$

$$3.2.4 I_{0.6}(|\eta| > 1) = \int_{-1}^{1} \frac{d\eta'}{n-\eta'} (1 - {\eta'}^2)^{\frac{5}{2}} = \pi \eta \left(\frac{15}{8} - \frac{5}{2}\eta^2 + \eta^4\right) - \pi (\eta^2 - 1)^{5/2}$$

Integrals in upwash generated by natural-logarithmic vortex distribution

$$4.1.1 J_1(|\eta| < 1) = \text{CPV} \int_{-1}^{1} \ln \frac{1 + \sqrt{1 - \tilde{\eta}^2}}{|\tilde{\eta}|} \frac{\tilde{\eta} d\tilde{\eta}}{\eta - \tilde{\eta}} = \pi (-1 + \frac{\pi}{2} |\eta|)$$

$$4.2.1 J_1(|\eta| > 1) = \int_{-1}^{1} \ln \frac{1 + \sqrt{1 - \eta'^2}}{|\eta'|} \frac{\eta' d\eta'}{\eta - \eta'} = \pi \left[ -1 + \eta \arcsin\left(\frac{1}{\eta}\right) \right]$$